A Thesis

entitled

THE DEVELOPMENT AND USE OF SCINTILLATION CHAMBERS IN NUCLEAR PHYSICS

by

John Walters, B.Sc., A.R.C.S.

Submitted for the
Degree of Doctor of Philosophy
of the University of London.

Department of Physics,
Imperial College,
London S.W.7

November 1962

ABSTRACT

In this thesis the results of an investigation into the use of image intensifiers for nuclear physics research are presented. In Chapter 1, the current methods of nuclear physics research are described and the properties of image intensifier tubes which make them useful for looking at weak visible light signals are described, with particular reference to their use in conjunction with scintillating materials. Chapter 2 reviews the types of image tubes currently available and the work that has been carried out in the field to date.

Some preliminary experiments on lenses, phosphor decay times, and switching tests on image tubes are described in Chapter 3, and the experimental apparatus that was built and set up to conduct tests at the 'Saturne' accelerator near Paris is described in Chapter 4.

Chapter 5 is devoted to the scintillation chamber experiments carried out using $\mathrm{NaI(t\ell)}$ and $\mathrm{CsI(t\ell)}$ crystals, plastic scintillator and scintillating glass as the chamber materials. The results of these experiments are presented in terms of the number of recorded scintillation flashes per cm. (in chamber space) under different conditions, and the figures obtained are used to estimate the recording efficiency of the image intensifiers for photo-electrons.

The photography of Čerenkov light from single particles in

the form of a ring image is described in Chapter 6, and the results are used to make another estimate of the recording efficiency of the intensifying system. The results of beam profiling experiments carried out using the image intensifying system are presented in the following chapter, together with a general discussion of the technique.

In Chapter 8, the present performance capabilities of fibre and homogeneous scintillation chambers are compared with the rival technique of spark chambers, and the usefulness of the scintillation chamber and Čerenkov camera for current nuclear physics research is discussed. Possible extensions of these methods in the future are also described.

CONTENTS.

CHAPTER 5.- The Scintillation Chamber Experiments.

CHAPTER 6.- The Cerenkov Ring Experiment.

CHAPTER 7.- Beam Profiling Experiments.

CHAPTER 1

Introduction to the use of Image Intensifiers in Nuclear Physics

1.1 Introduction.

There are a number of phenomena in nuclear physics whose investigation depend on the observation of the spatial and temporal distribution of weak visible light. Examples are the scintillation light emitted by certain luminescent materials when a charged elementary particle passes through, or the Čerenkov light emitted by a charged particle travelling through a medium at a speed greater than the speed of light in the medium.

Hitherto, the above phenomena have been largely investigated using conventional scintillation counter techniques and photomultiplier arrays. The advent of image intensifying systems with a sufficiently high gain to enable single photons of optical wavelength to be recorded with high efficiency using conventional fast photographic emulsion has resulted in a number of new methods of experimental investigation. The high gain intensifier tubes now available make it possible to amplify the light intensity of faint objects by factors $\sim 10^5$, whilst still preserving the spatial distribution of the light falling on the photocathode. Before discussing the possibilities of image intensifiers in nuclear research, a brief review of present detecting devices will be given.

1.2 Brief Review of Detecting Devices used in current Nuclear Physics Research

The experimental investigation of the properties of the elementary particles involves the interaction of these particles with matter in such a way that useful information is obtained. Depending on the nature of the device, this information may simply be their detection (i.e. presence or absence of a particle), or their detection in such a way that further information can be obtained in a fairly straightforward manner. Usually a nuclear physics experiment involves the use of several different devices for the detection, identification and measurement of the kinematic and dynamic properties of the particles under investigation, the different detectors being combined in a logical way so that the required measurements are made to the necessary precision.

Many of the detectors used are of the "track" type; that is, they enable the trajectories of the various particle interactions and decays to be seen (and usually photographically recorded). The track devices which are in current use are:-

(a) Cloud Chambers (including diffusion cloud chambers).

(b) Nuclear Photographic Emulsions.

(c) Bubble Chambers.

(d) Spark Chambers.

(e) Scintillation Chambers.

The cloud chamber contains a gas, and a supply of some liquid which has a reasonable vapour pressure at room temperature. If the vapour has reached equilibrium, and the volume of the chamber is suddenly increased, the gas is rapidly cooled, producing a condition of supersaturation of the vapour. The trail of ions left by the passage of a charged particle through the chamber act as condensation centres on which droplets of liquid can grow. Thus the trajectories of ionizing particles can be photographed in the form of liquid droplets. Stereoscopy is usually obtained by photographing from three different camera positions, and if a magnetic field is applied in the chamber volume the tracks are curved, enabling the momentum of the particles to be determined. Also, if the particle velocities are non-relativistic, the density of droplets per unit path length can be used to estimate the quantity '$Z/_{V}$'.

The simple cloud chamber is sensitive for only a short period (up to a few tenths of a second) after the expansion stroke because the gas soon heats up again by conduction from the chamber walls. A continuously sensitive device, known as the 'Diffusion Cloud Chamber' has been developed, in which vapour is allowed to diffuse downwards continuously in a region in which a steady vertical temperature gradient is maintained. Supersaturation then exists continuously throughout a certain zone. High pressure gas fillings are used to increase the likelihood of events, but in the case of expansion cloud chambers, the technological problem associated with high pressures is formidable.

A large cloud chamber such as the one being built at CERN (170 cm. by 60 cm. by 40 cm.) must be post-expansion operated, and has a resetting time of several minutes which is extremely wasteful of machine pulses. The precision of momentum measurement in cloud chambers is ideally set by diffusion of the ions during track formation, and by scattering of the particles in the gas, but errors often arise due to the presence of convection currents in the gas.

The 'Bubble Chamber', which was invented by Glaser[1], has largely replaced cloud chambers as a visual technique for use with high energy accelerators. The chamber operates on the principle that a superheated liquid will not boil spontaneously, but must contain a local heating discontinuity in order to boil; a charged particle passing through a sufficiently superheated liquid will produce the necessary local heating to cause boiling, resulting in a string of rapidly growing bubbles along the path of the particle. In a typical bubble chamber operating cycle, the hydrostatic pressure is rapidly reduced in a time ∼ a few msec (milliseconds) so that the pressure in the liquid goes below the vapour pressure and into the sensitive region. For a period of up to 10 msec. afterwards the expansion is such that the boiling at the various surfaces keeps pace with the expanding system, and the pressure is more or less constant. The chamber is now sensitive to charged particles, and these are injected sometime during this period; a few msec. later, the lights are flashed on and the bubbles are photographed. Finally, a fairly fast recompression ($\sim$ 5 msec) is applied, when the chamber returns to its quiescent state.

Chambers with volumes of several hundred litres have been built. The recycling time is $\sim$ 1 sec., (but may be increased to 10 - 15 per sec.), and the sensitive time ranges from 5 to 10 msec. The number of bubbles per cm. is $\propto 1/\beta^2$ but is a sensitive function of the thermodynamic conditions. Bubble chamber tracks are better defined than those of cloud chambers ($\sim$ 0.1 mm), but the bubble chamber cannot be used with counter controlled expansion.

In recent years, the photographic emulsion has been established as a versatile instrument for nuclear particle detection.

Its use is based on the fact that a fast particle, if it passes through a silver bromide grain in an emulsion, can make it developable. Special emulsions have been developed for use in nuclear physics, capable not only of counting particles, but of giving precise information concerning their mass, energy and modes of interaction and decay. The emulsion is a continuously sensitive device, so that no time resolution exists in the sense discussed above. The space resolution is of the order of the grain size of the emulsions ($\sim$ few microns).

Within the past eighteen months, a new and versatile track device, - the 'Spark Chamber', has been utalized in nuclear research. In most of the current types, this chamber consists of a series of parallel plates in which a voltage difference of several hundred volts is applied to alternate plates as a clearing field to sweep out electrons created by uninteresting tracks in a time $\sim 0.5 \mu$sec (microseconds). When an interesting event occurs, in the form of the passage of one or more ionizing particles across the gap, a high voltage ($\sim 10^4$ volts) is pulsed onto the plates within a few tenths of a microsecond and then removed after sufficient energy has gone into the discharge to permit direct photography of the "tracks". More than one particle passage per gap can be viewed, and the spark widths are $\sim$ 1mm. Table A is a compilation of the important parameters and special features of these track devices for comparison.

The other general class of detecting devices (generally called counter devices) is that in which the spatial resolution is usually relatively poor, but where the time resolution is much better than for the visual techniques. The first type of counter widely used was the Ionization Chamber. This consists of two conductors which are insulated from each other, the space between being gas filled and containing an electric field. If the voltage is low (i.e., $\sim$ 500 volts for a spacing of several cms.), then with the proper gas at the correct pressure the primary ions and the electrons produced by the passage of an ionizing particle can be

'Track' devices in current use

Type of chamber	Dimensions.	Material of chamber	Resolving time	Cycling time	Track resolution	Special features; capabilities.
Cloud Chamber	up to 170 X 60 X 40 cm.	Helium, Argon etc. at various pressures	$10^{-2} \to 10^{-1}$ sec	several secs. to several minutes.	typically ~ few x 10^{-1} mm.	Counter control (except very large chambers) Diffusion chamber is continuously sensitive.
Bubble Chamber	up to ~ 200 X 50 x 50 cm.	Hydrogen; Helium; Xenon; WF_6	~ 10^{-3} sec	≳ 1sec.	~ 10^{-1} mm.	
Nuclear Emulsions	~30cm X 30cm X 600μ pellicules, which can be stacked.	Ag, Br, I, C, H, O, N.	—	—	~ 10^{-3} mm.	
Spark Chambers	~ 1 metre cube. Can be stacked together to make larger units	Wide variety of plate materials Al → Pb.	$10^{-7} \to 10^{-6}$ sec.	dead time ~ 10^{-3} sec.	~ 1 mm.	
Scintillation Chamber	≲ 15cm. cube.	NaI (Tl) CsI (Tl) plastic etc.	$10^{-7} \to 10^{-6}$ sec.	$10^{-5} \to 10^{-6}$ sec	~ 1 mm.	Isotropic sensitivity. Energy-sensitive response. Counter trigger selection.

TABLE 'A'

collected, giving a weak signal. For higher voltages, the electrons make further ions as they are collected and the device is a "Proportional Counter". Finally, for voltages ~ 1000 volts/cm., the passage of a single charged particle causes a complete breakdown in the gap, and a count is registered. When operated in this fashion, the device is called a "Geiger-Muller Counter". Gas counters such as these have varied in size (i.e. space resolution) from a fraction of a centimetre up to 1 metre, with typical recovery times $\sim 100\ \mu$ sec.

The counters in most common use at present are both based on the detection and measurement of weak visible light. In the conventional "Scintillation Counter", the particles or quanta are allowed to enter a suitable organic crystal or other phosphor. Some of the atoms are excited, and on returning to their normal state, emit light (scintillate). Some of this light is picked up by the photocathode of an electron-multiplier tube (photomultiplier), and the resulting photo-electrons are multiplied in the suceeding electron-multiplication stages. A burst of electrons arrives at the final collecting anode, and the current pulse obtained is related in time to the nuclear event under observation. The time-integral of this current pulse is proportional to the total number of photons emitted in the phosphor, which is in turn a function of the energy of the particle or quantum of radiation being measured. The time resolution in scintillation counters is very good, both on the rise time and duration of the pulse; time resolutions down to 1 nsec. (nanosecond) are common for these devices. They can be made into sensitive volumes up to cubic metres. There is, however, no comparison with the track chambers for spatial resolution.

The high amplifications of photomultipliers (gains of 10^6 to 10^8 with transit-time delays $\sim$ a few times 10^{-8} sec.) has resulted in the possibility of recording the Čerenkov radiation emitted by energetic charged particles travelling through a transparent medium. Such counters can be used as velocity or momentum selecting counters because the intensity and direction of the Čerenkov radiation is a function of the particle velocity (the intensity is also a function of the charge carried by the particle).

It is in these last two effects that light intensification with good spatial resolution results in entirely new devices for nuclear physics research. In the present thesis, experiments on the use of an image intensifying system for viewing various scintillating materials to give a new type of track chamber, - (the"Scintillation or Luminescent Chamber") are described. Also, the photography of the Čerenkov radiation in the form of a ring image from a single charged particle is described. An experiment on the use of image intensifiers for determining the number and spatial distribution of the particles in a particle beam was also carried out, and is described in Chapter 7.

1.3 General Requirements for using Image Intensifiers in Nuclear physics.

The scintillation chamber consists of the scintillating material (which is the sensitive volume of the chamber), some means of imaging the light from the scintillation track onto the first photocathode of the intensifying system, the electron-optical intensification, and finally the image recording system. The final recording is usually done photographically, but the image can also be fed straight into a television viewing system.

The problem of recording the track image can be divided into two parts:-

(i) transference of light from the scintillation track onto the photocathode of the image-intensifier.

(ii) amplification and final recording of the photo-electronic image, including any switching that may be necessary to select the desired nuclear event.

The optical coupling onto the image tube will be discussed in the next section; the photo-electronic amplification is considered first. For the purposes of track imaging, an ideal detector would record the spatial and temporal co-ordinates of every photon from the original photon signal falling on the primary photo-sensitive surface. In practice, all image-intensifying systems fall short of this ideal performance in various ways. Thus the overall quantum sensitivity (i.e. the probability that any particular photon will produce a detectable event) is less than unity. Also, spurious events take place without the absorption of signal photons, introducing a "noise" which tends to mask the genuine signal. In order to estimate the amplification factor needed to give a high overall quantum sensitivity, the performance of photographic emulsion must be considered in some detail. In the photographic effect, the quantum efficiency of the primary process is low, and is a function of the exposure. It falls to zero for very small and very large exposures and has a maximum value of 0.1% to give reasonable densities in the fastest emulsions[2]. There is, of course, a "noise" element in the photographic effect, since on development, a number of silver grains are produced even with no exposure to signal photons due to light "fogging", unavoidable bombardment by natural radioactivity and the cosmic radiation. Among the interactions of photons with matter, the photo-emissive effect is highly efficient, with quantum efficiencies up to 30%. By coupling a primary detector of this kind to a photographic emulsion such that a single secondary event has a high probability of producing at least one developable grain in the emulsion, the overall quantum sensitivity of the composite detector will be very much greater than the emulsion alone, provided no significant noise is added by the new primary detector. The gain required in an image intensifier system with photographic recording in order to use the quantum efficiency of the primary photo-electric effect to the full is that which amplifies every photo-electron from the photo-cathode to a light level which can be recorded as a developed grain in the photographic emulsion. A quantum efficiency of 0.1% for the photographic emulsion means that 1000 photons must fall on an area of the order of the mean grain size ($\sim 4\,\mu$ diameter) to render it developable; that is, a photon flux of 10^{10} photons/ cm^2. If the final scintillation flashes in the output phosphor are imaged on the emulsion using f/1 optics (corresponding to a geometrical collection efficiency of 1/5 for a Lambertian emission), then $\sim 5.10^{10}$ quanta/cm^2 are needed at the phosphor. With a typical resolution of 10 line pairs per mm. (i.e. a mean scintillation flash diameter $\sim$ 0.05mm) this implies 10^6 quanta per scintillation flash. Taking the input quantum efficiency of the intensifier system to be 10%, an overall gain $\sim 10^5$ is required. The above calculation takes no account of the variation in the response of the various elements of the system with photon wavelength and contains many approximate numbers, but gives a reasonable order-of-magnitude value for the required gain.

An alternative to photographic recording is to use a television system. The best T.V. Vidicon cameras (in which the photon signal is imaged onto a photoconductive layer which is periodically scanned by an electron beam) have an overall quantum sensitivity which is approximately an order of magnitude less than the best photographic emulsions[3]. Image Orthicons (in which the photon image is converted into a photo-electric image at the input photocathode with subsequent electron optical focussing and acceleration of the electron image onto a secondary emitter storage surface,from which the signal is periodically read off) are generally about an order of magnitude more sensitive than emulsions under conditions which would be suitable for track imaging[3], but are very expensive.

Whilst image orthicons and image-intensifier orthicons offer the advantage of immediate visual presentation of the track information on a T.V. monitor, - a feature which is a considerable help for some applications of track imaging, and also present the signal in a form which is easier to digitize for computer analysis than a photograph, there are a number of drawbacks, mainly concerning control and quality of the signal. Image tubes now have better resolution with less noise and distortion than an orthicon of comparable amplification. More serious for track imaging is the fact that orthicons, at a given beam setting, do not have enough range to provide maximum signal-to-noise ratio for a minimum ionizing track and still not overload on the image of a stopping track.

Another essential feature of any image intensifier system used in nuclear physics experiments is that of pulsed operation. The reasons for this are:-

(i) instrumental. The dark current (i.e. thermal electrons and other spurious noise electrons) from the photocathode in image tubes ranges from ~100 to 10,000 electrons per cm^2 per sec., and since most events of interest in nuclear physics result in only tens of photoelectrons over the whole photocathode area, then only by looking at the output end for a fairly short time is it possible to reduce the signal to noise ratio to a reasonable number.

(ii) nuclear physics requirements. It is almost always necessary to select the events of interest in the presence of other uninteresting events which have occurred just before or just after the desired event. Only by cutting down the viewing time so as to exclude these near-contemporary events can a clear, unambiguous picture be taken.

For both the above reasons, switching times varying from 1 μ sec to 1 msec. are in practice needed, depending on the particular experiment.

Since all selection involves the use of scintillation counters, there must be a storage mechanism somewhere before the switching element in the system capable of retaining the picture of the track for a time ~ 10^{-7} sec., - the time needed for conventional circuits to decide whether or not the picture is to be recorded. For some high efficiency inorganic scintillators, the decay time of the scintillation light is relatively long (~250 nsec. for Na I (Tl); ~1000 nsec. for CsI (Tl); both to 1/e of the initial intensity) so that if an intensifier could be switched on within $\sim$100 nsec of the occurrence of the event only about 25% of the scintillation light would be lost; the remainder could be intensified and recorded. Thus a single tube capable of being switched, and having sufficient gain to enable single photoelectrons from the photocathode to be recorded would be adequate for such scintillators.

For glass and plastic scintillators, the decay times for scintillation light are 50 to 100 nsec. and 5 to 10 nsec. respectively, so that an alternative storage mechanism must be used. In this case, two intensifiers in cascade provide a suitable system; the first image tube is operated continuously and the second is pulsed from the counter coincidence circuitry. The storage time available is now the phosphor decay time of the first tube.

For optimum gain through the system, the spectral outputs and responses of the phosphors and photocathodes in the system should be well matched, and the various optical coupling elements should have good transmission characteristics for the wavelengths incident on them.

The other aspects of the image intensifying process which limit the performance of the system are the resolution of the image over the sensitive field area, distortion characteristics and the shape and size of the primary sensitive area. These parameters vary widely for different intensifier tubes and it will just be noted here that the resolutions attained with present tubes range from ~ 1 to ~ 30 ℓp/mm.,[*] with useful photocathode sizes from 1 cm. diameter up to ~ 10 cm. diameter. The photocathode area is usually a severe restriction on the chamber size that can be used for a nuclear physics experiment. In most cases of scintillation track imaging, the large aperture optics which is required to give a useful photon signal on the photocathode, together with the need for a reasonable depth of field in the chamber, means that the spatial resolution and distortion of the image intensifier system is not a limiting factor for this application. In the case of Čevenkor ring imaging, however, spatial resolution is of high importance, as will be discussed in Chapter 6.

It is desirable that the degree of multiplication of every photoelectron should be as uniform as possible so that the final scintillation flashes do not vary greatly in intensity. Finally, it should be noted that the electric and magnetic field requirements of the intensifiers should not be upset by the rest of the apparatus used in a nuclear physics experiment.

[*] One line pair per millimetre (1 ℓ.p./mm.) corresponds to one black and one white line of equal width per millimetre, with 100% modulation of the input pattern. The modulation required at the output was not strictly defined, - only the ability to distinguish lines with the eye was required.

1.4 Transference of light from the Scintillation Tracks onto the Photocathode Surface.

It was shown in the last section that the maximum equivalent quantum efficiency of the overall intensifying system is ultimately limited by the quantum efficiency of the initial photocathode (typically 10 to 20%). Table B gives the typical quoted scintillation outputs of the most efficient scintillation materials available; it is apparent that the efficient optical coupling of the useful chamber volume to the photocathode is of prime importance because of the small photon signal available. Two different types of chamber have been proposed:-

(a) Homogeneous chamber with conventional coupling optics. The major drawback of using this arrangement is the fact that a workable compromise has to be taken between light collection (requiring wide aperture optics), and depth of field (requiring small aperture optics). Table C gives typical values for the chamber parameters for a Na I (tl) scintillator. (No account is taken of light absorption either in the luminescent material or lens. The figures are given as an indication of the number of photons involved). Column H of Table C is a calculation of the number of photons collected by various lens combinations of different demagnifications and Column K gives the useable depth of field for a disc of confusion of 1 mm. at the photocathode. Thus the useable volume of the chamber is limited by

Chamber Material.	Density (gm./cm.^{3})	Decay time to 1/e (sec.)	Energy loss for minimum ionization. MeV/(gm/cm.^{2})	Scintillation Effeciency.	Spectral peak. (Ångstroms.)	No. of photons per cm. for minimum ionizing particles	Radiation Length (cm.)	Refractive Index
NaI(Tl)	3·67	$0{\cdot}25 \times 10^{-6}$	~1·3	~8 %	4130	~125,000	2·6	1·775
CsI(Tl)	4·51	$\cdot 7 \times 10^{-6}$	~1·3	~5 %	4200-5700	~105,000	1·9	1·788
NE102 plastic scintillator	1·03	3×10^{-9}	~2·0	3 %	4250	~20,000	42·0	1·581
GS/1 glass scintillator	2·70	$5\times10^{-8} < \tau < 10^{-7}$	~1·7	~1 %	3950	~15,000	11·0	1·57

TABLE 'B'

TABLE 'C'

Chamber parameters for NaI(Tl).

A	B *	C	D	E *	F *	G	H †	J §	K *
Demagnification	Back f/number of lens, 'A'. [$A = v/d$]	Focal length, 'f' [cm.]	Diameter of chamber field of view [cm.]	θ	θ'	% of isotropic emission collected	Photons per cm. in chamber collected for minimum ionizing particle	Recorded spots per cm. in chamber	Depth of field for 1mm. disc of confusion on photo-cathode
2	1	6·7	5	14°2'	7°51'	·47	~600	~20	± 7mm.
3	1	7·5	7·5	9°28'	5°19'	·22	~270	~9	± 16mm.
4	1	8·0	10	7°7'	4°0'	·12	~150	~5	± 28mm.
6	1	8·6	15	4°45'	2°41'	~·05	~60	~2	± 64mm.

Notes:
- * These parameters are explained in Appendix A, and Fig. 31.
- † Scintillation efficiency of 8% assumed here.
- § Assuming 10% quantum sensitivity for the photocathode, and 33% for the recording efficiency for photoelectrons. (no lens transmission factors are taken into account.) The figures are for minimum ionizing excitation.

depth of focus requirements to a few inches in depth, and to about 10 cm. in diameter, the maximum allowed volume depends on the limits set to the spot spacing and the tolerable disc of confusion. A more exact analysis of the geometrical light collection problem for homogeneous scintillators is given in Appendix A, and a discussion of the relative merits of the various chamber materials is given in Chapter 8.

(b) Fibre Chambers.

Filaments or fibres of plastic scintillor may be used to overcome the depth of field limitations of the homogeneous chamber. The chamber is made up of a large bundle of fibres, the scintillation light being "piped" to the end of each fibre by total internal reflection. The spatial resolution of the chamber is set by the fibre diameter, and the useful depth of a chamber is determined by the attenuation length of the light travelling down a fibre. Recently a special scintillating glass has been developed[4], which should have better drawing properties than plastic scintillator; the attenuation of the light (which is mainly due to scattering caused by imperfections or "crazing" of the fibre surface) as it is piped down the fibre should be substantially less than for the plastic scintillator, but the scintillation efficiency of glass is less than that of plastic (see Table B). For a plastic fibre of diameter 1 mm., approximately 1000 photons, on average, are produced by a minimum ionizing particle traversing a fibre diameter; 15 to 20% of the total solid angle is collected in the forward direction by total internal reflection, so that with zero attenuation about 200 photons would be piped to the fibre end. In practice a figure of 50 photons is more reasonable. These photons are distributed over angles ranging from zero up to the critical angle with respect to the fibre axis, but tend to be peaked forward because small angle photons are subject to fewer reflections. Only a small number are collected if conventional coupling optics is employed. For example, an f/1 lens working at 4 : 1 demagnification (giving a useful chamber diameter of 8 cm. for a 2 cm. diameter photocathode) would collect $\sim 1\%$ of the light, so that the chance of producing one photoelectron per fibre is much less than unity, even assuming 100% transmission for the lens element. Thus the size of the chamber is prohibitively small for a reasonable chance of producing one or more photoelectrons per fibre if a lens coupling is used. An alternative approach is to butt the fibre bundle directly against the end-wall of the image tube. A very high collection efficiency can be obtained in this way, but the resolution is limited by the thickness of the glass wall of the tube (between 2 and 3 mm. for most tubes). The best method of coupling is to butt the fibre chamber up against an image tube having a special glass fibre cathode window, when the resolution is unaffected and a very high collection efficiency is retained

Stereoscopy can be achieved in both cases by using two sets of image intensifying systems to view the chambers at any desired angle. In the case of the fibre chamber, a matrix made up of alternating layers of fibres at the appropriate angle can be constructed. It is interesting to note that the two stereoscopic views of a homogeneous chamber would differ in one fundamental aspect from similar pictures taken of cloud chamber or bubble chamber tracks. Since the particular quanta which result in photo-electrons in the two intensifier channels cannot be the same ones, the two views will, be made up of "different" scintillation spots. In the case of a fibre chamber matrix, the two intensifier systems look at different sets of fibres so that the two views of necessity originate from different photon aggregates.

CHAPTER 2

Review of Image Tubes available and Experiments carried out in the field.

2.1 Review of Image intensifiers Available.

All the image tubes at present available consist of evacuated envelopes (usually of glass), with a photoemissive layer deposited on the input window, some means of amplifying the primary photo-electron signal whilst preserving the image, and finally the conversion of the electron signal into a visible light signal at the phosphor deposited on the output window. A variation on the final conversion exists in image orthicons and image-intensifier orthicons in which the electron image is stored in a secondary emission target, and a "reading" electron beam periodically removes the store on an element-by-element basis and converts it into an electric video-signal for display on a T.V. system.

The electron-optics used in image tubes can be simple acceleration by a uniform electric field, electrostatic lens systems (usually with demagnification of the image), thin magnetic lens systems, or an electrostatic-magnetic focussing system.

Apart from "zero-stage" tubes, in which the photo-electrons are accelerated straight onto the output phosphor, two modes of amplification are extensively used:-

(a) Sandwich stages. The dynodes consist of a phosphor and photocathode deposited on opposite sides of a thin transparent membrane. The membranes are made of mica or glass between 5 and 10 microns thick to minimize loss of resolution. With Antimony-Caesium photocathodes and Zinc Sulphide (P.11) phosphor combinations, stage gains ~50 are attained for 15 Kilovolts incident electrons so that 3 such stages incorporated between input photocathode and output phosphor are sufficient to enable single photo-electrons to be recorded with high efficiency. The membranes are sufficiently thick to prevent any primary electrons from penetrating into the next stage. Because many photocathodes and phosphors have to be deposited in one envelope these tubes are difficult to make. They have the considerable advantage, however, that since the stage gains are high the spread in gain due to statistical fluctuations is likely to be low.

(b) Transmission secondary emission thin film dynodes.

The electrons of the electron image are accelerated and focussed onto one side of a thin secondary emission film, deposited on a thin conducting support membrane. The energy of the impinging electrons is chosen so that they have a small probability of emerging from the opposite side, but secondary electrons that they produce have a sufficiently high probability of escape to do so in numbers greater than the number of incident primaries. Mean gains ~ 5 are obtained for accelerating voltages of 4 to 5 Kilovolts. Little is known about the exact nature of the transmission secondary emission process. Recent measurements of the amplitude distribution of photomultiplier anode pulses due to single electron emission from the photocathode by Tusting et. al. [5] show a peak in the distribution, and are consistent with a calculated distribution based on a Poisson distribution of secondaries at each dynode. It is thought that previous measurements by Lombard et. al. [6] indicated an exponential distribution because of the presence of noise. However, measurements made on 5-stage transmission secondary emission tubes in the Instrument Technology department of Imperial College [7] indicate a fit to an exponential distribution down to a tenth of the mean gain. The only figure available for the number of primary electrons that give zero secondaries is a measurement carried out on a single dynode of a one-stage tube; about 50% of the primaries gave zero secondaries.

A disadvantage of secondary emission thin films is that a number of the primary electrons penetrate into the next stage; such electrons are unfocussed and result in loss of contrast and noise at the output. Measurements made with a single stage tube [8] give a figure of 50% for the number of incident primary electrons which yield secondary electrons of energy $\geqslant$ 50eV; that is, about 10% of the emission electrons from the dynodes are fast unfocussed electrons. Also there is a wide range in the intensities of the final scintillation spots from transmission secondary emission image tubes due to the statistical fluctuations around the mean gain.

A table summarising the properties of the image tubes at present available is given in Appendix B.

2.2 Description of "Twentieth Century Electronics" and "English Electric" 5-stage Transmission Secondary Emission Image Intensifiers.

When the research work described in this thesis was started, successful five-stage transmission secondary emission image intensifiers of the Wilcock-Emberson type [9] had been made in the Instrument Technology department of Imperial College. Shortly afterwards, the manufacture of similar tubes was undertaken by Twentieth Century Electronics Ltd., and the number and variety of tubes available increased. These tubes are 40 cm. long and 6.4 cm. diameter with Antimony-Caesium photocathodes of up to 40 micro-amps. per lumen efficiency (corresponding to a quantum efficiency of about 10% at 4000Å). They can be supplied with 'slow' decay phosphors (e.g., P.11. ZnS), or the less efficient 'fast' phosphors (e.g. P.24 ZnO). The useable area of the photocathode is 19 mm. with a resolution of 15 ℓp/mm or better over the whole field, with only slight S-distortion. Photo-electrons are accelerated onto a film of KCl ~500Å thick, evaporated on a 500Å thick membrane of Al_2O_3, the membrane already having a 250Å thick conducting layer of aluminium on it. The mean electron gain per dynode, defined as the number of secondary electrons divided by the number of primary electrons, is unity for impinging electrons of 3KeV energy, rising steeply to about 5 for 4KeV electrons and flattening off to a maximum of 5.5 at 4.7KeV [10]. Five secondary emission dynodes are incorporated in the standard tubes. The electron image is focussed between stages by the combined action of homogeneous co-axial electric and magnetic fields. The principle is that the transit time of the electrons across the inter-dynode gap, or between the fifth dynode and the phosphor, is made some multiple of the period of rotation which the electron has by virtue of the transverse component of its emission velocity in the magnetic field. With an overall voltage of ~37 Kilovolts (which corresponds approximately to the voltage required for maximum gain), a magnetic field of ~ 200 gauss is required to give focussed loops along the tube. The diameter of the helical trajectory for an electron of 1eV emission energy and 45° emission angle with respect to the tube axis is ~0.25mm. Overall light gains (defined as the ratio of the total light output from the phosphor to light input, for incident light on the photocathodes of the same spectral composition as the phosphor emission) of a few times 10^4 to a few times 10^5 are obtained, with average overall internal electron gains ~3000. These tubes can be pulsed for pulse lengths down to 1 μsec. as will be described in Chapter 3.

More recently, image intensifiers having an essentially similar mode of operation have been available from the English Electric Valve Co. Ltd [11]. These tubes can be supplied with tri-alkali photocathodes having responses in the 100 to 150 micro-amps. per lumen range (corresponding to 13 to 20% quantum efficiency at 4100Å); the photocathodes have a low dark current ($\sim$100 electrons per cm^2 per sec.) and have a useable area $\sim$ 25 mm. diameter. The overall operating voltage is again $\sim$37 to 40 Kilovolts, but owing to the fact that the longitudinal separation between the components is smaller, slightly higher magnetic fields ($\sim$ 360 gauss) are required for focussing.

2.3 Work of other Authors

The first syccessful application of image-intensifiers for the photography of elementary particles in a homogeneous chamber (a CsI(Tl) crystal) was reported in 1955 by Zavoisky et. al.[12,13,14] Using a single high gain tube of the 'sandwich' stage type, which incorporated a method of switching by electrostatic deflection of the electron image by parallel plate electrodes, these authors photographed tracks of stopping and minimum ionizing protons. In 1960, Demidov and Fanchenko [15], again using a single tube system and a NaI(Tl) crystal were able to photograph tracks in which they obtained half the number of spots per cm. that they expected from calculation. They attributed the discrepancy to light losses in the objective and crystal, and to uncertainties in the quantum yields of the NaI(Tl) crystal and photocathode used.

In the United States, Reynolds et al [16,17] reported the development of plastic fibres for use in filament scintillation chambers. In 1959, he and his co-workers assembled an image intensifying system consisting of a Westinghouse WX4047 electrostatically focussed demagnifying tube of gain 11, followed by three R.C.A C73458 two-stage 'sandwich' tubes with gains of 290, 930 and 125, all optically coupled, and photographed cosmic ray tracks in a plastic fibre chamber [18,19]. Reynolds has given an up-to-date account of filament scintillation chamber work at Princeton University in the "Second Symposium on Photo-electronic Image Devices (1961)" [20], and the Princeton group has recently published a paper on a completed experiment carried out with their filament chamber [21]. To check the predictions of a universal Fermi interaction, μ^--mesons were stopped in a 3.8 cm. diameter fibre chamber made up of 0.75 mm. diameter plastic scintillator fibres. About 1% of the stopped muons are absorbed by carbon nuclei to give B^{12} ($\mu^- + C^{12} \rightarrow B^{12} + \nu$), and this channel was identified by the 21 msec. half-life of its decay electron. The experiment consisted of comparing the capture rate to B^{12} with the free decay rate of the muon. Duflo [36] has studied the angular distribution of light from filaments for use in a fibre chamber, and Reiffel and Kapany [43] have discussed the factors affecting the performance of filamentary plastic scintillators.

Whilst the Princeton group was working on fibre chambers, Jones and Perl at Michigan University started on experiments with image intensifiers and homogeneous chambers [22]. They successfully photographed cosmic ray μ-meson tracks in 1959;[23] their image intensifier system, like the earlier Reynolds set-up consisted of several low gain tubes in cascade. These authors have subsequently published several accounts of their apparatus which they have gradually improved as better image tubes became available.[24,25,26] They have recently described two successful experiments.[27,28,29] These were to measure the large angle differential elastic scattering cross-section of π^--mesons on protons at 1.5, 2.0 and 2.5 GeV/c using two sets of NaI(Tℓ) scintillators 5 cm. by 5 cm. by 20 cm. each, and to study the reaction $\pi^- + p \rightarrow \pi^- + \pi^0 + p$.

An image intensifying system essentially similar to the Michigan arrangement has been used by Hill, Caldwell and Schluter [30] at M.I.T., the final R.C.A. tube of the Perl and Jones set-up being replaced by an R.C.A. intensifier orthicon system in conjunction with a Kinescope and camera. Lande et al [31] have also successfully operated a similar scintillation chamber assembly.

Goetze et al [32,33] at the Westinghouse Research Laboratories are (apart from the work described in this thesis) the only group who have used transmission secondary emission image intensifiers. In 1961, they reported the photography of minimum ionizing tracks in NaI(Tℓ) using two 4-stage tubes in cascade. The calculated number of electrons leaving the first photocathode of their system agreed within a factor of 1.5 to 2 with the photographed scintillation flash population.

At Bonn University, Geise and Gilderneister [34,35] have built a 3-stage 'sandwich' intensifier and photographed minimum ionizing cosmic ray particles in a Caesium Iodide crystal.

A recent review of scintillation chamber work has been made by Salvadori [37], and a discussion of the application of the various types of image tubes available to high energy physics has been given by McGee [38].

2.4 Scope of the Work in the Present Thesis.

The present research work is devoted entirely to the use of 'Twentieth Century Electronics' and 'English Electric' transmission secondary emission tubes for the intensifying system. Also, as work with fibre chambers had already been undertaken by Reynolds and his co-workers and as good quality fibres were not obtainable in this country, the work was confined to homogeneous scintillators. Commercially available large aperture lenses were used for all the optical couplings and photographic recording was used rather than T.V. Kinescope systems because of the simplicity and cheapness of the former.

CHAPTER 3

Preliminary Experiments

3.1 Photography of Cosmic Ray μ -mesons.

The initial effort of the research project was put into an attempt to photograph cosmic ray tracks to confirm the performance expectations of 5-stage transmission secondary emission image tubes for scintillation track photography. It was hoped that experience gained using this prototype apparatus would help to pinpoint the difficulties and defects of the system before a more versatile apparatus was built for use at an accelerator. Cosmic ray tracks were successfully photographed in December 1960 using a special mesh-grid image tube as the gated tube. Fig. 2(a) shows the arrangement used, and Fig. 2(b) is an example of a μ -meson track taken using this set-up. The parameters of the system were briefly as follows:-

Chamber: NaI(Tℓ) crystal 7.5 cm. diameter by 2.5 cm. thick.

Front optical coupling: Dallmeyer 150 mm. f/3.5 and Canon 50 mm. f/1.2 lenses connected face-to-face.

First image tube: Twentieth Century type VX9236, with an Sb-Cs photocathode of 35 microamps per lumen, and a P.11 phosphor.

Inter intensifier coupling lenses: A pair of Canon 50mm. f/1.2 lenses

Second image tube: Special 5-stage tube incorporating two fine mesh grids between photocathode and first dynode.

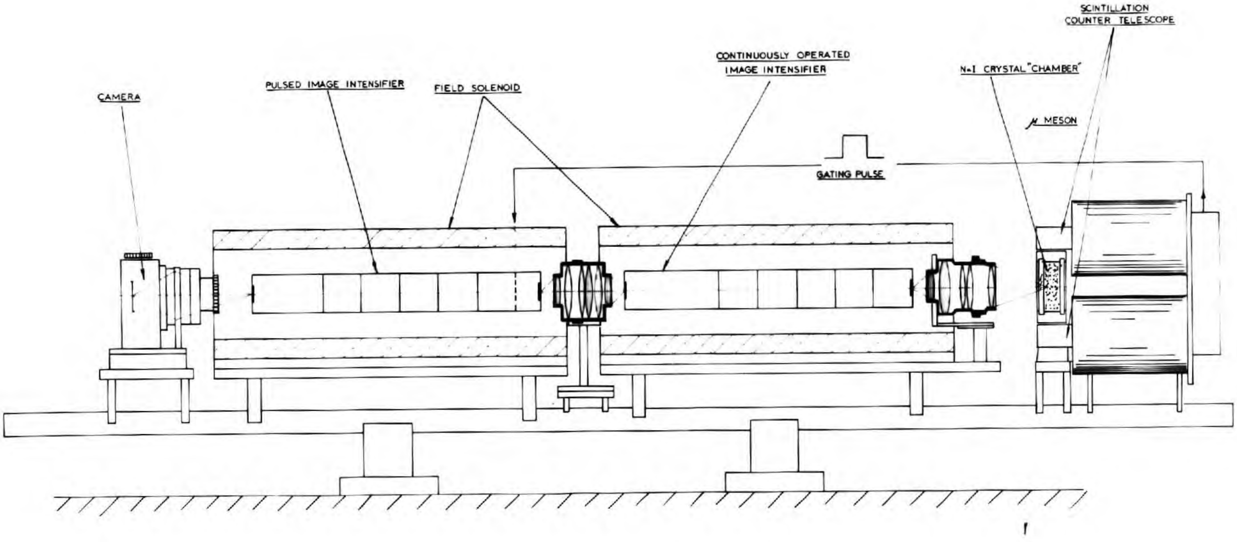

(a) HOMOGENEOUS SCINTILLATION CHAMBER

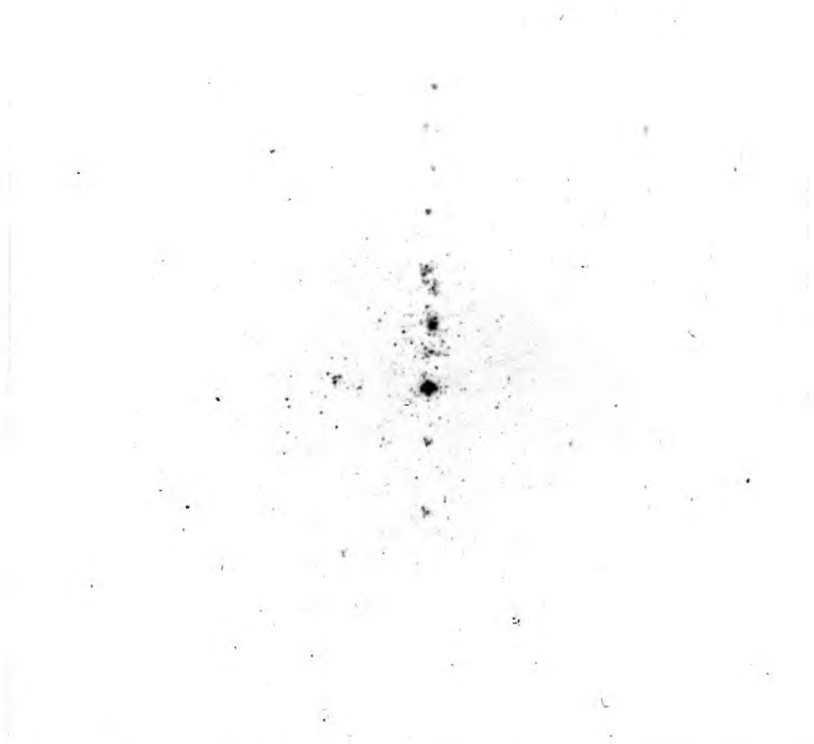

(b)

Fig.2(a). The arrangement used to photograph cosmic ray tracks in a Sodium Iodide crystal.

Fig.2(b). A track of a μ-meson in a single crystal of Sodium Iodide. The track is 7cm. long.

Photography: Final image formed by a pair of Canon 50mm f/1.2 lenses onto Kodak Tri-X film.

Unfortunately, the intensifier with meshes was accidentally destroyed before any systematic experimentation could be carried out with the apparatus, but the photographs taken showed that the density of points was within a factor of 2 or 3 of the number expected, and also showed up some defects in the system. Fig,2(b) shows clearly two types of vignetting of the final picture. The first was due to the optical coupling of the chamber to the first intensifier and leads to a variation in the number of photoelectrons along the track and the second was due to vignetting in the inter-intensifier and camera optics and gives rise to variation in photographic density of the final image discs.

Immediately after the feasibility of using transmission secondary emission tubes had been confirmed, more comprehensive tests were carried out to find the most suitable lenses for optical couplings, the most suitable 'memory' phosphor, and some method of gating conventional Twentieth Century tubes.

3.2 Experimental Studies on Lenses.

For inter-intensifier coupling, fairly efficient light collection is required, and the vignetting should be kept to a minimum. Since, in the final system, the first intensifier always incorporated a P.24 'fast memory' phosphor having an emission spectrum peaked at 5000Å there was little loss of signal by absorption. The resolution and distortion should be such as not to degrade the image quality at the previous phosphor. Similar requirementsapply in the case of the camera coupling optics.

The spectrum of the scintillation light from the phosphors used as luminescent chambers has a width of a few hundred Ångstroms, with peak wavelengths ranging from 3950Å in the case of scintillating glass to 4200 - 5700 for CsI(Tℓ). Thus the initial coupling optics must be a large aperture system, with good transmission characteristics at the blue end of the spectrum. Vignetting must be kept to a minimum since preservation of the low intensity primary photon signal over the field is of crucial importance at this stage.

The transmission properties of a number of commercial large aperture lenses were measured for different wavelength light, and the vignetting for off-axis rays was also determined. Values for the transmission were obtained by measuring the attenuation of a weak axial pencil of light from a monochromator, using a photomultiplier as the light detector. The vignetting tests were performed by using essentially the same technique, the wavelength now being kept constant, but the angle end position of thepencil ray with respect to the principal axis of the lens being varied. The results are summarised in Appendix C, which also includes similar measurements made by other authors on lenses which might be suitable for use in a scintillation chamber system.

It was decided to use a pair of Dallmeyer 4" focal length f/1.9 "super six" anastigmat lenses for the inter-intensifier and camera coupling optics. If thephosphor emission is assumed to be Lambertian, this lens combination collects 7% of the emitted light. With 5 stages of secondary emission multiplication preceeding the first tube phosphor there should be a sufficient signal at this stage to relax the optical coupling efficiency between the intensifiers and still have an adequate photo-electronic yield at the second photocathode. The field diameter covered is 2 cm so that the maximum angle subtended is 5°, at which angle the signal is reduced to ~ 80% of the axial intensity for these lenses.

A number of lens combinations were used for coupling the chamber to the first photocathode so that a variety of demagnifications could be employed. Table D gives the properties of the combinations used to cover demagnifications from 1.5 : 1 up to 4 : 1.

3.3 Phosphor decay-time characteristics

A series of experiments were carried out by Mr. M.R.Jane to find the most suitable phosphor for use as the "memory" phosphor in the first image tube. As was explained in the first chapter, the main requirements for this phosphor are that it should have a short decay time (~ few μsecs) and no 'long-tail' decay. The experiments consisted of pulsing a number of cathode

Lens combination.	Demagnification	Back f/number [see appendix A and Fig 31 for definition]	Transmission with wavelength.	60 % vignetting radius in mm. [measured in the image space]
Canon 50mm. f/1·2 + Dallmeyer 82·5mm f/1·9	1·58	1·2	~45% at 4050Å ~55 % at 4350Å	6mm.
Canon 50mm. f/1·2 + Dallmeyer 152mm. f/3·5	2·9	1·2	~45% at 4050Å	9mm.
Wray 50mm. f/1	4·0	1·25	57% at 4050Å 65% at 4350Å	11mm.

TABLE 'D'

ray tubes having different phosphor screens, and viewing the electron gun spot with a photomultiplier. The photomultiplier output was displayed on an oscilloscope whose time base was triggered every time the C.R.T. was switched on. The main decay time of thephosphor was obtained directly by pulsing at a repetition rate of a few per second. A measure of the amount of light present in the 'long-tail' of the decay was obtained by observing the shift in the D.C. level of the trace on the oscilloscope when the C.R.T. was pulsed at a fast rate.

Of the standard phosphors available, three have nominal decay time characteristics which would be suitable in an image intensifier system; these are P.15, a ZnO phosphor which decays to 10% of the initial brightness in 3 µsec. and has a double peaked spectral output (4000Å and 5000Å); P.16, a Calcium Magnesium Silicate: Cerium phosphor which decays to 10% in 0.12 µsec., spectral peak at 3750Å; and P.24, a Zinc Sulphide phosphor with spectral peak at 5000Å, and 1.5 µsec. decay time to 10% of the initial brightness.

The experiments showed that P.16 was the 'cleanest' phosphor, and could be used under pulsed operation up to 250 Kc/sec. with 1 µsec. pulses for a signal to noise ratio (defined as the ratio of the amount of light due to the short-lived component to the amount due to the long-lived component during the 1 µsec pulse) of 10. The corresponding figure for the P.15 and P.24 phosphors was ~ 30Kc/sec. Transmission tests of the phosphor light through a pair of Dallmeyer 4" f/1.9 lenses showed that 20%, 37% and 60% respectively of P.16, P.15, and P.11 phosphor light was transmitted; although no measurements were made on a P.24 phosphor, it would be 60% or better because it peaks at 5000Å compared with 4500Å for a P.11 phosphor. This result, coupled with quoted average absolute efficiencies for these phosphors [39] indicated that the effective efficiency of P.16 would be a factor of between 10 and 20 down on a standard P.11 phosphor, whereas the P.24 would be down by a factor of 3 to 5 on a P.11 phosphor. Since it is important to maintain a reasonable signal level of photo-electrons at the second photocathode it was decided to use P.24 phosphors on all the first tubes to be used in the system. The fluxes of particles which were used in the Saclay experiments were so small that the effect of the slight 'long-tail' of this phosphor was negligible.

3.4 Gating of a standard Twentieth Century Electronics Image tube.

Originally, the only image tube of the secondary emission type having switching facilities was a special 5-stage tube made in the Instrument Technology department of Imperial College; this was the tube used in the cosmic ray track photography described in section 1. This tube had two wire-mesh grids between the photocathode and first dynode. The added complication of mounting two fine wire meshes, however, made the chance of getting a useful tube quite low. The only satisfactory tube made had a resolution of about 7. ℓp./mm., could be switched in times $\sim 1\,\mu$sec., and had an opacity (defined as the probability that a signal photo-electron gets through the mesh grids onto the first dynode and is thus amplified) of 10^{-7} under favourable operating conditions. Because of the many difficulties and delays encountered in making the mesh-type trigger tube, experiments were carried out in an attempt to use a standard 5-stage tube as a trigger tube.

Fig. 1 shows how a Twentieth Century Electronics tube can be used under pulsed operation. The photocathode is held at a potential of several hundred volts (suitable operation was obtained over a fairly wide voltage range; 500 to 900 volts), and the second cylindrical ring electrode is held at a variable potential, approximately half-way between earth and the first dynode potential. It was then found that the potential of the first ring electrode effectively controls the flow of photo-electrons to the first dynode.

With the photocathode at 750 volts, virtually no photo-electrons penetrated to the dynode if the first ring was at a potential of less than 20 volts positive; the transmission factor or opacity was less than 10^{-7}. As the potential of the first ring was gradually increased (i.e. effectively static operating conditions), the photo-electrons began to penetrate in appreciable

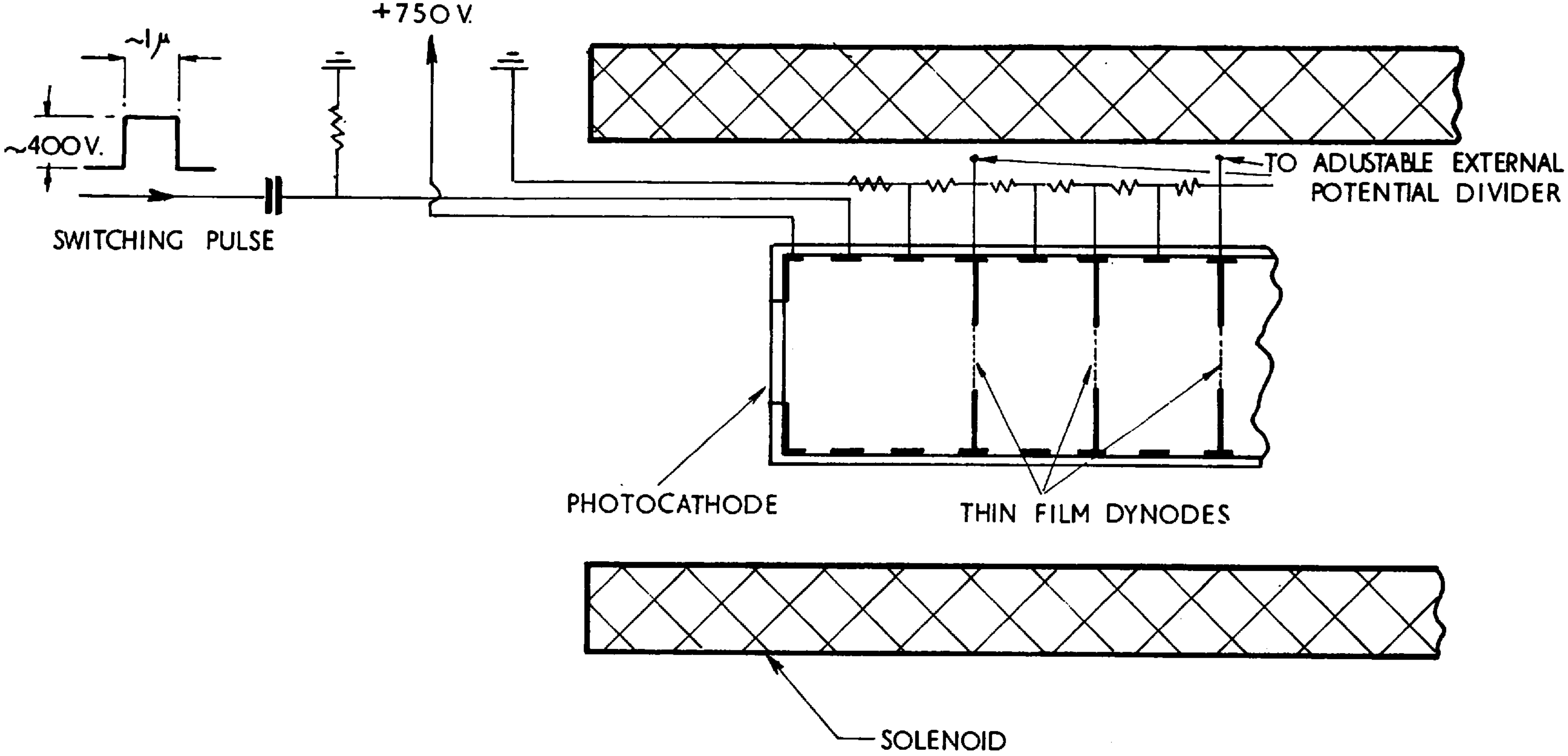

FIG. 1. 'TWENTIETH CENTURY' TUBE UNDER PULSED CONDITIONS

numbers at about 70 volts. The electrons getting through were at first confined to a small irregularly shaped region; in the particular tube used, the penetration area appeared first on one side of the sensitive area, gradually growing in size until it covered the whole sensitive area. The complete effect took place over a voltage change of about 20 volts on the first ring, and can be understood qualitatively in terms of the change in shape of the equipotential surfaces due to the various electrodes of the system. At first, only the higher energy photo-electrons get through; thus, 3eV electrons get through if there is a "hole" in the corresponding equipotential surface. As the voltage of the control ring is increased, this "hole" increases in size, and a hole appears in a slightly lower equipotential surface, allowing slightly lower energy photo-electrons through to the dynode.

The detailed shape and growth of the penetration area is unique for any particular tube, and depends on the geometry of the electrodes, but the overall change which constitutes the switching action is very comparable for different tubes.

There is gross S-distortion of the image at low voltages, but this improves gradually as the voltage on the first ring is increased; the image goes through a series of focii with increasing voltage and both resolution and distortion improve. When the same potentials were applied under pulsed conditions, it was found that the tubes could be switched successfully down to pulse lengths of 1 μsec., but the resolution under pulsed conditions was never equal to the 'static' resolution.

CHAPTER 4.

The Experimental Set-up at Saclay

4.1 The Experimental Facilities at the "Saturne" Accelerator.

The experiments on the photography of scintillation tracks, Cerenkov light and beam profiles were carried out at the "Saturne" proton synchrotron of the French Atomic Energy Centre, Saclay, near Paris. The synchrotron accelerates protons up to energies of 3 GeV, and the particle beams were obtained from four target blocks which were introduced into the primary circulating proton beam as required. The intensities of the beams depended on the main circulating beam intensity and on the fractions of this intensity taken by the individual targets.

The test experiments to be carried out required only a rather crudely focussed low intensity beam. Because the experiments involved many changes of optical coupling lenses and substitution of scintillation chambers in the case of the scintillation track and beam profile runs, and required variation of gas pressure for the Čerenkov experiments, the actual runs were usually fairly short and no exact programme of running time could be worked out beforehand. For these reasons the experiments were carried out using a parasitic beam of particles. The most convenient beam of this type was the particle beam coming off at 47°30' from the target in the second straight section (S.D.2) of the accelerator ring. This target was being used for a 35 cm. hydrogen bubble chamber experiment so that particles were available during any of the long scheduled runs of the bubble chamber experiment. Details of the parasitic beam that was set up are given in the next section.

The other important requirement for the image intensifier system was that there should be no large disturbing magnetic fields, either from the accelerator ring magnets, or from bending magnets and other equipment in the experimental hall. From this point of view, the "Saturne" accelerator was particularly 'clean'; the value of the accelerator magnetic field fell off to a few hundred gauss very close to the ring, and was less than 1 gauss in the blockhouse where the image tubes were operated. The largest contribution ($\sim$ few gauss) to the stray magnetic field in the vicinity of the image intensifiers came from the bending magnet used for the momentum analysis of the parasitic beam. Since the intensifiers were shielded for successful operation in transverse fields of up to 50 gauss, the external fields never affected the performance of the intensifier system.

4.2 The Particle Beam

A sketch of the 47°30' beam that was set up is shown in Fig. 3; this sketch also shows the relative positions of the bending magnetic, blockhouse and image intensifier system. The target employed for the bubble chamber experiment was a rectangular copper block, 8 cm. long in the direction of the circulating beam, 1 cm. deep and 4 mm. high; its projected dimensions when viewed

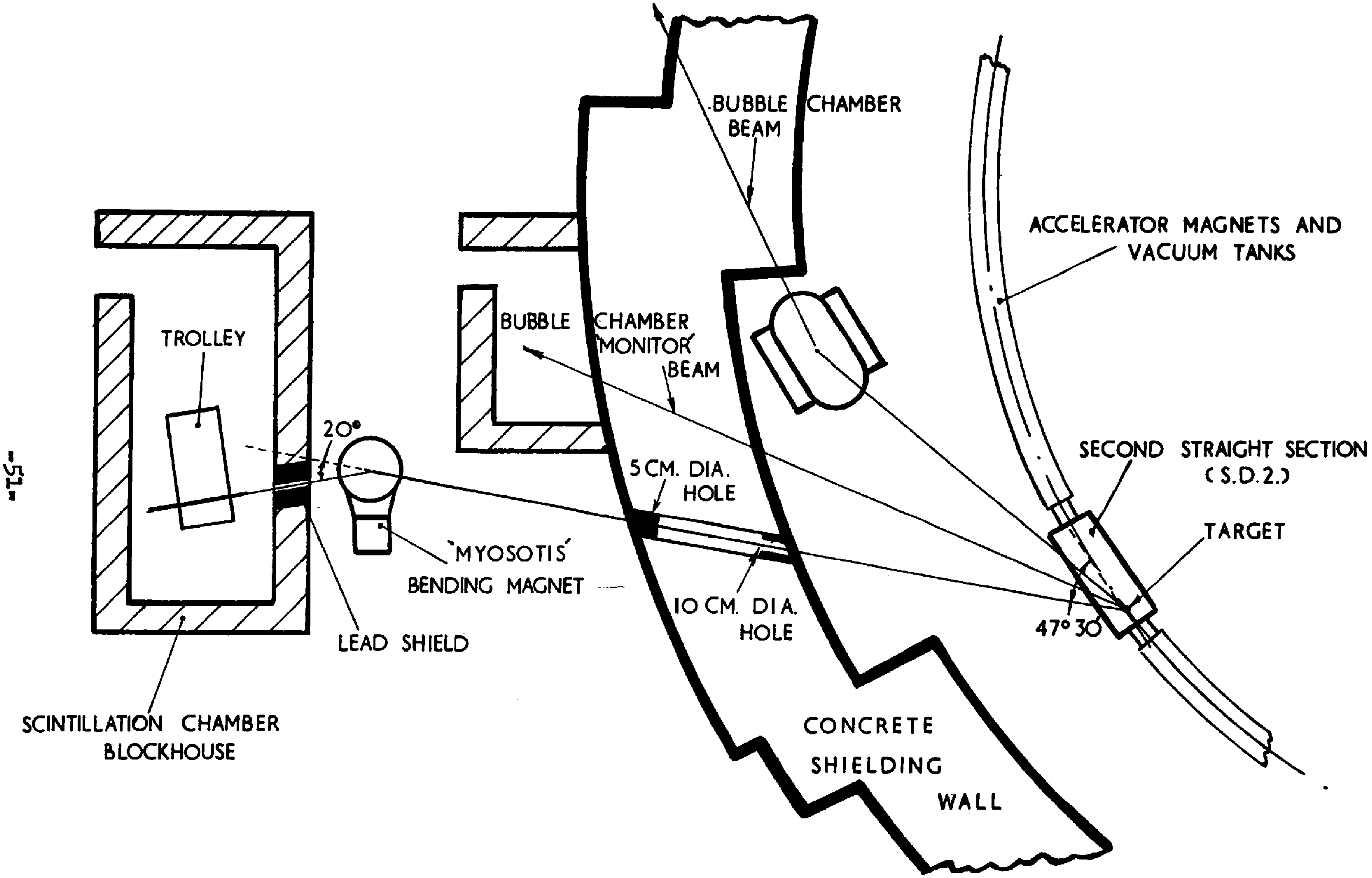

FIG. 3. THE 47° 30' PARASITIC BEAM AT SACLAY

at 47° were 5.8 cm by 4 mm. due to the presence of the concrete shielding wall and other apparatus in the experimental hall, the total distance from the target to the scintillation chambers was 18.5 metres. Apart from the bending magnet, the only other electron-optical device available was a standard quadrupole unit of 15 cm. aperture situated immediately in front of the shielding wall, at a distance of 5.2 metres from the target. Little gain in intensity compared with simple geometrical collimation, can be obtained by using just one quadrupole in this position, because the highly magnified image produced in the vicinity of the chambers would largely cancel out the effect of the increased solid angle of collection of the quadrupole lens. Moreover, the momentum spread of the particles incident on the 2 cm. chamber width would be much worse using the quadrupole lens because of the increased overlapping effect of the magnified images of particles of different momenta.

The simple collimating system shown in Fig. 3 was used, the collection being sufficient to give a reasonable intensity for all the particles at the energies and energy spreads needed. It was decided to work at a bending angle of 20° throughout the experiments, and in order to have sufficient bending power for the highest momenta required (about 1 GeV/c), special iron discs were strapped between the pole pieces of the magnet to increase the magnet flux. The magnetic properties of the bending magnet were measured using the standard facilities at Saclay; Fig. 4 is a graph of the magnetic field in the median plane at the centre of the pole pieces as a function of the current. A series of contour plots of the variation of the field over the pole pieces were made at three representative currents, and the bending power of the magnet was calculated using an analogue device [40] known as the "bug". Working at a fixed bending angle of 20°, the computed momentum scale which corresponds to the field strength at the centre of the magnet is given on the right-hand ordinate of Fig. 4.

Some simple approximate calculations can be made to estimate the momentum resolution and expected intensity of the beam. The collimation produced by the final collimating hole of 5 cm. diameter and the projected target size of 5.8 cm. gave a maximum angular spread of less than $\frac{1}{4}^{\circ}$ in the beam particles incident on the bending magnet, with a beam width of 5 cm. The momentum analyzed particles were required to pass through a chamber 2 cm. wide so that the maximum angular spread of particles passing through a chamber was $\sim 1^{\circ}$. If the $\frac{1}{4}^{\circ}$ spread in the pre-bending magnet beam is neglected, the momentum 'bite' accepted at the chamber is approximately contained by all particles bent through 19° to 21° (i.e. $\sim 5\%$ momentum resolution).

Total particle flux measurements from a similar target and made at the same angle gave a total count of 1000 ± 50% particles

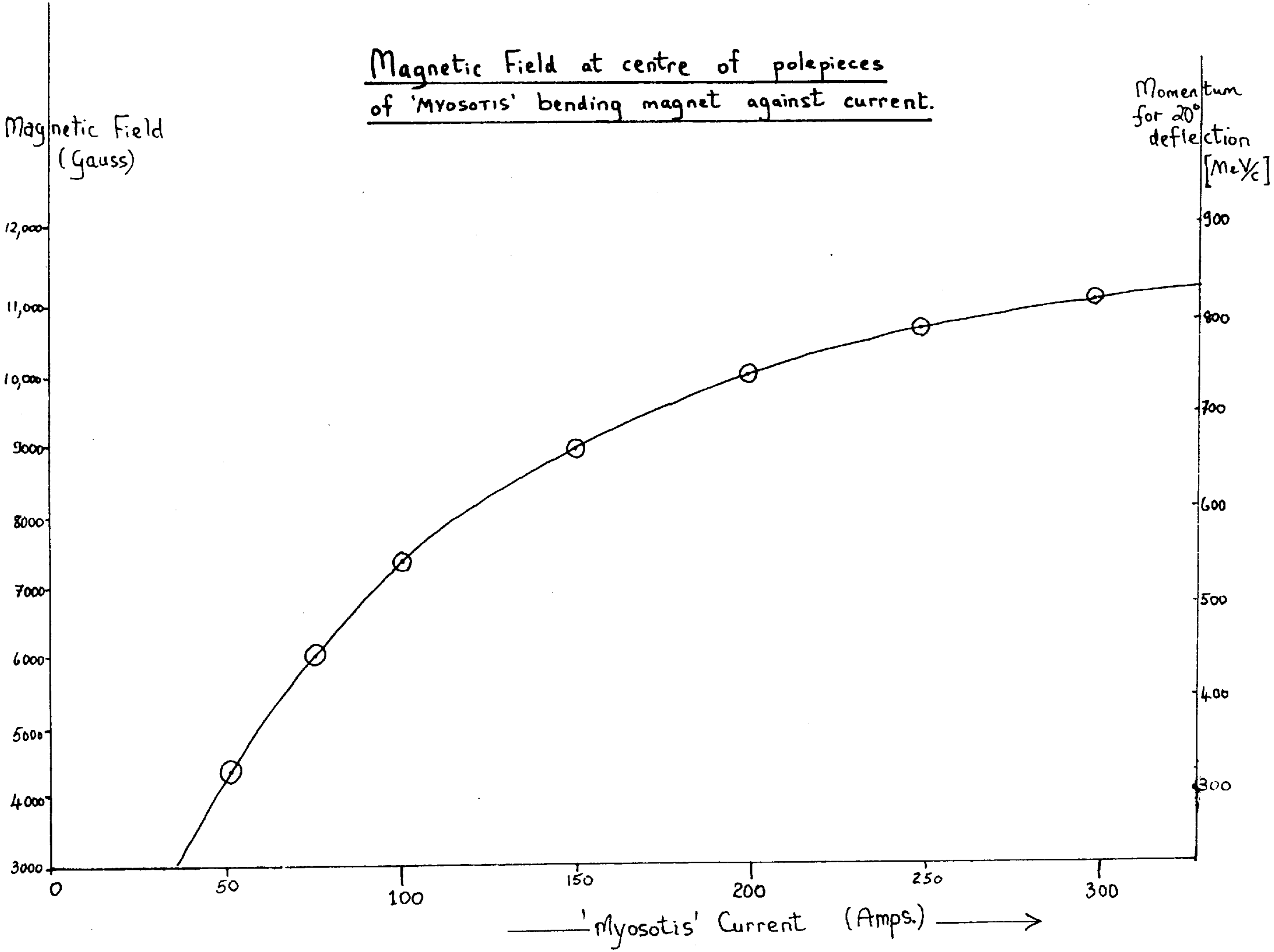

Magnetic Field at centre of polepieces of 'MYOSOTIS' bending magnet against current.

Fi- 4

per 10^{10} circulating protons in the machine, with a roughly triangular shaped energy spectrum going from zero flux at low momenta to a peak at about 300 MeV/c and falling off to zero again at ~ 1 GeV/c [41]. This figure refers to the solid angle collected by a 2 cm. diameter counter at a distance of 10.5 metres from the target, and the corresponding number for the beam described in this section would be 2500 ± 50%. Assuming a similar energy spectrum, about 100 particles per 10^{10} circulating protons would be expected in a ±5% momentum 'bite' at 300 MeV/c.

4.3 The Image Intensifier Trolley.

The image intensifying system was mounted on a moveable rectangular box framework, known as the trolley. This trolley was constructed of 3" by 3" rectangular dural angle girder, the overall dimensions being: length, 6 ft., width, 3 ft., height, 3 ft. Two decks were formed on the trolley by bolting duralumin sheets to the top and bottom of the dural framework. The trolley was mounted on large rubber-lined roller-bearing castor wheels 7½" diameter for transportation and large scale movement. When the trolley had been manoeuvred into roughly the correct position with respect to the beam, the whole assembly could be jacked off the ground by means of four large jacks mounted on the four base corners of the framework. The large castors could then be removed, and the trolley could be lowered to the correct height. For final positioning, small twin-wheel roller-bearing castors were swivel-mounted under the trolley. By raising the jacks a further short distance, the trolley could rest on the small castors and small adjustments to its position could be made. In this way the Saclay beam-height tolerances of 150 cm. ± 5 cm. were amply covered. Figs. 5 and 6 are general views of the trolley; the image intensifiers, camera, scintillation counters, and scintillation chamber are all on top of the framework, whilst the electronic circuits, power supplied, cooling fans and the special potential divider boxes required for the intensifiers are all below the upper deck.

4.4 Mounting and Shielding the Image Intensifiers.

The image intensifiers were housed in a cylindrically shaped casing which contained the magnetic field coils. The whole unit was designed to provide a uniform axial magnetic field for the tubes, to give adequate shielding from external magnetic fields, to allow air cooling of the coils and housing, and to give the necessary light-tightness. Fig. 7 is a schematic drawing of a vertical cross-section through the intensifier housing. A sheet of Lohys (1/16" thick), in the form of a 9" diameter cylinder, was placed around the coils in order to act as a return path for the magnetic flux due to the solenoid coils. Two end-plates of Lohys and mild steel were also used. The whole system was surrounded by a mu-metal cylinder 1/16" thick of 12" diameter which was intended to act as a screen against transverse external

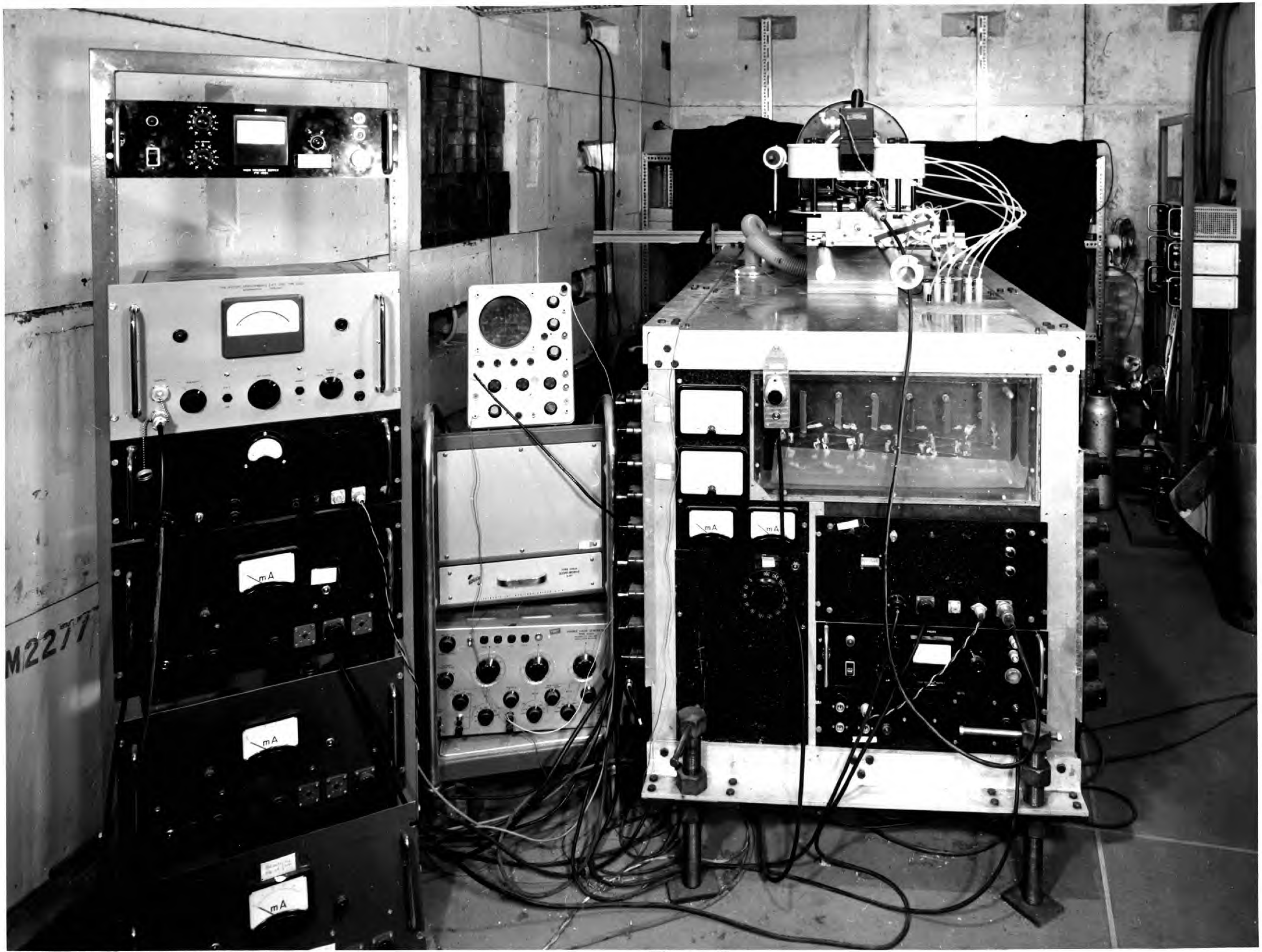

Fig. 5.

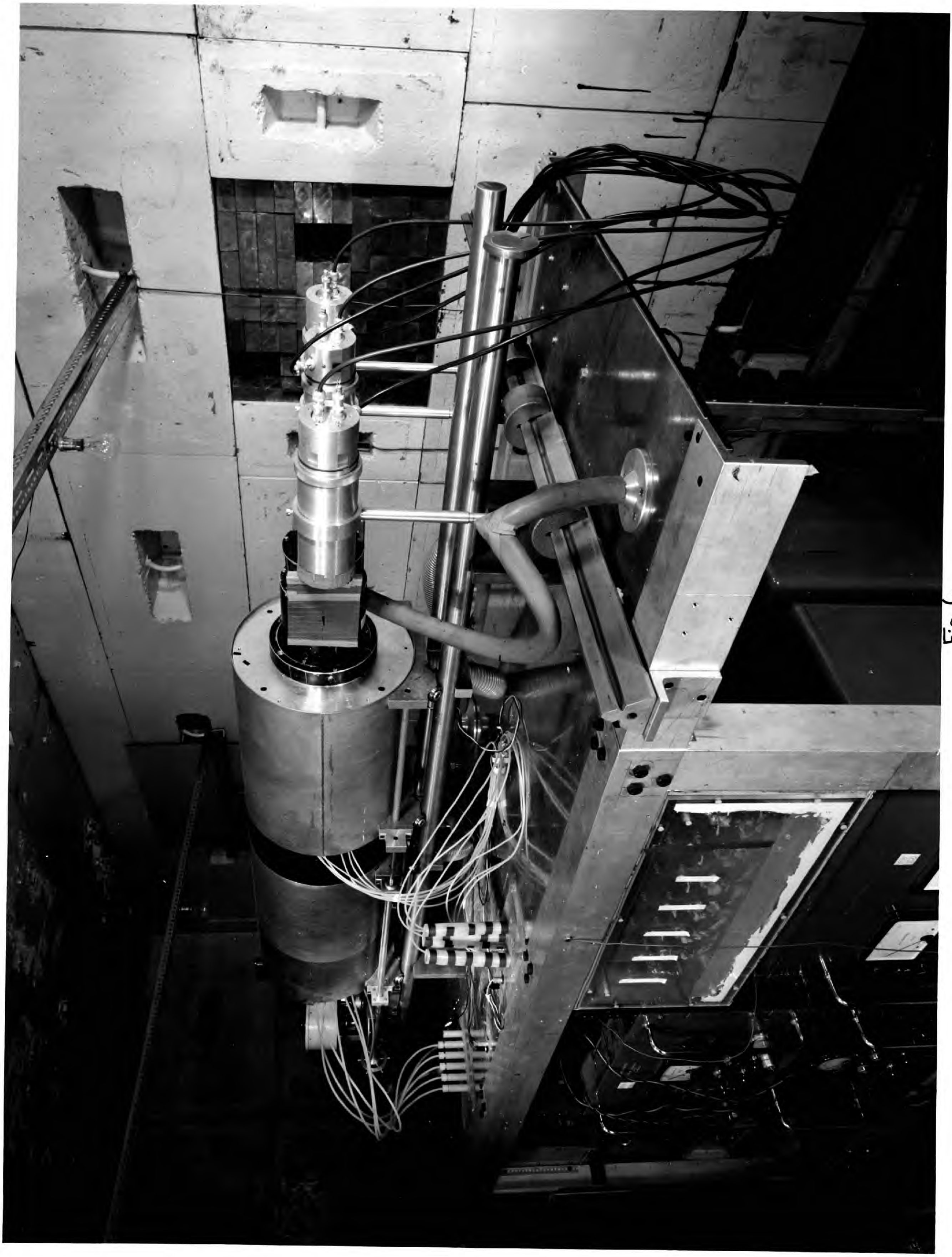

Fig. 6.

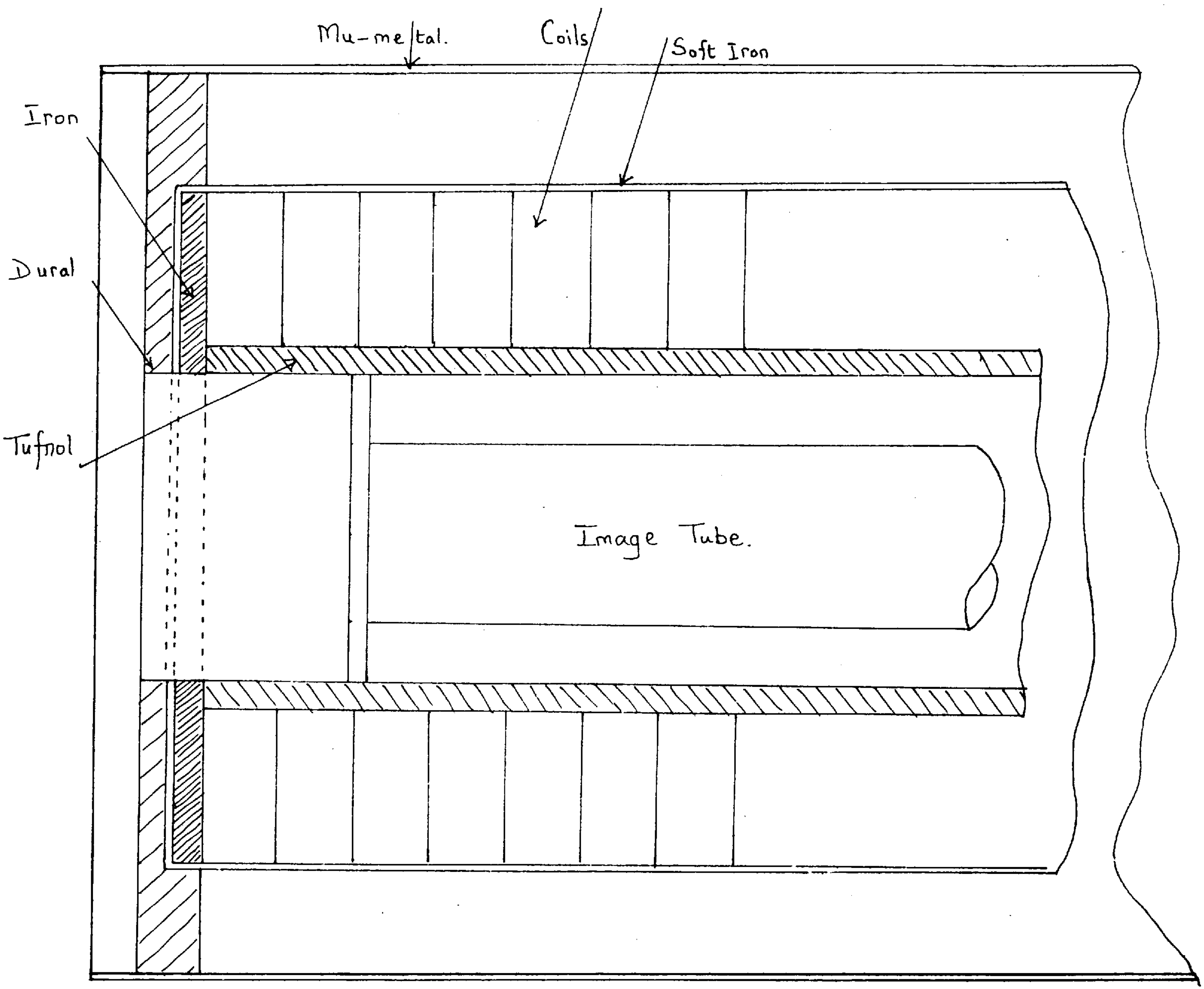

Fig. 7.

magnetic fields. In measurements made by Mr. D.C. Potter, the percentage of return magnetic flux in the Lohys and mu-metal for a current of 300 milliamps. passing through the solenoid coils were found to be 72% and 26% respectively. Fig. 8 shows the relation between the external field and the field on the image intensifier axis. It is seen that external fields of up to 20 gauss are reduced to a few hundredths gauss at the image intensifier axis, which is entirely satisfactory.

The image tube magnetic field was provided by 17 coils (15 in the case of English Electric tubes) in series. For the Twentieth Century tubes, thirteen (3rd to 15th inclusive) of these coils had a turn density of n, the 2nd and 16th coils had a turn density of 1.5n, and the 1st and 17th had a turn density of 2n. The total length of these coils, together with the two end-plates was about 20" and Fig. 9 shows the variation of magnetic field along the axis, integrated over the internal area of the Tufnol tube which was placed inside the coils. The graph shows that the magnetic field at the photocathode (which was approximately 6 cm. from the end-plates) was 95 ± 1% of the field at the centre of the intensifier. The drop in field at the photocathode would probably be less than 5% if the measurements were confined to the photocathode area, and experiments in the Instrument Technology department [42] have shown that good resolution is maintained with this variation. A smaller number

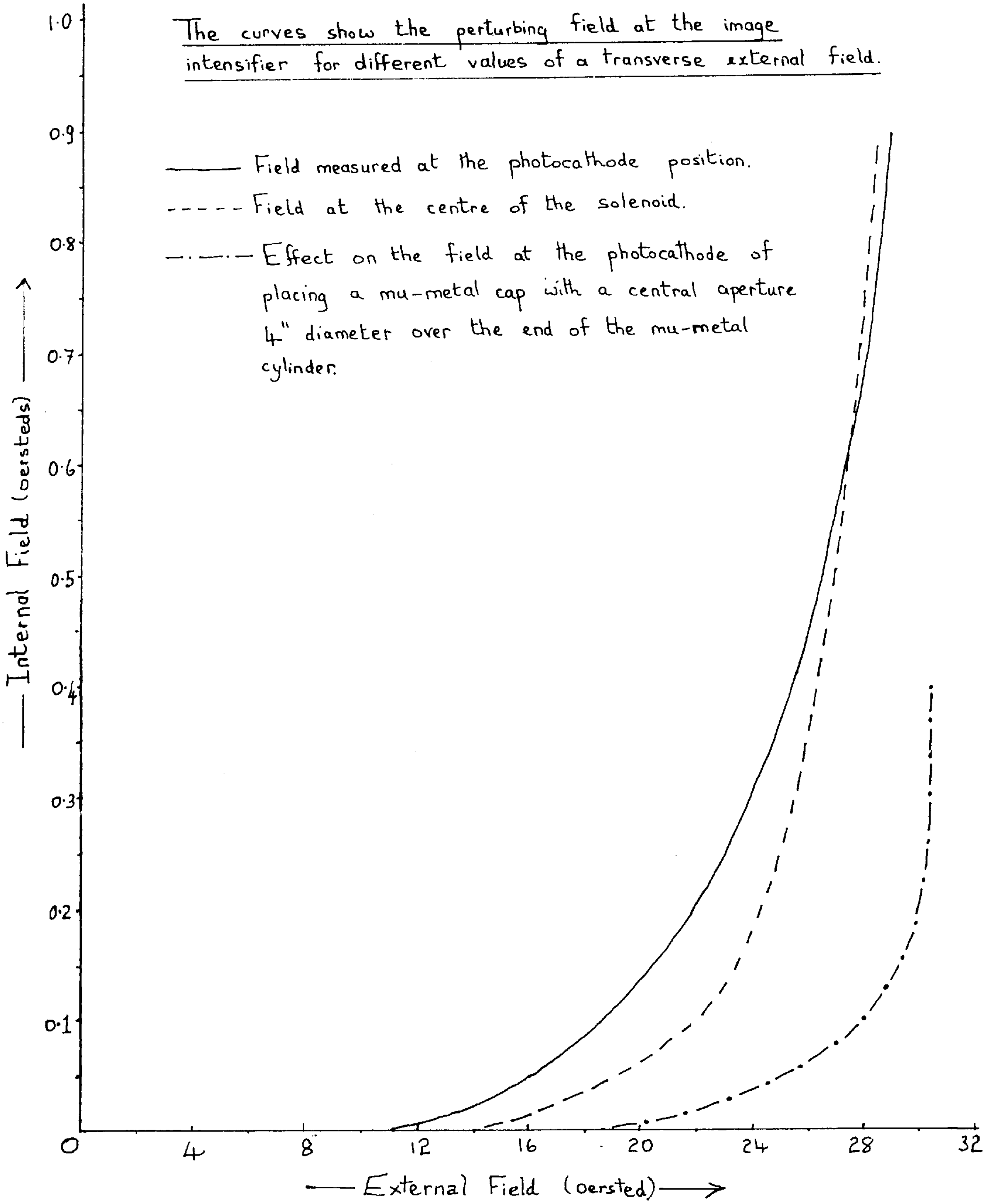

The curves show the perturbing field at the image intensifier for different values of a transverse external field.

Fig. 8.

Fig. 9.

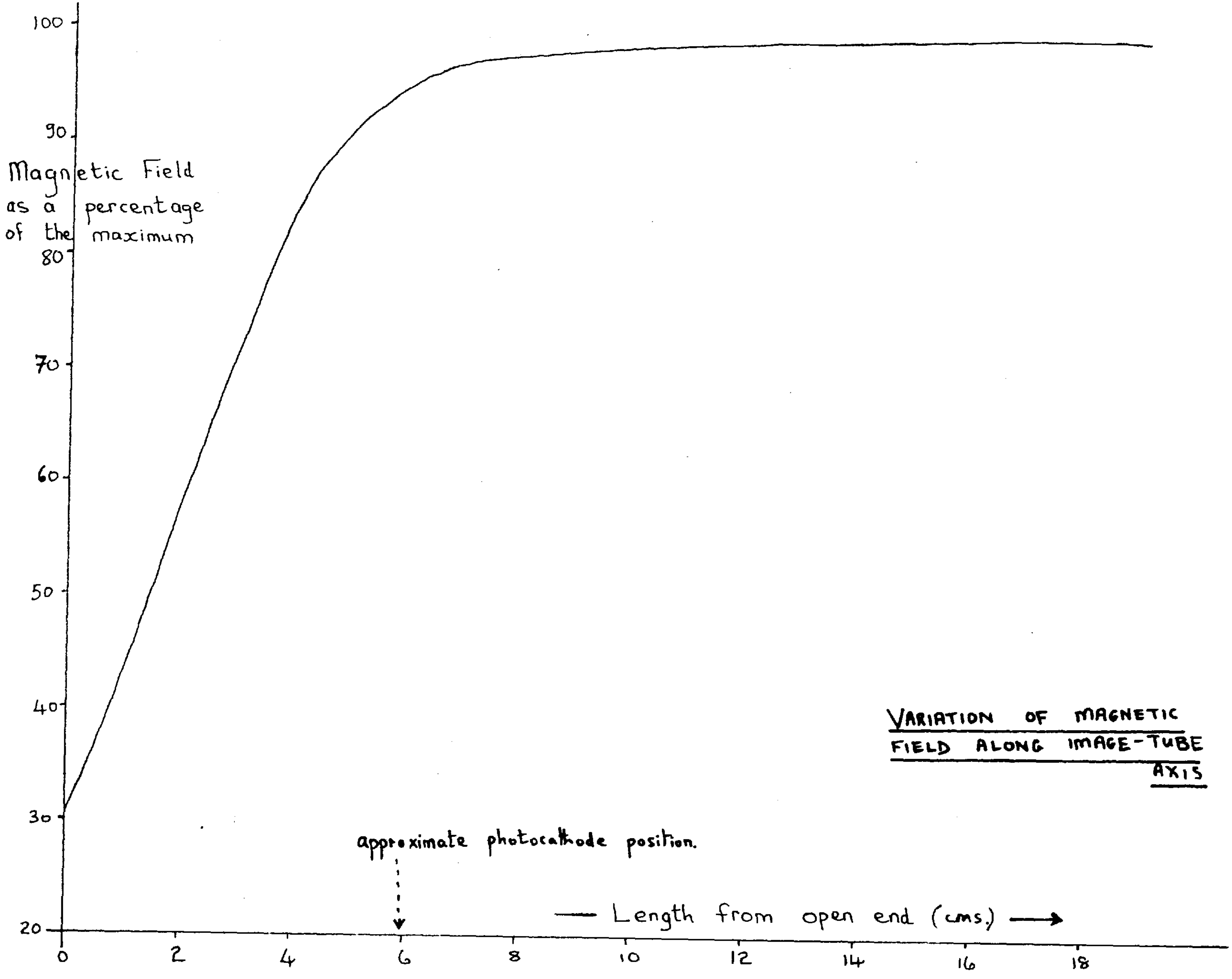

VARIATION OF MAGNETIC FIELD ALONG IMAGE-TUBE AXIS of coils made up the solenoid for the English Electric tube, but the field variation was essentially the same as above.

The twentieth Century tubes were mounted inside the Tufnol tube by means of a perspex framework and a polythene tube (see Fig. 10). The use of polythene as an insulating layer between the high voltage elements of the image tubes and the Tufnol tube gave a much quieter operation than when using the Tufnol alone. By painting a layer of 'Silastomer' silicone rubber over all bare high voltage components any tendency for corona discharge and breakdown effects was completely eliminated. Longitudinal location was provided by pressing the perspex framework against a brass stop ring bolted inside the Tufnol tube at the photocathode end. Pressure at the phosphor end of the tube was provided by means of three small dural latches pressing against the end of the polythene tube. The perspex end-pieces of the framework consisted, at each end, of two discs bolted together through enlarged holes which allowed for small transverse displacement and angular alignment of the intensifier tube with respect to the main housing axis. Later English Electric tubes were supplied completely potted in a cylindrical 'silastomer' jacket; the diameter of the silastomer was about ½" less than the inside diameter of the Tufnol so that these tubes were mounted by means of six perspex spacers (three at each end) araldited onto the silastomer. Longitudinal mounting was again achieved by pushing

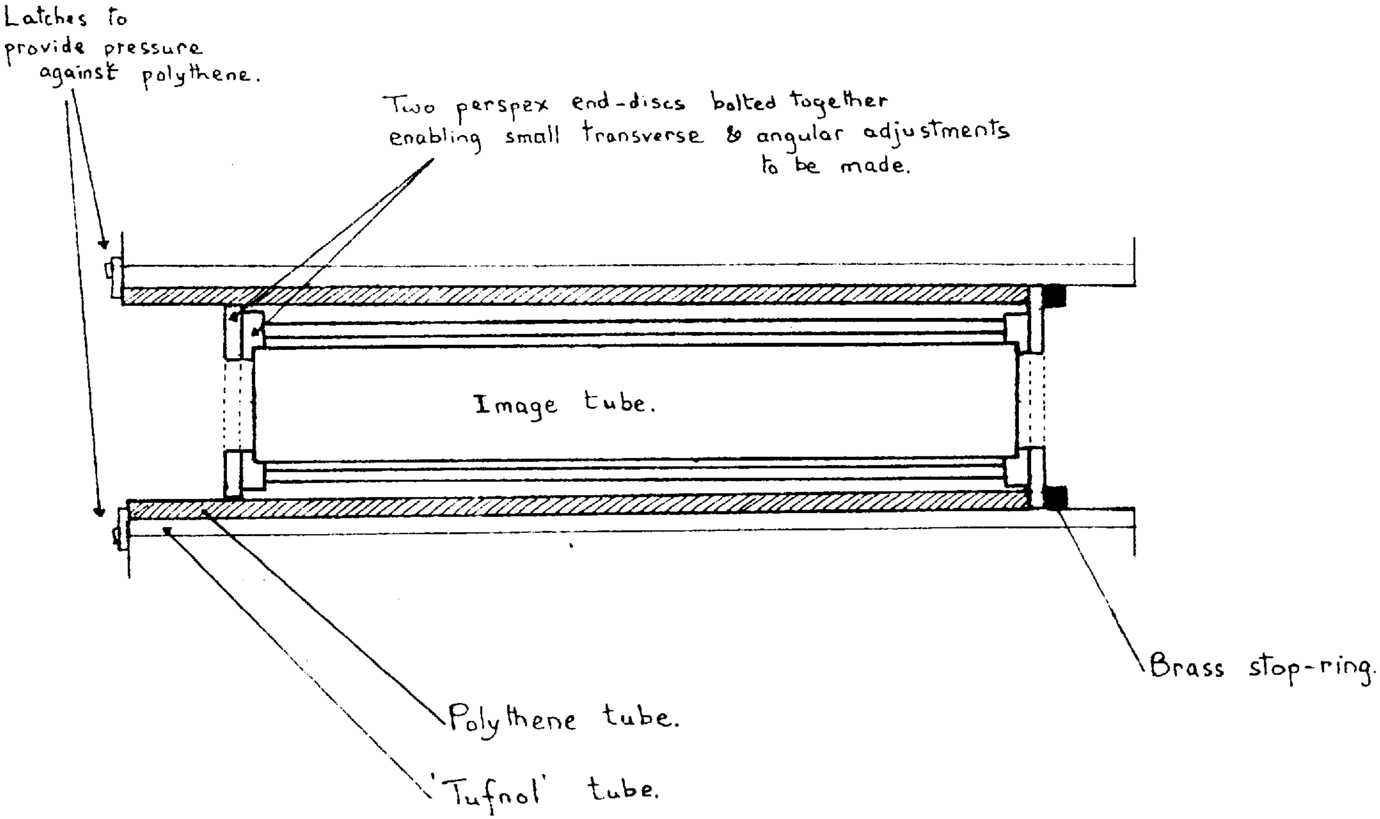

Fig.10. Method of mounting '20th Century' tube.

against a brass stop ring, the pressure being provided by three rectangular polythene strips bolted on to the faceplate of the main housing.

The main cooling air was blown in at the bottom of the mu-metal through a 2" diameter hole, emerging at the top of the mu-metal at the other end of the housing. Because of the long continuous operating periods during experimental runs, the efficiency of the cooling system was later improved by inserting thin aluminium vanes between the coils of the solenoid to facilitate the conduction of heat out of the coils. Also, an additional blower was used to blow cool filtered air along the inside of the whole intensifying system; the air entered at the photocathode compartment of the first tube and was confined to flow along the axis of the system between the tubes and the Tufnol, emerging through a light-trap after the phosphor compartment of the second intensifier tube (i.e. the one nearest to the camera).

4.5 Method of Mounting the Optical Elements

The image intensifier housings were fitted with 6 roller-bearings arranged to give accurate translational motion along an optical bench made of two parallel 1½" diameter cylindrical non-magnetic stainless steel bars. The bars which were 6" apart were mounted at a height of 15 cm. above the upper deck of the trolley, and the intensifier housings could be fixed rigidly to the optical bench by means of clamps which screwed up against the underside of the bars. The lens couplings used in the apparatus were mounted as follows:-

(a) the lens system between the chamber and first image tube was held in a focussing mount, which was bolted to the face-plate at the photocathode end of the housing. Focussing was obtained by rotating the lens, which was held in a threaded collar screwed into the main mount. Different lens mounts were necessary for the various demagnifications because of the widely differing back focal lengths and physical dimensions of the lenses used. The 1mm pitch on the collar thread enabled the lenses to be positioned to ± 3 microns, corresponding to a disc of confusion of ± 1/30mm for the optics used, but because a useful depth of field is required in the chamber volume a precise focussing adjustment is not demanded for the initial lens.

(b) Focussing of the inter-intensifier lens coupling (a pair of Dallmeyer 4" f/1.9 lenses, mounted front to front in a threaded collar) was again achieved by screwing a collar inside the main mount which was bolted onto the face plate at the photocathode end of the second intensifier housing. This coupling was adjustable to ± 3 microns and was usually preset to give 1 : 1 magnification.

The camera lenses, which were also a pair of Dallmeyer 4" f/1.9 lenses were attached to the camera body.

4.6 Focussing the Image Intensifiers.

The circuit arrangement shown in Fig. 11 was used to provide the correct electrostatic potentials for the trigger image tubes. Apart from the slightly more complicated photocathode to first dynode stage shown in this figure, an identical potential divider provided the first tube potentials. Physically, these variable potentiometric supplies consisted of high stability, high D.C. voltage rated resistors mounted in a perspex coffin, with all bare high voltage elements potted in 'silastomer' silicone rubber.

The voltage between two dynodes could be varied while the ratio of the voltages between all the other dynodes remained fixed. The change in absolute value of the voltage across all the other stages could then be taken up by adjusting the magnetic field current. Best focus was attained by a method of systematic successive adjustments of each dynode voltage and the solenoid current. The potentials of the inter-dynode accelerating electrodes were derived from a fixed bleeder chain of high impedance soldered directly alongthe outside of the tubes.

In practice, the resistance of thephosphor stage, and the current through the resistor chain were fixed, and the potentials of the remainder of the tube dynodes were varied relative to this stage. It was usual to focus the trigger tube under static conditions first, and then to apply a repetitive pulse and refocus for pulsed operation. Suitable values for the photo-

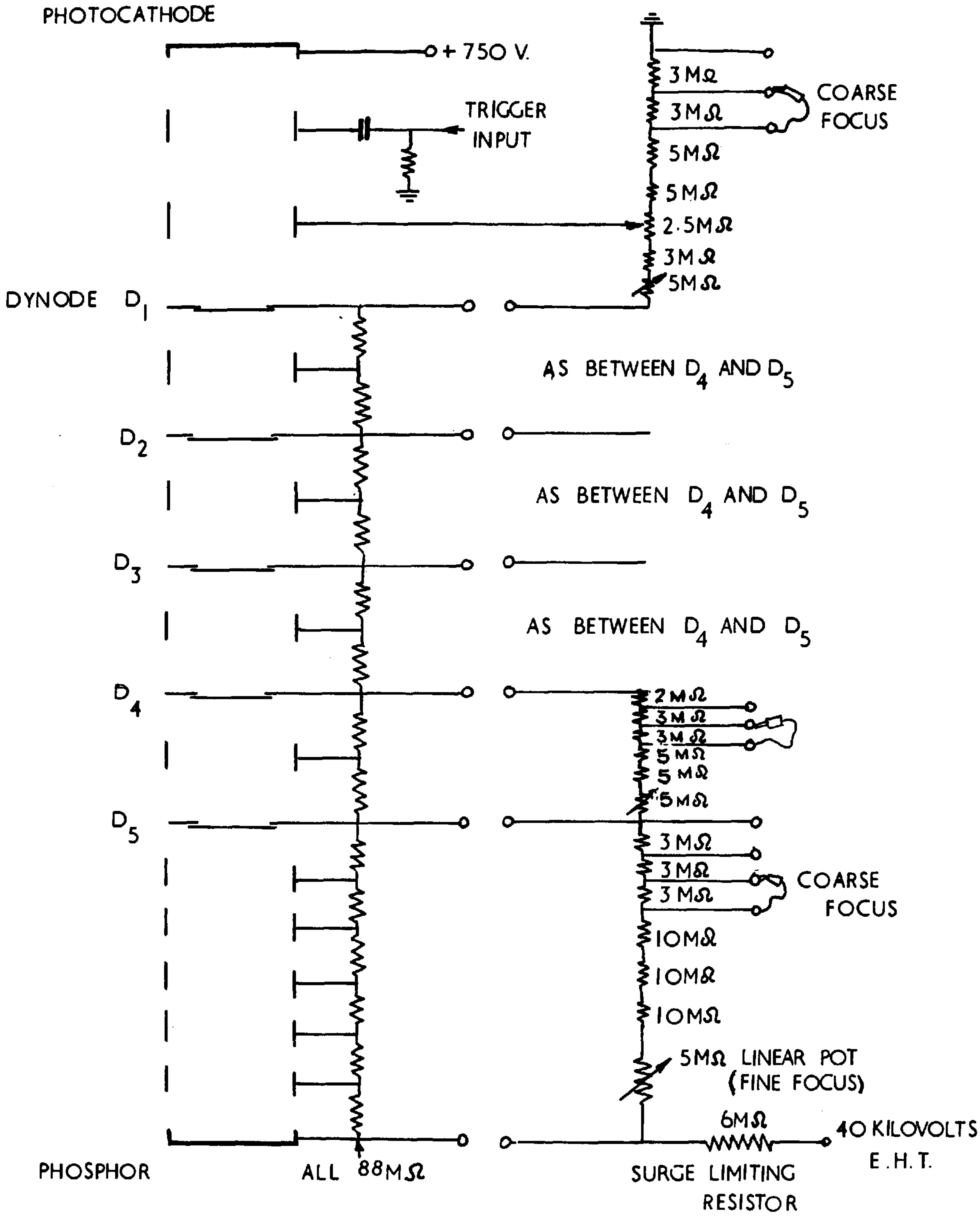

FIG. 11. CIRCUIT FOR PROVIDING THE ELECTROSTATIC POTENTIALS FOR THE TRIGGER TUBES

cathode potential and the trigger pulse amplitude could be chosen beforehand; two variables the overall voltage between photocathode and first dynode, and thepotential of the second accelerating ring electrode were still unspecified. It was desirable to keep the photocathode to first dynode voltage at a value near the optimum for secondary emission yield (between 4.7 and 5.5 kilovolts) and this left the second ring electrode potential as the final focus control.

4.7 Method of Aligning and Focussing the System.

The stages in the transference of an amplified well focussed image of the scintillation photons on to the photographic emulsion may be divided up as follows:-

(i) A sharp image of the central plane of the chamber volume at the correct demagnification must be formed on the photocathode.

(ii) The first image intensifier must give a high resolution amplified light image at the phosphor, with unit magnification, and minimum distortion.

(iii) The inter-intensifier lens coupling should give a well-focussed image of the first phosphor on the second photocathode, usually with unity magnification, but sometimes a demagnification of 5/4 was required.

(iv) The second intensifier should satisfy the conditions of (i), but under pulsed operation.

(v) A sharp image, of unit magnification, of the final phosphor signal should be formed on the emulsion.

The normal focussing proceedure was to perform stages (i) and (ii) as one operation, and the method adopted for the scintillation chamber experiments will be described here. The chambers were all 3" diameter, and between ¾" and 1" thick, and were held in a cylindrically shaped holder which also served as a light-tight and air-tight container (see Fig. 12). A large flange, A, was bolted to the faceplate of the intensifier housing so that thin-walled cylindrical holders, B, could be attached to the housing; a third component, C, was fixed to B. The chambers fitted snugly into the outer ledge of C, and were sealed at the rear by a light-tight cap, D, held firmly in place by easily detachable tension springs. The lengths of the units, B, which could be inserted between A and C gave exactly the right demagnifications for an object in the median plane of the chamber.

With the chamber and end cap, D, removed, a slide holder, E, having a faintly illuminated test chart and with micrometer adjustment could be fixed to C using the three ¼" diameter posts, F; keyhole shaped holes gave quick and accurate attachment and removal of the slide holder. The plane of the test slide coincided with the median plane of the chambers for the central position of the micrometer movement.

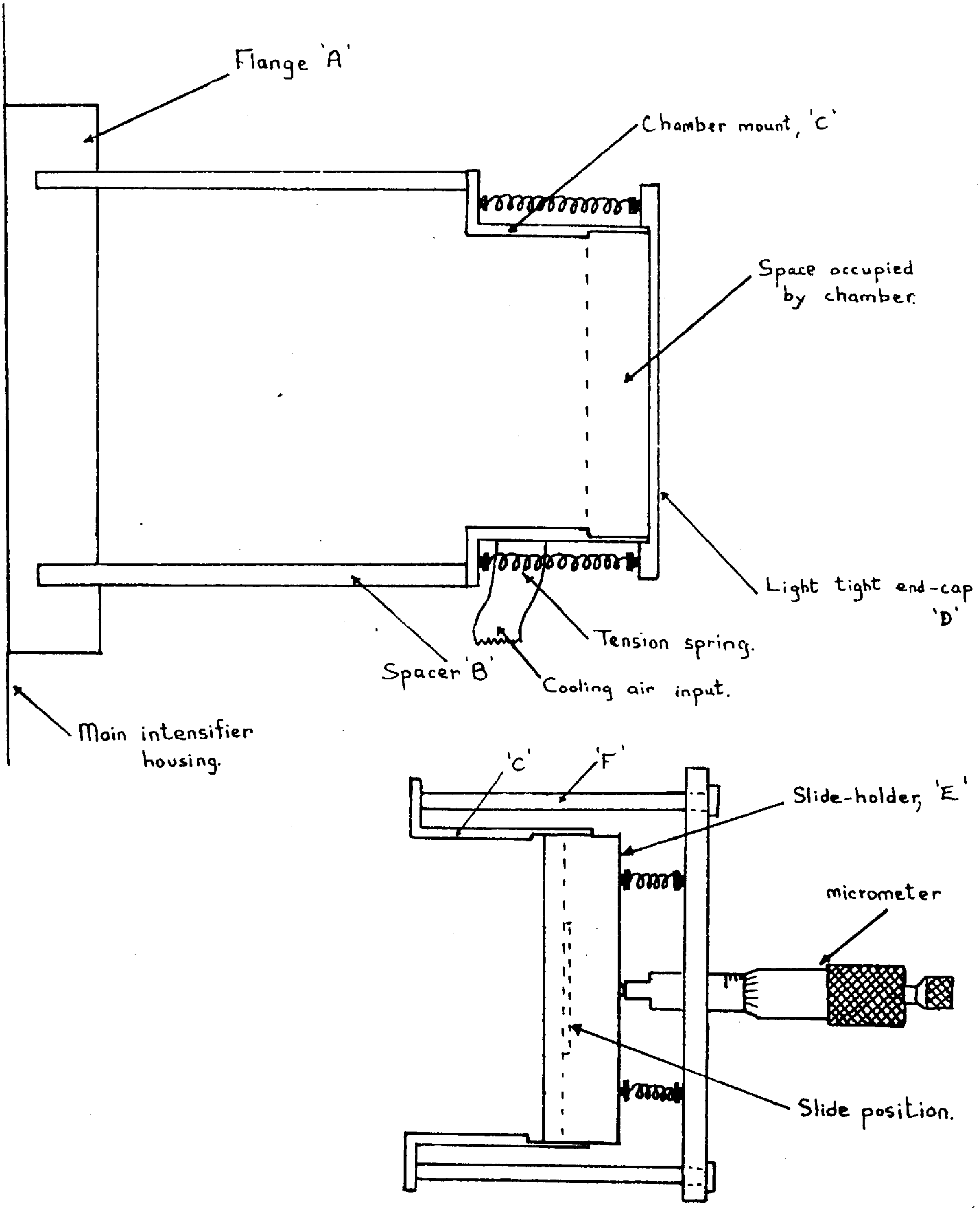

Fig. 12. The chamber and slide-holder mountings.

The first image tube had been fairly well focussed at this stage, and a direct viewing method could be used to perform stages (i) and (ii) of the focussing. With a coarse test chart in the slideholder, the approximately correct values of the magnetic and electrostatic fields were applied, and the micrometer adjustment was varied to find the rough position of the object plane for best focus at the photocathode. By adjusting the lens position, this object plane could easily be brought to within 1 mm of the median plane of the chamber, which was adequate from the point of view of the precision of the particle selection and the depth of focus in the chamber. In this position, the demagnification would be very nearly the desired value. With the gradual substitution of more sensitive resolution charts and continuous systematic adjustments of the electrostatic potentials and the magnetic field, resolutions of between 15 and 20 ℓ.p./mm. were attained at the first phosphor.

The next stage was the independent focussing of the trigger tube. A micrometer-controlled slide holder was again used to image a test chart on the photocathode, the Dallmeyer coupling lenses having been preset to give approximately 1 : 1 magnification. An outline of the proceedure for focussing the trigger tube was given in the previous section.

It should be noted that for any particular lens system, the image intensifiers have a definite position on the optical bench, corresponding to the correct alignment of the particle beam with the median plane of the chambers; the precision necessary is to within 1 mm.

Next, the two intensifiers were coupled together and the combined system was focussed by moving the second image tube and lens, as one unit, with respect to the first intensifier. A long ½" diameter screwed rod, bearing mounted to the trigger tube housing and spring-loaded to press against a ball bearing fixed to the other intensifier housing provided the intensifier spacing adjustment. Any lack of alignment between the axes of the intensifiers could be corrected for at this stage.

The inter-intensifier light-tightness consisted of a variable length light-trap formed by a thin cylindrical shell of dural bolted to one intensifier housing, which just slid between two similar concentric cylindrical shells bolted to the other housing.

A shutterless camera was used in the experiments, the electrically operated film transport being counter-controlled. Spool size of 25 ft. gave 30 minutes running time and 600 pictures at one picture per beam pulse. The camera was mounted on a special platform which had an accurate micrometer-controlled longitudinal motion on the main camera saddle. This camera saddle had three roller bearings at one end, the other end being attached to the second tube housing. Thus adjusting the micrometer affected the separation between the camera and the image tube, giving the camera focus control. The variable length light-tightness between the camera and final tube housing was provided by a thin slightly sloppy rubber membrane, circular in shape, with a circular hole in the middle. The outside edge was fixed to the intensifier face plate, and the camera lens could be pulsed through the hole in the middle, the elasticity of the rubber providing the light-tight seal around the lens.

The final best position for the camera was found by taking a series of photographs of standard test patterns for a range of micrometer settings and assessing the optimum position from the photographs. The best overall resolution attained was about 5 ℓ.p./mm at the output phosphor.

4.8 Electronic Circuits

Fig. 13 is a block diagram of the electronics used for the coincidence circuits, and for pulsing the trigger image tube. Fig. 14 gives the circuit diagram for the same circuits.

The output from a five-channel coincidence and two-channel anticoincidence circuit was fed into a discriminator-amplifier and then into the grid of an EFP60 secondary emission valve. A fast positive pulse of variable amplitude was generated at the secondary emission output of the EFP60, and provided the trigger pulse for switching the image tube. This pulse had a rise time $\sim$ 80nsec. to 400 volts, and the amplitude was controlled directly by varying the cathode potential of the clipping diode,

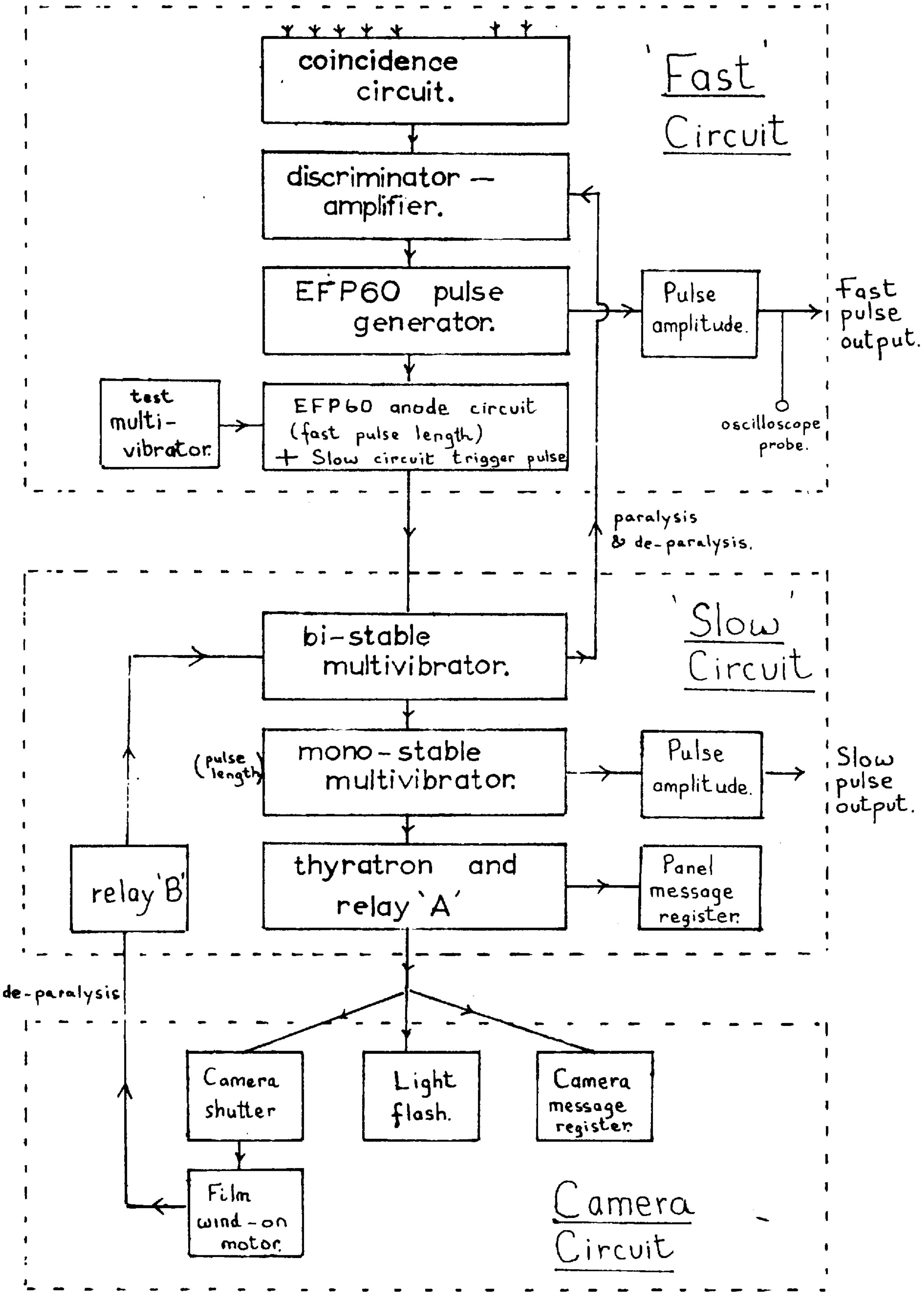

Fig. 13. Block diagram of circuits.

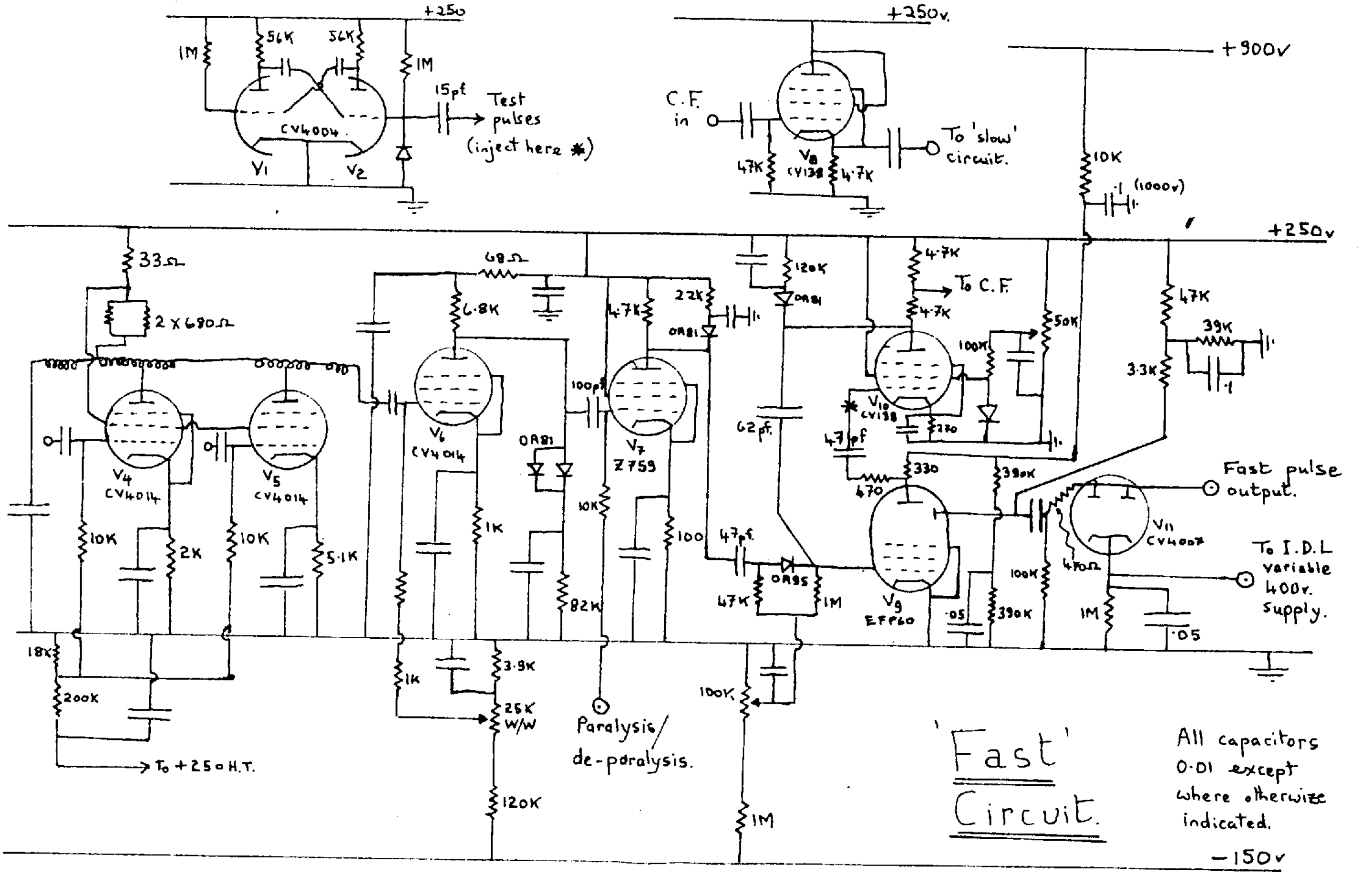

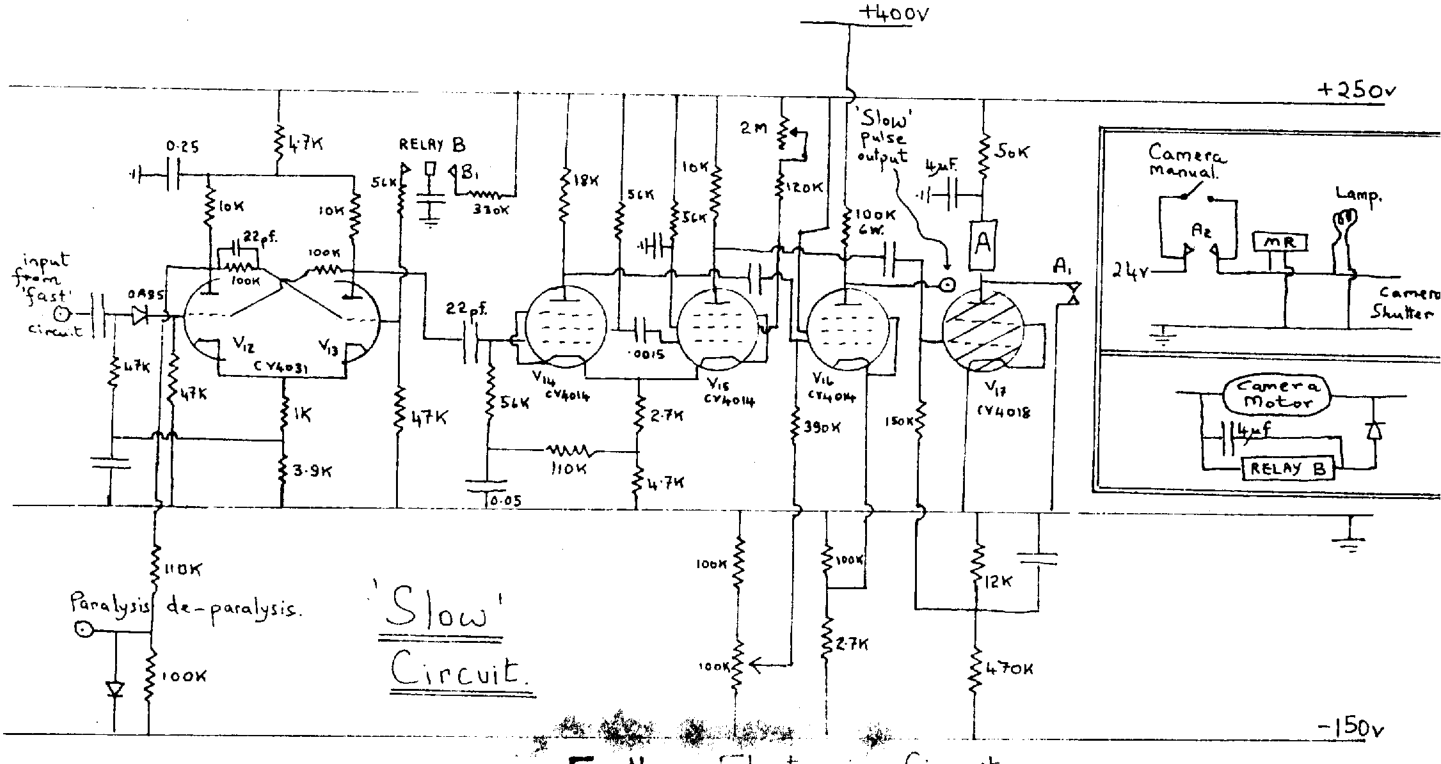

Fig. 14. Electronic Circuits

V10. The total delay, from the time that a particle traversed the chamber to the time when the trigger tube was switched on, was $\sim$ 200nsec., so that comparatively little of the P.24 phosphor light was lost during this 'switching on' period. The pulse length could be varied continuously from 1 μsec. to 12 μsec. by changing the 50K Ω potentiometer in the EFP60 anode circuit. A 20 volt pulse was available from the anode of V_{10} and this was fed into the 'slow' pulse generator/paralysis circuit. By activating a bi-stable flip-flop in the 'slow' circuit, a pulse of variable length ($\sim$msecs.) was generated by this circuit. This flip-flop also provided the paralysis and de-paralysis pulses: when a positive trigger pulse switched V_{12} on, the negative step pulse from its anode was applied at the grid of V_7, making this valve insensitive to any further signals from the coincidence circuits. The valve remained in this condition until V_{10} of the bi-stable flip-flop was switched off. V_{17} (which was a 2D21 thyratron), which was fired at the same time, activated the camera motor and operated message registers on the instrument panel and in the camera. The latter register was built into a special numbering device and two small bulbs, which were flashed on, projected a demagnified image of the digits onto the film.

By means of a two-way relay, B, fed off the rectified camera motor current, a condenser was charged up to 250 volts, and discharged into the grid of V_{13} when the camera motor was switched off. This pulse switched V_{13} on which turned V_{12} off giving the de-paralysis pulse. Thus the circuits were paralyzed until the camera had moved the film on by one frame, when another picture could be taken. Facility for switching off the paralysis pulse was built into the circuit, so that several track pictures could be superimposed on one frame before the camera meter moved the film on. Also, two manual single picture devices were provided; one enabled the camera only to be moved on, and the other injected a pulse at the coincidence stage of the circuit so that a coincidence pulse could be simulated. The trigger pulse was always monitored on a Tektronix 515A oscilloscope. Inputs were provided for injecting standard repetitive pulses from a pulse generator for focussing the trigger tube under pulsed operation.

CHAPTER 5

The Scintillation Chamber Experiments.

5.1 The Types of Picture Taken.

A series of runs were taken in which the chamber material, coupling optics, demagnification and particle ionization were all varied in turn. The other factor which affected the number of scintillation spots recorded on the film was the photocathode efficiency and recording efficiency of the intensifier system. Since different image tubes were used at different times during the experimental runs, these parameters were sometimes variable for the experiments. The ionization of the particles was in the range from minimum ionizing to three times minimum ionizing so that the response of the scintillation chambers to high energy particles could be investigated, with particular reference to the ionization information contained in the track pictures. Pictures of stopping, decaying and interacting particles were taken to test the track recognition aspect of the chambers. In the beam available at Saclay, these exposures were limited to stopping protons and stopping π^+ and π^- mesons. In the last two types of event, the e^+ from the muon decay resulting from the π^+ decay, and the nuclear interaction when the π^- mesons were captured by a nucleus were looked for. Appendix D gives the range-energy, range-momentum and energy loss-momentum curves for protons, π mesons and μ mesons in the four scintillating media used for the experiments.

5.2 The Counter Selection Methods

For 'straight through' particles of well defined ionizing power, simple two or three-fold coincidence counters were used to select the particles. Two collinating counters (typically 1 cm. by 5 cm. area and 1 cm. thick plastic scintillator) were placed in front of the chamber, with a further counter placed directly behind the chamber. The particle fluxes were such that this selection was adequate to ensure at least one acceptable particle per beam pulse, with no contamination from nearly contemporary particles. For selecting stopping protons, two collinating counters in coincidence were placed before the chamber, with a large (10cm. by 10cm.) anti-coincidence counter immediately after the chamber. This simple selection system was sufficient when used in conjunction with the correct particle momentum. The flux and time-spread of the particles was again such that one stopping proton with suitable geometry was obtained per beam pulse.

Selection of positive and negative π-mesons with momentum to stop in the central region of the chambers was difficult for two reasons. Firstly, the flux of π-mesons at the low momenta required ($\sim$100 MeV/c) for CsI(Tℓ)and NaI(Tℓ) chambers was very low, giving a useful event only every 9 or 10 beam pulses. Secondly, the bending magnet current to give the appropriate field was very small and the correct value to be used was not accurately known. A field of 1300 gauss was needed to bend the π mesons through 20°, the corresponding current being approximately 20 amps. This meant working on a part of the magnet current/magnetic field curve for which there were no experimental points. A working value for the current was obtained by extrapolating the known part of this curve to zero (this ignored any remnant magnetic field possessed by the pole pieces, or any hysteresis effects on the shape of the curve at this point). An attempt was made to optimize this working value by making visual observations of the number of stopping π mesons as a function of the magnetic field current. (The ability to observe the particle tracks in the focal plane of the camera was found to be a useful feature of the scintillation chamber apparatus, and was generally used for checking the events being photographed). Experiments in which a beam of fairly high momentum pions was degraded to the required energy by iron, lead and aluminium absorbers proved unsatisfactory because the degraded mesons were scattered over such a wide range of angles that the flux through the chambers was reduced to a very low number.

5.3 Examples of Scintillation Tracks.

Figs. 15 to 19 are chosen as representative photographs to illustrate the appearance of scintillation tracks under a wide range of conditions. It is immediately apparent that the appearance of the tracks is by no means constant, and this was a

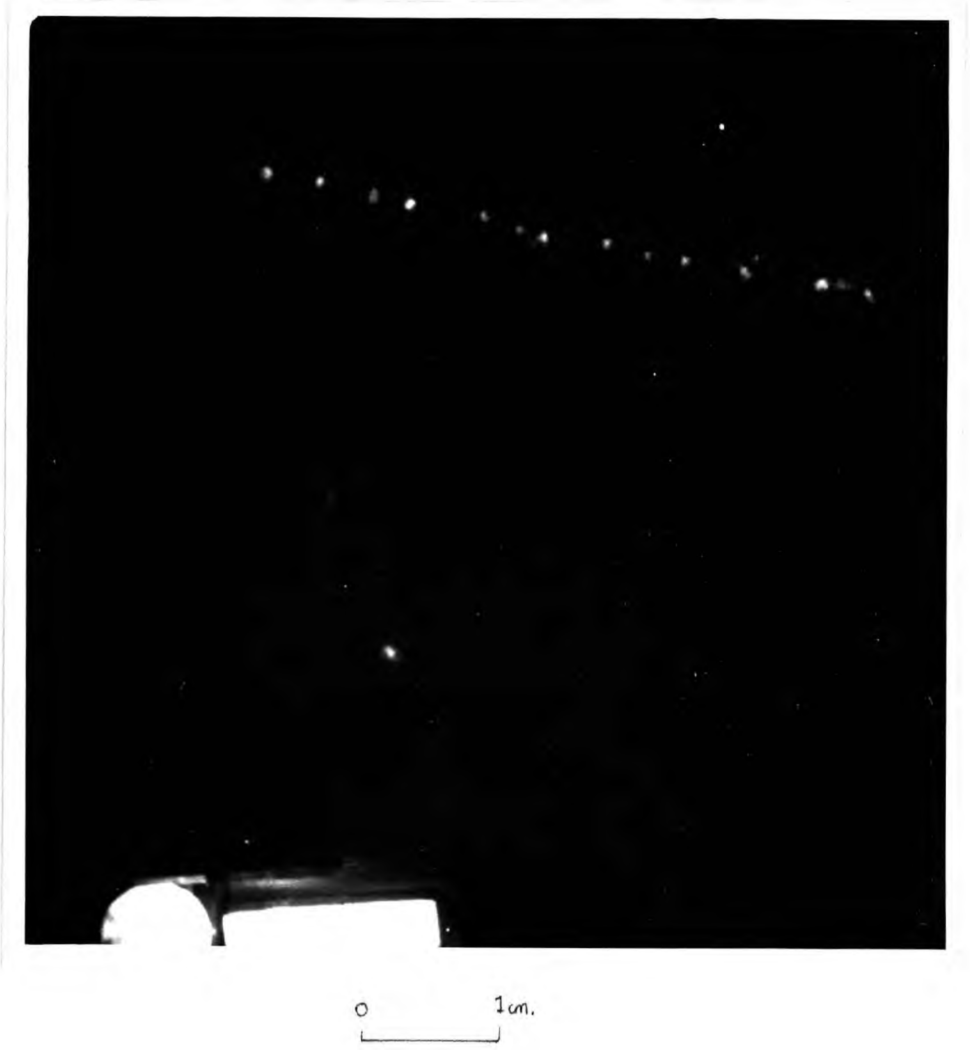

Fig.15. The track of an approximately twice minimum ionizing proton in a CsI(Tl) crystal at ~4:1 demagnification. The first image tube had a photocathode of ~25μA/lumen sensitivity.

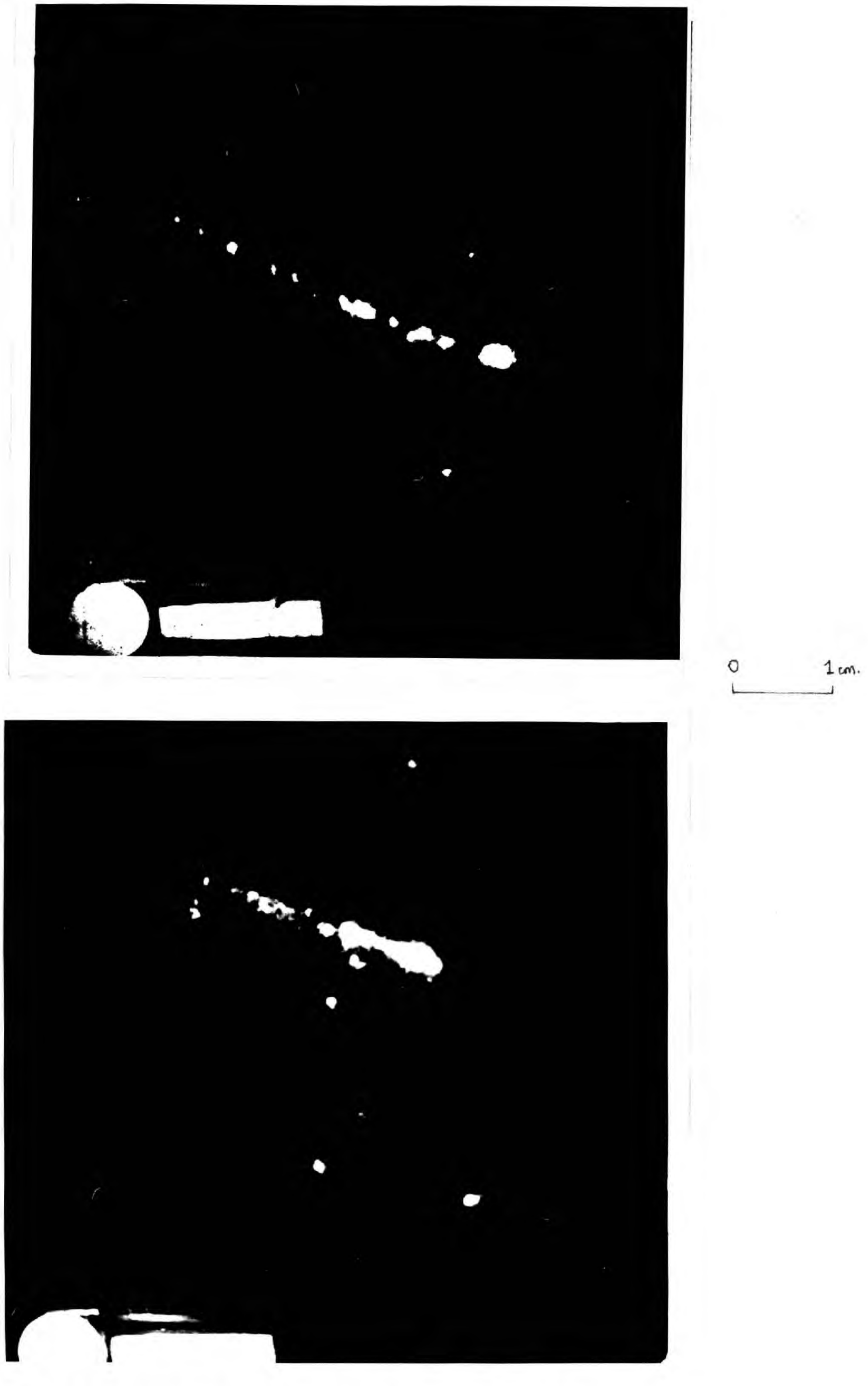

Fig.16. Stopping proton tracks in CsI(Tl) at ~4:1 demagnification. (Photocathode ~ 25μA/lumen.)

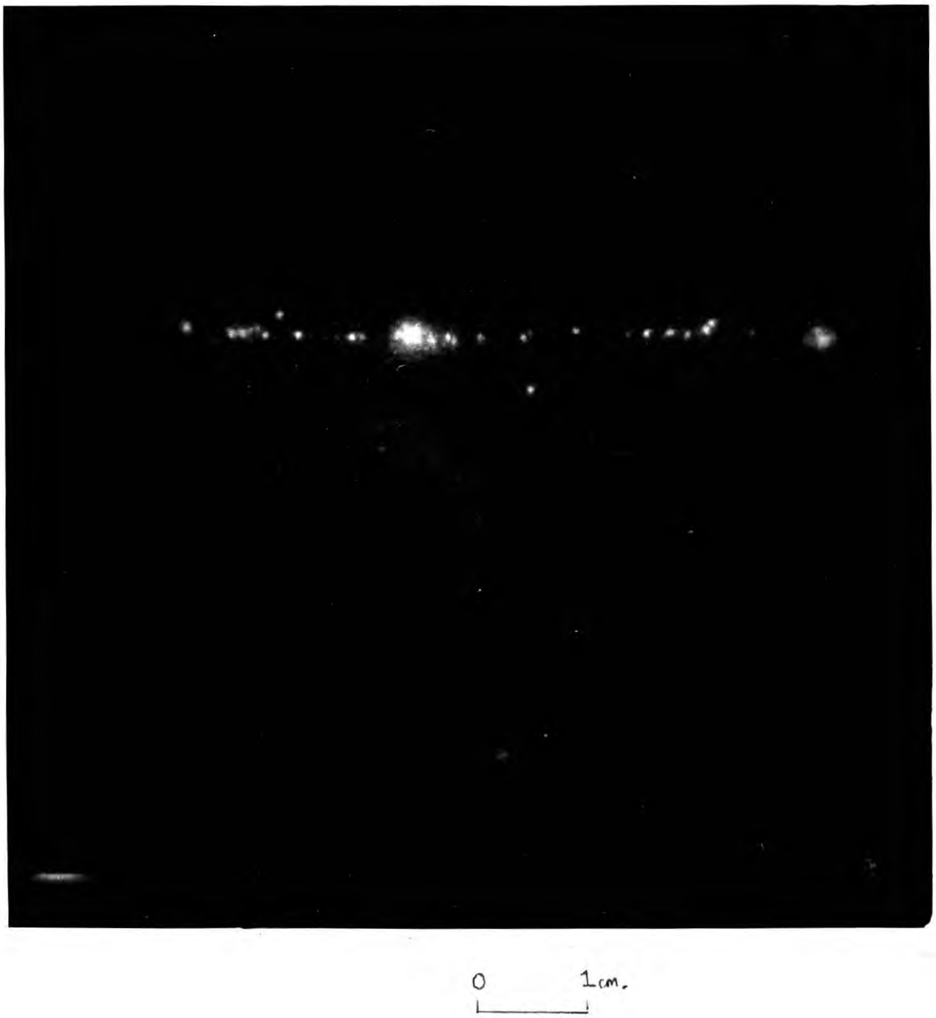

Fig.17. A minimum ionizing proton track in CsI(Tl) at ~4:1 demagnification. Note the very faint background which originates from single photo-electrons at the second photocathode. The first photocathode in this case was a ~100μA/lumen (~13% efficiency at 4400Å) tri-alkali photocathode.

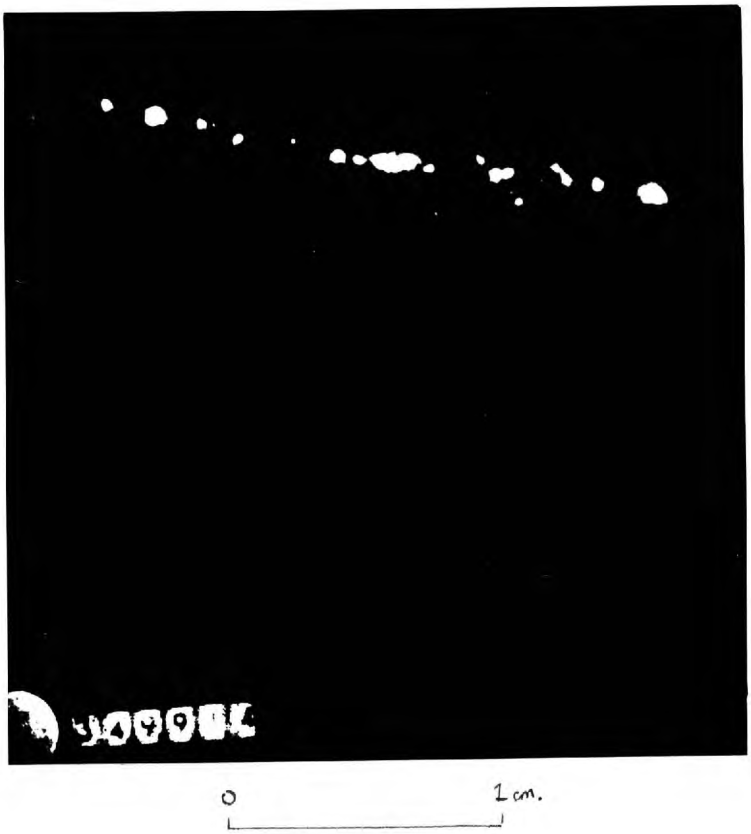

Fig.18. A minimum ionizing proton track in CsI(Tl) at ~1.6:1 demagnification. Note the effect of the smaller depth of field compared with the 4:1 demagnification tracks. (~25μA per lumen photocathode.)

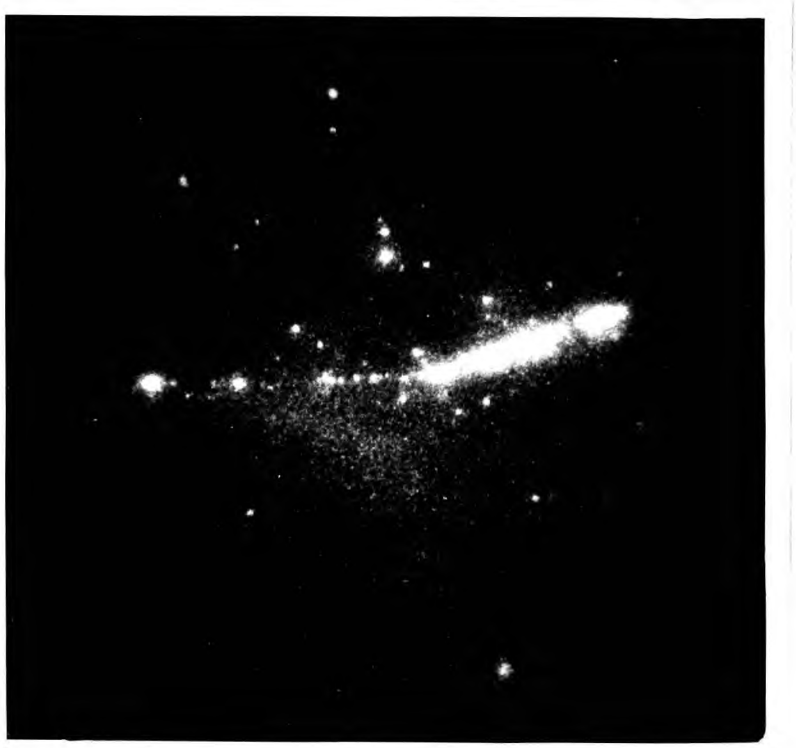

Fig.19(a). $\pi \rightarrow \mu \rightarrow e$ decay in NaI(Tl) at 4:1 demagnification. (~25μA/lumen photocathode.)

Fig.19(b). A minimum ionizing π-meson is slowed down by a scatter in CsI(Tl).

major difficulty during the quantitative scanning of the tracks. In particular, the intensity and size of the scintillation spots were dependent on the overall resolution and gain of the intensifying system. The background or noise visible originates from several sources. In Fig. 17, the small but intense background comes entirely from the trigger tube, and is a function of the operating conditions used for switching this tube. The intense spots are produced from single photo-electrons at the first photocathode whereas the fainter and smaller diameter scintillations are due to single photo-electrons from the second photocathode. These originate (i) externally, from the general unfocussed background light in the inter-intensifier compartment, and (ii) internally from the photocathode to first dynode compartment of the trigger tube. One of the difficulties encountered throughout the scanning of this type of picture was to distinguish between true signal spots and background noise when the statistical fluctuations in gain rendered the two signals comparable in size and brightness on the photographic emulsion.

On other pictures, where there was no visible background from the second photocathode (see Figs. 15, 16, 18, 19) the situation was still frustrated by the terrific range in intensities of the amplified photo-electron spots. These ranged from intense black spots ~ 1mm. in diameter to spots which were just visible. It is reasonable to assume that there were still other clusters of photons originating from signal photo-electrons which were too weak to render the photographic film developable so that the wide fluctuations in gain associated with many stages of transmission secondary emission amplification results in some loss in recording efficiency. The statistical nature of the amplification means that for any particular mean gain associated with the intensifying system, it is meaningful to talk in terms of the probability that any particular photo-electron will be given an amplification which is equal to or greater than the minimum necessary to give a visible spot on the film. If the number distribution of the secondary electrons were known, it would be possible to predict the gain needed to ensure that a certain fraction (for example, 95%) was an average recorded. Research is being carried out to establish the statistics of the multiplication process, since at present the exact nature of the transmission secondary emission mechanism is not understood.

5.4 Scanning Methods

The first step in the analysis adopted for correlating the number of spots obtained on the film with ionization energy loss was to draw out and define zones within which tracks would be accepted for spot counting. For each experimental run, weakly illuminated calibration charts were photographed through the intensifier system at the beginning and end of the run. These charts were centred on the chamber positions so that the exact region of the chamber which was used was always recorded on the film. Throughout the scanning, a projected image of the tracks, magnified by a factor of 10 was used. The relative chamber positions were marked out on the screen together with the position of the camera message-register which served as a fiducial mark for aligning each frame accurately with respect to the chamber position. The chamber area was divided up into 4 or 5 radial regions which corresponded to areas of approximately equal vignetting. The vignetting curves were approximated by a series of step functions. A further restriction ensured that the particle tracks used passed near or through the centre of the chamber within well defined limits so that the track length varied only slightly for all accepted tracks. This restriction was also necessary in order to be able to apply the vignetting correction, as will be described later. As a preliminary experiment, the mean direction of the particle trajectories was established for each intensifier combination by tracing out and measuring the relative angles of many tracks. This procedure was necessary because different combinations of intensifiers produced a net rotation of the image due to electron-optical distortion.

The scanning technique was then straightforward. For each acceptable track (i.e. one which crossed the central region of the chamber within the defined zones, without scattering or interacting), the number of points falling in each zone was recorded, together with the track length and the number of background spots. In most pictures there was no difficulty in deciding whether a scintillation spot was part of a particle track or whether it should be classified as background, but for the doubtful cases the following criterion was adopted. For each demagnification the maximum spread in the incident photon signal due to the depth of focus effect in the chamber was calculated, and a perspex sheet was marked off by two parallel lines whose separation was the corresponding disc of confusion diameter at the photocathode: the parallel lines were then fitted to the track. If the spot lay on or between the two lines, the spot was accepted as a signal spot; otherwise it was classified as background. The greatest difficulty encountered in scanning arose from the wide range in intensities of the tracks. Sometimes it was difficult or impossible to decide the exact number of spots in the vicinity of very intense spots. It is also certain that many very weak but just visible spots must have been missed during the scanning, even when the greatest care was excercised. In a test in which two scanners (who had previously decided on a common scanning criterion) compared their results for the same set of 150 pictures, a 5% difference in the number of spots per cm. was obtained, compared with the 2% r.m.s error of the arithmetic mean in this case. This agreement is surprisingly good when the rather subjective nature of the judgements to be made is borne in mind.

All the results presented in this thesis (except the Čerenkov ring scanning in Chapter 6) are based on scanning carried out by the author only. The above and several other comparative tests of scanning efficiencies, however, indicate that the numbers are quite reproducible if strict scanning criteria are fixed beforehand.

5.5 Treatment of Results.

To get a figure for the number of spots per unit distance and per unit energy loss from the tabulated scanning results obtained as outlined in the last section, the first step was to normalize all the concentric step zones into which the chamber had been divided for zero-angle vignetting over the whole area. This was done by multiplying the number of spots in each zone by a factor which had been computed from the vignetting curves for each lens combination. Although for any particular track an unreal figure is obtained in which fractional numbers of total spots are obtained, an accurate figure for the mean number of spots per unit length (with zero-vignetting) could be calculated when the results for a large number of individual tracks were combined. A sufficient number of tracks of any one kind were scanned to ensure that the statistical or random error of the computed result was always much less than other residual errors, such as non-uniform development of the film and variation in image intensifier gain and resolution. In Fig. 20 a typical histogram of the frequency of track densities is plotted, and a Poisson distribution based on

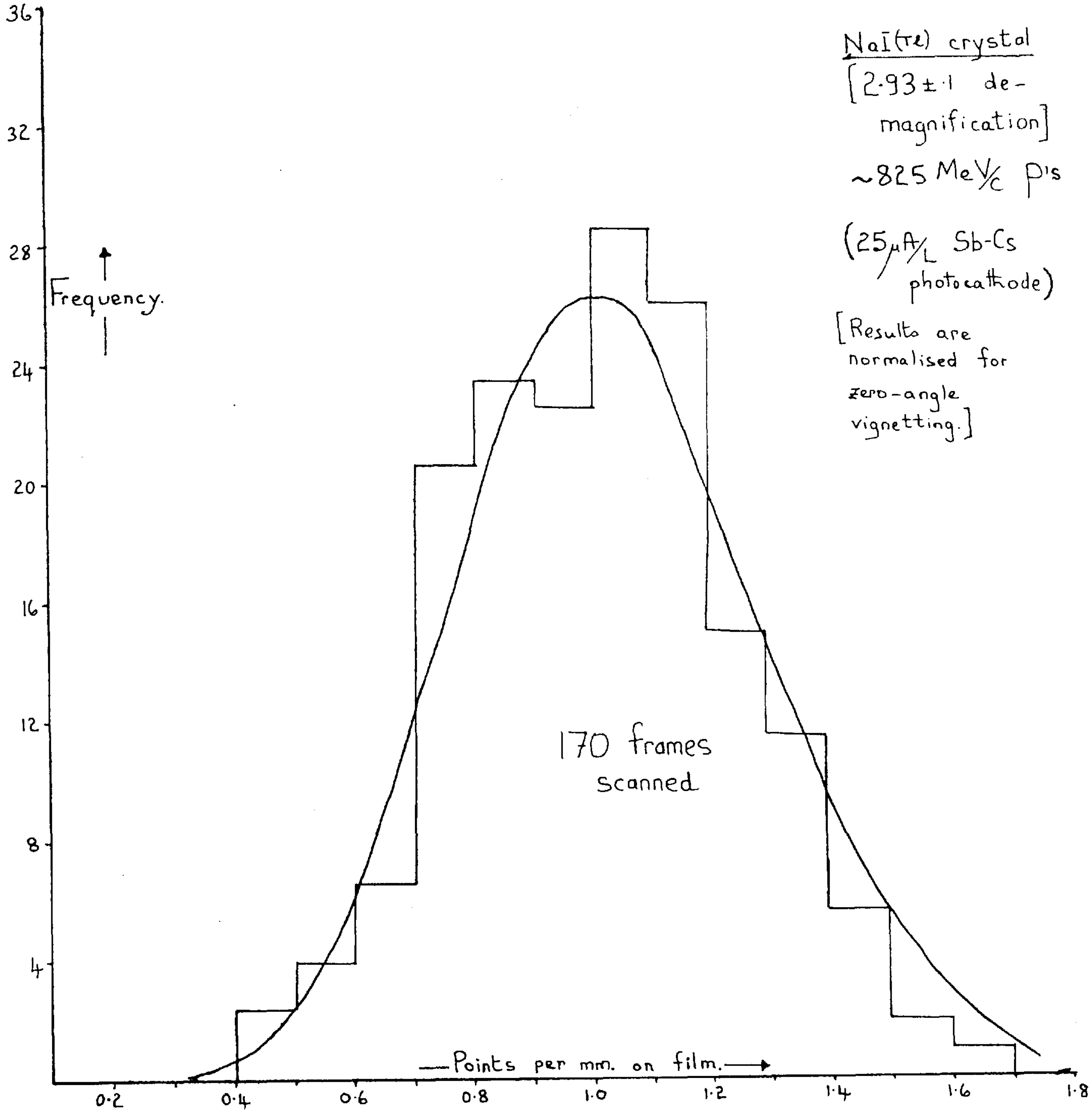

Fig. 20.

Typical Scintillation Chamber Scanning Histogram.

the computed mean is superposed. The Poisson is drawn to indicate an approximate fit to random fluctuations in the various processes involved in forming the spots.

From the nuclear physics viewpoint, it is interesting to know the number of recorded spots per MeV of energy loss in the chamber, and also the number of spots per unit distance in chamber space corresponding to some well defined ionization loss. In these calculations, two important errors arose; first, the momentum spread of the beam meant that the initial ionizing power of the particles was spread out, and secondly the amount of absorber (the scintillation counters and the unused parts of the scintillation chambers) which the particles passed through varied even when the acceptance zone was narrowed down to the central region. The combined effect of these two errors gave a percentage error of up to 25% and was the dominant error in the final figure for points per MeV.

The scanning results are summarised in Table E.

5.6 Analysis of the Results.

It is shown in Appendix A that a particle which produces $P(\lambda)d\lambda$ photons per cm. of track in a chamber gives approximately $\frac{\int P(\lambda)T(\lambda)d\lambda}{16A^2m^2\ n^2}$ photons at the photocathode, where $T(\lambda)$ is the transmission of the lens, 'm' is the demagnification produced by the lens, 'n' is the refractive index of the chamber

TABLE 'E'

Type of photo-cathode	Chamber material.	Type of event.	Demagnification.		Points per mm. on film. *	Points per cm. in chamber	Points per mean track.	Mean energy loss (MeV) †	Points per MeV.
			Front lens	Overall.					
Antimony Cæsium 25 μA/L	NaI(Tl)	min. ion. p.	1·58 ± ·03	1·42 ± ·04	1·75 ± ·06	12·3 ± 0·5	28·2 ± 1·2	19 ± 2·5	1·48 ± 0·2
		2× min. ion. p	3·88 ± 0·1	3·44 ± ·06	1·20 ± ·03	3·5 ± 0·1	19·7 ± 0·6	85 ± 13	0·23 ± ·04
		min. ion. p	2·93 ± 0·1	2·64 ± 0·1	1·00 ± ·03	3·8 ± 0·2	16·6 ± 0·6	33 ± 8	0·5 ± 0·12
	CsI(Tl)	min. ion. p	1·58 ± ·03	1·42 ± ·04	1·74 ± ·03	12·2 ± 0·4	28·8 ± 0·09	25 ± 3	1·15 ± 0·14
		2× min. ion. p	3·88 ± 0·1	3·44 ± ·06	1·03 ± ·02	3·0 ± ·08	16·8 ± 0·5	100 ± 20	0·165 ± ·03
		min. ion. p	2·93 ± 0·1	2·64 ± 0·1	0·88 ± ·025	3·33 ± 0·16	14·5 ± 0·5	44 ± 10	0·33 ± ·08
	NE102 plastic.	2× min. ion. p	1·58 ± ·03	1·42 ± ·04	0·57 ± ·04	4·0 ± 0·3	9·2 ± 0·7	14 ± 4	0·66 ± 0·19
		2× min. ion. p	3·88 ± 0·1	3·44 ± ·06	0·30 ± ·02	0·86 ± 0·06	4·8 ± 0·3	36 ± 6	0·14 ± ·025
	GS/1 glass.	2× min. ion. p	1·58 ± ·03	1·42 ± ·04	0·32 ± ·02	2·3 ± 0·16	5·15 ± 0·35	29 ± 6	0·18 ± 0·04
tri-alkali 100 μA/L	NaI(Tl)	2× min. ion. p	4·44 ± 0·1	4·00 ± 0·1	1·47 ± ·08	3·68 ± 0·22	24·5 ± 0·15	96 ± 10	0·255 ± ·03
	NE102.	2× min. ion. p	1·77 ± ·03	1·59 ± ·03	1·12 ± ·02	7·05 ± 0·18	18·5 ± 0·06	15 ± 4	1·23 ± 0·33
	glass.	2× min. ion. p	1·77 ± ·03	1·59 ± ·03	0·50 ± ·03	3·14 ± 0·2	8·4 ± 0·5	26 ± 6	0·32 ± 0·07

* The errors shown in this column are the R.M.S error of the arithmetic mean. The values are normalised for zero angle vignetting.

† The errors here represent the maximum variation in energy loss due to the combined effects of the momentum spread of the beam particles and the variable absorption path of the scanned tracks.

material, and A is the ratio of image distance to lens aperture. The use of v/d rather than the more usual f/number is reasonable since the limitation to the optical system is set by the angle ϕ in Fig. 31. The expression is accurate only when the object angle is small, but the error involved in using this simpler formula is less than 6% for demagnification greater than 2 for the apertures used in the Saclay experiment. A table giving the accuracies of several approximate formulae for a typical lens aperture is also given in Appendix A.

The number of photo-electrons produced is obtained by including the spectral response of the photocathode $S(\lambda)$ in the integrand. Finally, to obtain the number of recorded spots for each cm. of track in the chamber, the probability 'η' that a single photo-electron be recorded must be included. The number of spots is then given by:-

$$N = \frac{\eta \int P(\lambda)\ T(\lambda)\ S(\lambda)\ d\lambda}{16A^2\ m^2 n^2} \quad \text{..........eq.(5.1)}$$

where the integral is taken over the whole spectrum of the scintillation light.

In principle, this expression can be used to measure 'η' by equating the number of spots per cm. observed experimentally with the theoretically predicted number as given by the right-hand side of eq. (5.1). The absolute value of $P(\lambda)$ was not measured for any of the scintillation chambers used, and the only measure of the efficiency of the photocathode was a figure in terms of microamps per lumen. Because of this, numerical integration of the curves $P(\lambda)$, $T(\lambda)$ and $S(\lambda)$ was not carried out. The scintillator whose efficiency was likely to correspond closest to the quoted efficiency was plastic scintillator, and a value for $P(\lambda)d\lambda$ for plastic based on the quoted 3% absolute scintillation efficiency was used to estimate 'η'. Values of $T(\lambda)$ and $S(\lambda)$ corresponding to the spectral peak (4200Å) of the scintillation light from plastic were used.

All the estimates for 'η' based on the results of Table E and using the above approximations lie between 0.2 and 0.4. A more satisfactory estimate based on Čerenkov light is described in the next chapter.

Apart from the recording efficiency calculations, a number of comparisons (which are independent of $P(\lambda)$ and 'η') can be made to check the validity of eq. (5.1). For any particular crystal, used at different demagnifications, the recorded number of spots is given by:-

$$N_a = \frac{\eta\int P(\lambda)\, T_a(\lambda)\, S(\lambda)\, d\lambda}{16\, A_a^2\, n^2\, M_a^2} \quad \text{.........eq.(5.2)}$$

and

$$N_b = \frac{\eta\int P(\lambda)\, T_b(\lambda)\, S(\lambda)\, d\lambda}{16\, A_b^2\, n^2\, M_b^2} \quad \text{.........eq.(5.3)}$$

where the subscripts 'a' and 'b' refer to two different demagnifications.

Dividing eq.(5.2) by eq.(5.3), we get:-

$$\frac{N_a}{N_b} = \frac{\int P(\lambda)T_a(\lambda)S(\lambda)d\lambda}{\int P(\lambda)T_b(\lambda)S(\lambda)d\lambda} \times \frac{A_b^2\ M_b^2}{A_a^2\ M_a^2} \quad \text{.......eq.(5.4)}$$

and if the transmission curves for the lenses which give the two demagnifications are taken to be approximately equal, and the recording efficiency 'η' remains constant then

$$\frac{N_a}{N_b} = \frac{A_b^2\ M_b^2}{A_a^2\ M_a^2} \quad \text{..................eq.(5.5)}$$

All the results of Table E are consistent with the ratios calculated from eq.(5.5), within the limits of the experimental errors.

If the absolute scintillation efficiency of the plastic scintillator used is taken to be 3% then rough estimates for the scintillation efficiencies of the other three chamber materials can be made. In working out these efficiencies, the approximation is made that the spectral outputs are similar; this is reasonable within the accuracy of the estimates. The values obtained were:-

(8 ± 2.5) % for NaI(tℓ)

(4 ± 1) % for CsI(tℓ)

(1 ± 0.3) % for Glass scintillator type GS/1

Or, in terms of photons for a minimum ionizing excitation:

130,000 ± 43,000 per cm. for NaI(tℓ)

90,000 ± 23,000 per cm. for CsI(tℓ)

12,000 ± 4,000 per cm. for glass scintillator, type GS/1

Finally, it is possible to judge the relative performance of the two types of photocathode used in the experiments. By comparing the ratios of recorded spots per MeV for the results obtained with the two photocathodes, an improvement factor ~ 2 in the overall recording efficiency is found when using the 100 microamps per lumen tri-alkali photocathode, compared with the 25 microamps per lumen antimony -caesium photocathode.

5.7 Summary of properties and Capabilities of Scintillation Chambers.

The results described in the previous two sections can be generally extrapolated to predict the present performance capabilities in terms of the number of spots per cm. in chamber space that are recorded for any combination of luminescent material, lens, and image tube, with the underlying assumptions that the behaviour of these components are similar to those used in the experiment. Alternatively, by equating the desired number of spots per cm. produced by some standard excitation to the right-hand-side of eq.(5.1), it is possible to arrive at reasonable values which would be needed for the parameters of the system in order to achieve this spot density.

As an example, suppose 5 recorded spots per cm. in chamber space were required for minimum ionizing particles, using plastic scintillator as the scintillation material. Then assuming a 100 microamp per lumen photocathode, 90% transmission of the scintillation light, and 1/3 recording efficiency for photo-electrons, and substituting in eq.(5.1) this requirement is equivalent to

$$Am = 1.5 \quad \ldots\ldots\ldots\ldots\text{eq.}(5.6)$$

If an useable field of 5 cm is needed and the photocathode is 2.5 cm in diameter then m = 2, so that A must be ~ .75. A lens satisfying these conditions would have to be specially designed.

Once the lens aperture and demagnification have been specified, the useful depth of chamber can be worked out; the value depends on what criterion is adopted for the allowed disc of confusion, as given in eq. (A.13) of Appendix A. The choice of useable depth is bound to be tied up with the number of spots per cm. specified in the normal viewing plane of the chamber, and with the particular degree of track recognition or information needed in the experiment.

Examination of the parameters of eq.(5.1) shows that there is little scope for a large improvement on the present overall recording efficiency except from the recording efficiency of the intensifier system. It is instructive to consider the improvement factor on the current performance that would be attained in an 'ideal' detector of this type. The best scintillators at present available yield ~150,000 photons per cm. for minimum ionizing excitation. The lens systems used in the present experiments transmitted between 60 and 70% of the incident scintillation light so that there is a slight improvement to ~90% possible here. The most efficient photocathodes produced nowadays have quantum efficiencies of between 20 and 30% at their most sensitive working wavelength. The aperture of the lens system is always limited to somewhere around the present value if the depth of field is not to be reduced. All the above factors amount to an improvement on the current performance by a factor of 1.5 to 2 at the most. If, however, the recording efficiency of the image intensifier system was ~ 100%, a further improvement by a factor of about 3 could be achieved (evidence in the next chapter indicates that 'η' is most probably ~ 33%). Thus one could hope in an 'ideal' scintillation chamber system to improve on the present overall recording efficiency by a factor of between 4 and 6. This gain in sensitivity could be taken up in different ways depending on the needs of the experiment.

CHAPTER 6

The Čerenkov Ring Experiment

6.1 Principles of Čerenkov Ring Imaging

The Čerenkov light from a particle of charge 'e' travelling with velocity 'βc' in a medium of refractive index 'n' is emitted at an angle $\theta = \cos^{-1}(1/\beta n)$ to the trajectory of the particle. The number of photons emitted per unit path length, per unit wavelength interval is proportional to $1/\lambda^2$; the radiation intensity in terms of the number of photons produced within a spectral region defined by the wavelengths λ_1 and λ_2 is given by:

$$N_{ph} = 2\pi\alpha \ell \int_{\lambda_1}^{\lambda_2} \frac{1}{\lambda^2} \sin^2\theta \times d\lambda \text{ .... eq.(6.1)}$$

where α is the fine structure constant; $\alpha = \frac{e^2}{hc} \approx \frac{1}{137}$

and 'ℓ' is the path length.

The Čerenkov light from a particle may be focussed to a circular ring by a lens whose optic axis coincides with its trajectory, the radius of the ring 'r' being given by the focal length 'f' of the lens and the emission angle of the Čerenkov radiation:-

$$r = f\tan\theta$$

A ring image is also produced, to a first approximation, for a particle whose trajectory does not coincide with the principal axis of the lens; in this case the centre of the ring is displaced by an amount depending on the angle between the particle direction and the principal axis. Thus a measure of the ring diameter enables 'θ', and hence 'β' to be evaluated (n being known). The position of the ring determines the orientation of the trajectory of the particle with respect to the principal axis. The position of the trajectory in space is not, however, determined (it may move parallel to itself without altering the ring position). Location of one point on the trajectory of the particle (e.g. by means of a small scintillation counter), together with the Čerenkov ring position, fixes it in space.

This focussing property of Čerenkov light has been used extensively for measuring particle velocities, using photomultipliers as light detectors.[44] A small range '$\Delta\theta$' is selected by placing an annular opening of mean radius 'r' in the focal plane and viewing the ring with a single photomultiplier, or an array of photomultipliers in more complicated devices. An inherent disadvantage of these differential Čerenkov counters is the small solid angle of acceptance allowed if an accurate velocity determination is to be made, which has confined the use of such counters to particle identification in primary beams.

If the ring is imaged on the photocathode of an image intensifier, the requirement for presetting for a certain range of $\Delta\theta$ in θ is overcome since rings of a whole range of diameters can now be recorded, and the solid angle of acceptance is limited only by the size of the photocathode sensitive area. The idea of using image tubes in this way was first suggested by Roberts in 1960 [45].

Of crucial importance is the question of whether a sufficient number of photons can be recorded on the ring image to make the technique a practical proposition, and it was this aspect of the Čerenkov camera that was investigated at Saclay. The problem of obtaining the highest possible accuracy of velocity measurement was given secondary consideration.

6.2 The light Collection Problem.

In differential form, eq. (6.1) is written;

$$dN_{ph} = 2\pi\alpha \ell \sin^2\theta \; d\lambda / \lambda^2 \quad \text{................eq.(6.2)}$$

If the radius of the lens aperture is 'a', then;

$$\tan\theta = \frac{a}{\ell} = \frac{r}{f}$$

Thus for small angles, where $\sin\theta \simeq \tan\theta$, eq. (6.2) may be written:-

$$dN_{ph} = 2\pi\alpha \frac{a}{f} \; r \; d\lambda / \lambda^2 \quad \text{..........eq.(6.3)}$$

The number of photons reaching the photocathode will depend on the lens transmission, which is a function of wavelength, $T(\lambda)$. The number of photo-electrons emitted will be given by folding the photon spectrum incident on the photocathode with the quantum efficiency, $S(\lambda)$, of the photocathode. The total number of photo-electrons is thus:-

$$N_{pe} = 2\pi\alpha \frac{a}{f} \; r \int_{\lambda_1}^{\lambda_2} \frac{1}{\lambda^2} \, T(\lambda) \, S(\lambda) \, d\lambda \quad \text{....eq.(6.4)}$$

The limits of integration are set by the vanishing of $T(\lambda)$, or $S(\lambda)$, or by the dispersion of the refracting medium (i.e., $\theta = \theta(\lambda)$)

Eq. (6.4) shows that there is little freedom available in choosing the parameters of a system. An upper limit for a/f is that which corresponds to the largest apertures readily available (i.e., f/0.7, so that $\frac{a}{f} \sim 0.7$), whilst 'r' cannot be greater than the radius of the photocathode. The functions $T(\lambda)$ and $S(\lambda)$ are set by lens design and photocathode technology .

In practice, it was found that thelarge aperture lenses available were severely restricted in angular acceptance due to vignetting, and this may be taken into consideration as follows:-

Again, $$dN_{ph} = \frac{2\pi\alpha\sin^2\theta}{\lambda^2}\, d\ell\, d\lambda$$

and using $d\ell = dr/\sin\theta$,

$$dN_{ph} = \frac{2\pi\alpha T(\lambda,r)}{\lambda^2}\sin\theta\, dr\, d\lambda \quad \text{...............eq.(6.5)}$$

Now assume $T(\lambda,r) = T(\lambda)\, t(r)$, then

$$N_{ph} = 2\pi\alpha\sin\theta\int_0^r t(r)dr\int_{\lambda_1}^{\lambda_2}\frac{1}{\lambda^2}T(\lambda)\, d\lambda \quad \text{..........eq.(6.6)}$$

and $$N_{pe} = 2\pi\alpha\sin\theta\int_0^r t(r)dr\int_{\lambda_1}^{\lambda_2}\frac{1}{\lambda^2}T(\lambda)S(\lambda)\, d\lambda \quad \text{......eq.(6.7)}$$

Measurements on the transmission with angle and wavelength confirmed that the transmission could be written in the form $T(\lambda,r) \equiv T(\lambda)t(r)$. At 7°, the effective aperture (i.e. the quantity $\int_0^r t(r)\,dr$) of the 65 mm. f/0.7 Oude Delfte lens was 2.7cm., which meant that its effective f/number was only f/1.2. For larger angles the effective aperture dropped sharply to zero. Because of this effect, similar measurements were carried out on a simple condenser doublet (f/1.42, 5" focal length). In this case, the effective aperture was 4.3 cm. at 5°, giving an effective f/number of f/1.48. The limitation on angle was the photocathode diameter. It should be noted that the amount of Čerenkov radiation falling on an annular ring element of the lens surface is proportional to the difference between the two extreme radii which define the annulus (i.e. to dr) . The condenser doublet proved to have superior transmission characteristics compared with the highly corrected 8-element Oude Delfte lens, but worse resolution. However, since the experiment was not primarily concerned with accurate velocity measurement, the resolution was not an important limiting factor. Numerical evaluation of the integrals in eq.(6.7) gave a predicted 6 points on an 8 mm. radius ring for the Oude Delfte lens (corresponding to a Čerenkov angle of $\sim 7^{\circ}$, which was the largest that could be used with this lens), and 16 points on a 11 mm. radius circle for the Dallmeyer condenser lens (corresponding to a Čerenkov angle of 5°). Both these figures assume a tri-alkali photocathode with response of 100 micro-amps per lumen and general shape as given by standard E.M.I. curves. A transmission loss factor for the exit window of the Čerenkov chamber and for the reflection through 90° by a mirror, as well as the reduction in useful radiation path caused by the 90° reflection was allowed for in the above estimates.

6.3 Perturbing effects on an Ideal Čerenkov Ring.

The recorded images of photons from a single particle do not lie on a perfect circle because of the following effects:

(a) Loss of particle energy in the radiator.

(b) Dispersion of the radiator.

(c) Multiple coulomb scattering of the particle in the radiator.

(d) Limitations of the optical coupling.

(e) Image intensifier resolution, distortion and background noise.

The magnitude of each of these effects in the case of the Saclay experimental run is discussed below.

(a) The radiator thickness traversed by the particle was ~ 100 cm., and the highest refractive index used ($n = 1.025$) required a pressure of 18 atmospheres. For the radiator used, this is equivalent to a radiator density of 8.5 gm./cm^2. The energy loss for 700 MeV/C π-mesons is ~ 14 MeV giving a change of 0.0016 in β, corresponding to a change of $\sim 1^\circ$ in θ if everything else were constant. Using the Dallmeyer 5" lens this results in a gradual reduction by about 1 mm. in the radius of the ring; the photons originating at the beginning of the particle trajectory lie on the largest ring diameter, those produced at the end give the other limiting diameter.

(b) Dispersion effects.

Figures for the dispersion in gases of use in Čerenkov cameras are not readily available, but it is reasonable to take as a representative value for gas dispersion $\frac{d\Gamma}{\Gamma} \approx 0.03$, where $\Gamma = n - 1$.[46] Differentiating the Čerenkov relation $\cos\theta = (1/\beta n)$ for constant β gives the angular resolution in terms of refractive index;

$$\left(\frac{d\,\theta}{\mathrm{cotan}\,\theta}\right)_\beta = \left(\frac{dn}{n}\right)_\beta \quad \ldots\ldots\ldots\ldots\ldots \text{eq.}(6.8)$$

or $$\left(\frac{d\theta}{\mathrm{cotan}\theta}\right)_\beta = \left(\frac{d\Gamma}{1+\Gamma}\right)_\beta$$

$$= \left(\frac{d\Gamma}{\Gamma}\right)_\beta \left(\frac{\Gamma}{1+\Gamma}\right)_\beta$$

Now $\Gamma \ll 1$, so that

$$\left(\frac{d\theta}{\mathrm{cotan}\theta}\right)_\beta \approx \left(\frac{d\Gamma}{\Gamma}\right)_\beta \times \Gamma$$

$$\left(\frac{d\theta}{\mathrm{cotan}\theta}\right)_\beta \approx \pm\, 0.015\,\Gamma \quad \ldots\ldots\ldots\ldots \text{eq.}(6.9)$$

For the rings photographed in the experiment, Γ was typically 0.02 and $\theta \sim 5^\circ$, whence $d\theta \approx \pm\, 3 \times 10^{-5}$ radians. This gave a spread of $\pm\, 4 \times 10^{-1}$ mm. on the photocathode, which was of same order as ~~quite negligible compared with~~ the other factors contributing to the spread in θ.

(c) Multiple coulomb scattering and diffraction. Dedrick[47] has calculated the angular spread of the Čerenkov radiation emitted by a particle undergoing multiple scattering. He has taken the diffraction effects produced by the loss of coherence into account, but the slowing-down effects due to energy loss are not allowed for. The half-width of the emitted light at half-intensity is about one-half of the mean scattering angle of the particle. For 'arcton 13' at 18 atmospheres the R.M.S scattering angle for pions of energy to give 16 mm. diameter rings was ± 1°. The corresponding value for $\Delta\theta$, using Dedrick's curves was ± ½°, giving a spread of ± 1mm in 'r' for the 5" Dallmeyer lens.

(d) Limitations of the optical coupling lens.

The Dallmeyer 5" f/1.42 lens was certainly very badly corrected for the usual aberrations, but it was verified that the imperfections introduced due to the lens would not degrade the rings when the other perturbing effects (notably scattering) were borne in mind.

(e) A single transmission secondary emission tube gives typically a resolution of 15 to 20 ℓp./mm. With two such tubes in cascade, however, the resolution achieved at Saclay was in the 2 to 5 ℓp./mm. range. The dominant distortion in electrostatic-magnetic focussed tubes is the S-shaped distortion of radial lines. Although such a distortion produces only second order effects on a ring image, it would have to be allowed for by calibration in any accurate measurement of velocity.

The presence of noise spots, not associated with the Čerenkov light from the particle under investigation, would also interfere with an estimate of the ring diameter, since these would be indistinguishable from the 'genuine' signal photons. Such noise spots could arise internally in the intensifier system, or could be due to photo-electrons produced by unfocussed Čerenkov light given off by the passage of spurious particles through transparent components at the front end of the Čerenkov camera (lenses, glass window, image tube end-window etc.). The time resolution of the system was such that the chance of internal thermal photo-electrons coincident with the signal was of the order of 0.002 photoelectrons per picture. External noise was eliminated as much as possible by shielding; the residual noise was allowed for by special calibration runs described in the next section.

From the above discussion it is apparent that scattering, energy loss and lens resolution introduced approximately equal contributions to the spread in the radius of a ring due to a particle in the low momentum π-beam used at Saclay. It must be mentioned that the momentum spread of 3% in the primary beam of 736 MeV/c (corresponding to 16 mm. diameter rings for a refractive index of 1.02) gave rise to variations in diameter from 11 to 20 mm in the Čerenkov ring pictures. Because of this large variation in the intrinsic radius of the rings, together with the simultaneous effects of the other perturbations described it was difficult to decide on the diameter of many of the rings having a small number of points. Moreover, it is clear that the experiments provided no test of the ultimate precision in velocity determination of the apparatus.

6.4 The apparatus used.

It has been shown in section 6.2 that the parameters of a Čerenkov ring imaging system are strictly defined by the lens and image intensifier dimensions. Using the Dallmeyer condenser lens for imaging the light, the maximum acceptable angle for Čerenkov light was 5°. The tests were to be carried out with electrons ($\beta \approx 1$), and with 700 MeV/c π - mesons ($\beta \sim 0.98$), so that for values of θ from 0 to 5°, a refractive index variation from 1.0 to 1.025 was required.

The Čerenkov camera was designed by Mr. M. R. Jane. Fig. 21 is a schematic diagram of the camera and coupling lens system. Čerenkov light was produced when the beam particles crossed a cylindrical duralumin chamber 9 cm. in diameter and 85 cm. effective length containing "arcton 13" ($CC\ell F_3$) gas. This gas gave a refractive index range from 1.004 to 1.025 for a pressure range from 60 to 300 lbs./sq. inch. at $15^{\circ}C$. The pressure was monitored using a Bourdon-type gauge accurate to 0.5 lb./sq. inch over the full scale range (20 to 300 lb./sq. inch). To keep the intensifier system out of the particle beam, the Čerenkov radiation was reflected through 90° by the mirror, M, and emerged from the chamber through a pressurized glass window. The chamber assembly was pressure-tested to a pressure of 600 lb./sq.inch. Great care

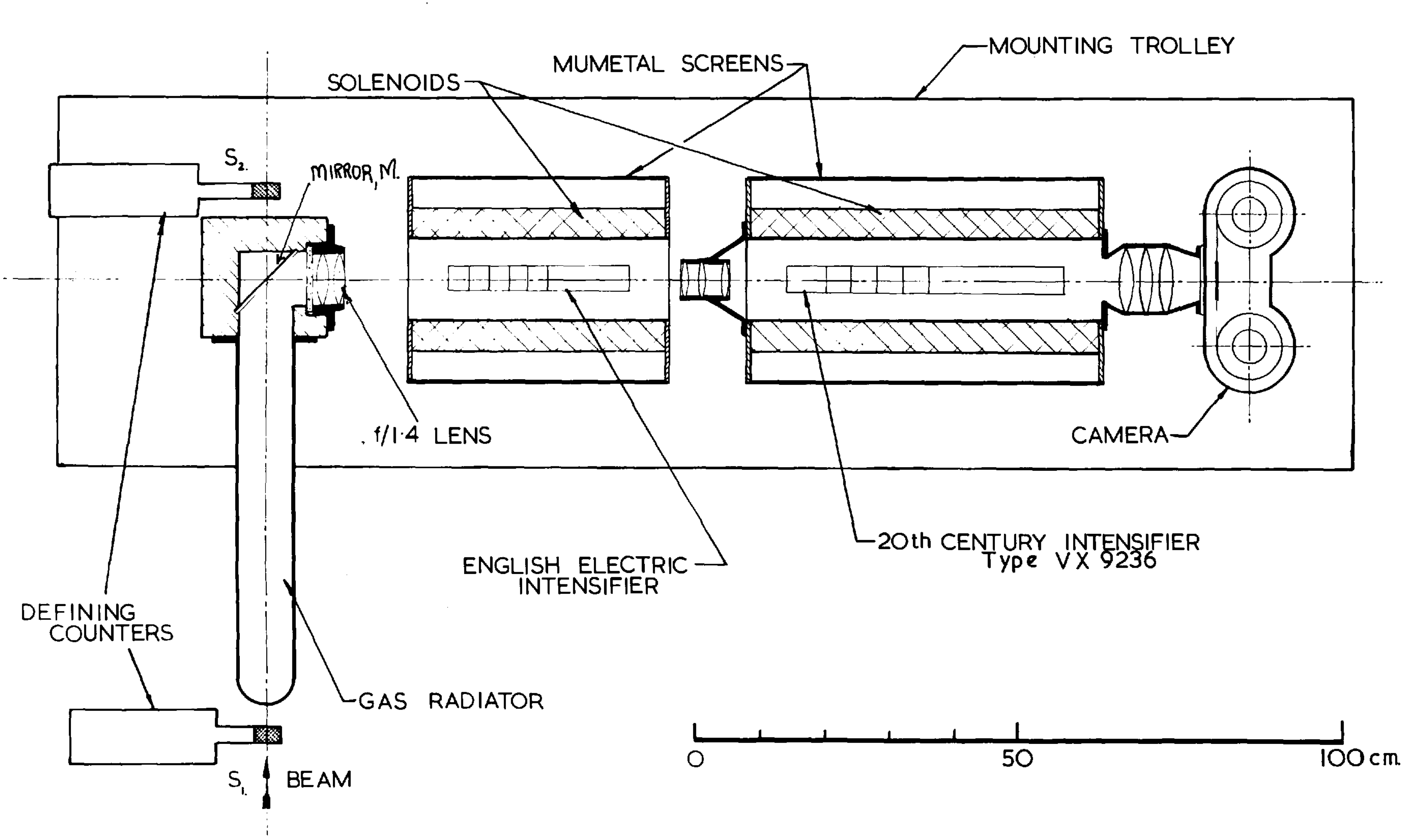

Fig. 21. PLAN OF ČERENKOV CAMERA

was taken in light-tighting the Čerenkov camera connection onto the image intensifier housing, a thin flexible rubber membrane being used as the light-tight material.

6.5 Scanning Methods.

Representative examples of the 'ring' image of photoelectrons produced by Čerenkov radiation under different conditions are shown in Fig. 22(a),(b),(c) and (d). The Čerenkov angle ranges from 2.2° to 4.5° (10mm. to 20mm. diameter on the photocathode), covering a momentum range of 45 MeV/c around 700 MeV/c. These rings have been selected to have more spots than 'average' rings would have so that the circular pattern formed by them is more clearly visible.

To make a quantitative analysis of the number of photoelectrons observed in the runs, an estimate of the ring diameter is required. Since the diameter is a very sensitive function of both momentum and refractive index, it was not possible to compute a reliable figure from the magnet current and chamber pressure and temperature readings. At a constant temperature and pressure corresponding to a refractive index of 1.02, the Čerenkov angle for π-mesons varies from threshold at 695 MeV/c to the maximum angle for which the rings still fall on the photocathode ($5^{\circ}30'$) at 790 MeV/c. A computation for 16 mm. diameter rings to within ± 0.5 mm. on the photocathode would require a knowledge of the momentum to 8 MeV/c (i.e. 1% accuracy), together with temperature

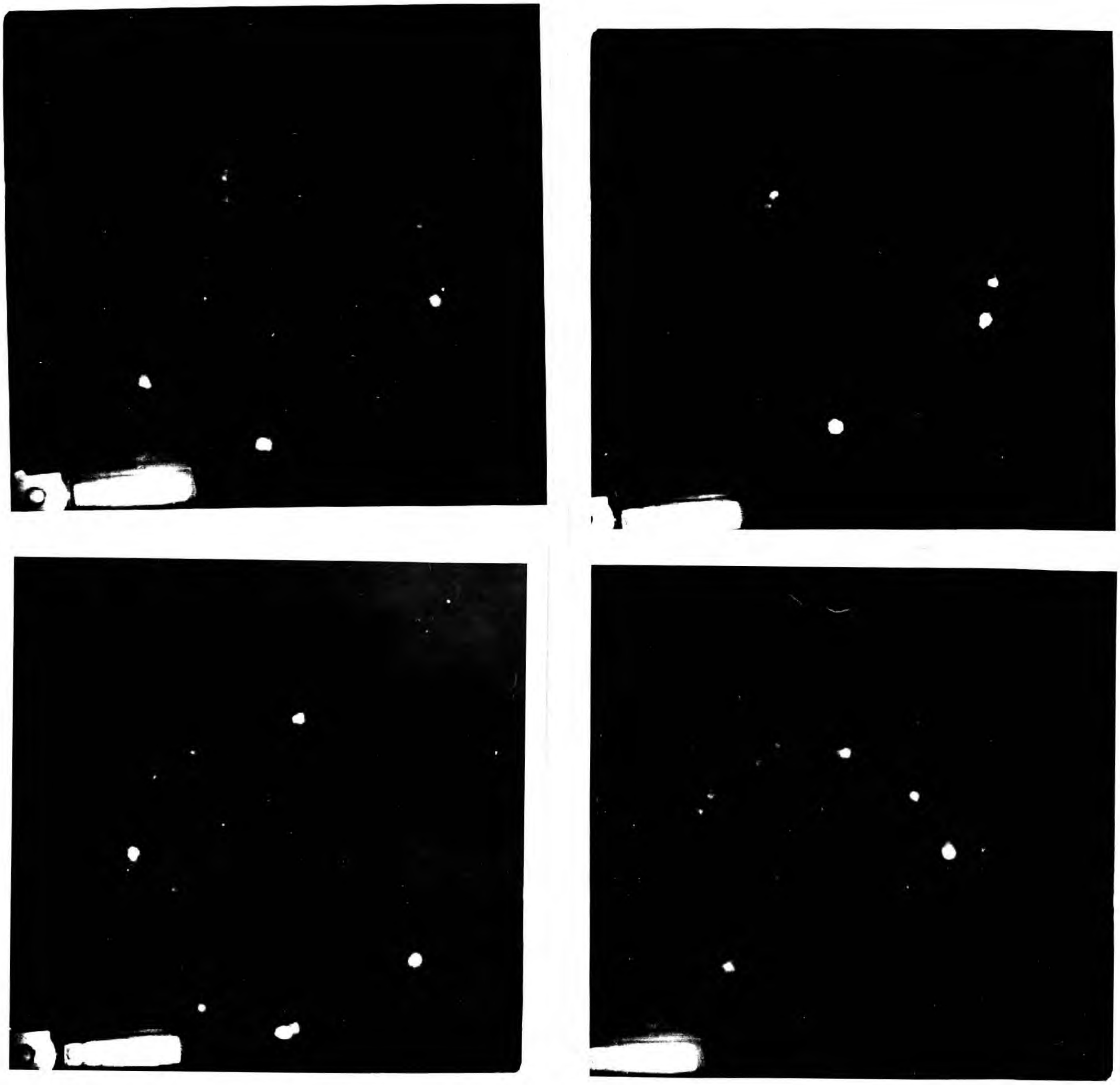

Fig.22. Pictures of Čerenkov rings produced by single pions. The Čerenkov angle varies from 2.2° to 4.5° (10mm. to 20mm. diameter on the photocathode), covering a momentum range of $\sim$ 45Mev/c around 700Mev/c.

monitoring to 1°C. Neither of these requirements were met in the experimental system; the actual momentum accuracy was between 3 and 5%, and no accurate check was kept on the chamber temperature. The procedure adopted was therefore to set the momentum and pressure at reasonable values, and observe the rings visually on integrated pictures; in this way it was possible to make slight adjustments to the pressure of the radiating gas to give rings of roughly the desired diameter.

The demagnification factor of the image intensifying system from first photocathode to photographic film was accurately known so that by measuring a number of rings having a large number of spots, a good value for the mean diameter on the photocathode would be obtained (i.e. to within 1 mm). By using this figure, together with the relevant temperature and pressure readings, a figure for the corresponding mean momentum could be worked out, the accuracy of which was limited entirely by the refractive index accuracy. This gave a check on the momentum-current relationship and was used as a standard reference point.

Only negatively charged particles were used to produce Čerenkov rings, most of the pictures being taken for π^--mesons, and a few for electrons. At a refractive index of 1.02 and momentum 736 MeV/c (corresponding to a ring diameter of 16 mm. for π^--mesons), the diameters for μ^--mesons and electrons are 35 mm. and 50 mm. respectively so that there was no danger of confusion between the particles at these low momenta.

Several criteria for scanning the Čerenkov rings were adopted:-

(i) Simple spot counting. Here the total number of spots visible in each frame was noted with no restriction. Although this method gave a crude estimate of the mean spot diameter, a number of serious biases were introduced. There was no method of discriminating between signal and noise, and no check that the spots came from rings which were properly centred on the photocathode. Also, the counter system selected all negative particles whereas only π^--mesons could give rings which could be imaged on the photocathode.

(ii) Scan for spots which lie in a circular diaphragm whose mean diameter corresponded to the approximate mean ring diameter, and whose width allowed a reasonable spread due to the perturbations on an ideal ring. This was an improvement on method (i), but was still very indefinite for rings having a small number of spots (i.e. less than four). It also ignored the fact that some rings fell partially off the sensitive area of the photocathode, and this tended to give a pessimistic figure for the mean number of spots. Scans were made for diaphragms of different width.

(iii) Diaphragm scanning as in (ii) but with the additional requirement that the ring must fall completely on the photocathode.

This method of scanning, if it could be applied fairly, should have given the best set of values for the number of spots on a ring, but in practice it was difficult to apply. It was often possible to fit the diaphragm onto the spots so that the ring was entirely in the sensitive area, or by choosing a different but apparently equally allowable position, the ring could be made to fall off the sensitive area. The scanning criterion adopted was that if a ring could be made to partially fall off the photocathode, it was rejected.

In order to get around the difficulty (present in all three scanning methods), of not knowing whether a blank frame represented a Čerenkov ring in which the statistics of producing and amplifying the photo-electrons had produced no recordable scintillation spots, or whether it represented a μ^- or electron going through the counters, a method of estimating the mean number of spots was devised, based on the assumption that the final distribution was Poissonian. The probability of 'r' events occuring in a certain time is:-

$$N(r) = \frac{N_{tot} \; Z^r \, e^{-Z}}{\lfloor\underline{r}}$$

Where Z is the mean number in this time. A graph of $\left[\log_e N(r) + \log_e \lfloor\underline{r}\right]$ against 'r' is a straight line of slope $\log_e Z$ and intercept $\log_e N_{tot}$. Only frames having 3 or more spots were used in computing the mean so that stray background

Čerenkov light which could give rise to one or occasionally two spots was also eliminated. An estimate of the background was made by recording the number of points that did not fall within the diaphragm in scanning method (ii) as well as those that did; this number was classified as background. The number of spots not associated with π-meson rings was found to be 0.3 per frame. Most of this light must come from scattered Čerenkov light since the thermal background contribution was always very small.

All the scanning described in this chapter was carried out by Mr. M. R. Jane, to whom the author is greatly indebted for permission to publish the results.

6.6 Results.

Fig. 23(a) is a typical histogram of frequency against number of points on a ring when method (ii) was applied to 16 mm. rings produced by π^--mesons, and Fig. 23(b) is a plot of $\left[\log_e \underline{|r} + \log_e N(r)\right]$ against 'r' to determine the mean. The best value based on this method was 3.8. A Poisson based on the mean estimated from the method of Fig.23(b) is superimposed on the histogram for comparison. The same pictures, when scanned by method (iii) gave an estimated mean of 4.7, and Figs. 24(a) and (b) show the relevant histogram and straight line plot. This method of scanning clearly introduces a bias against rings having a small number of points because it was easier to find a position where the ring could fall off thephotocathode area in these cases. This is indicated by the low ordinates of the histogram columns for rings having 5 spots

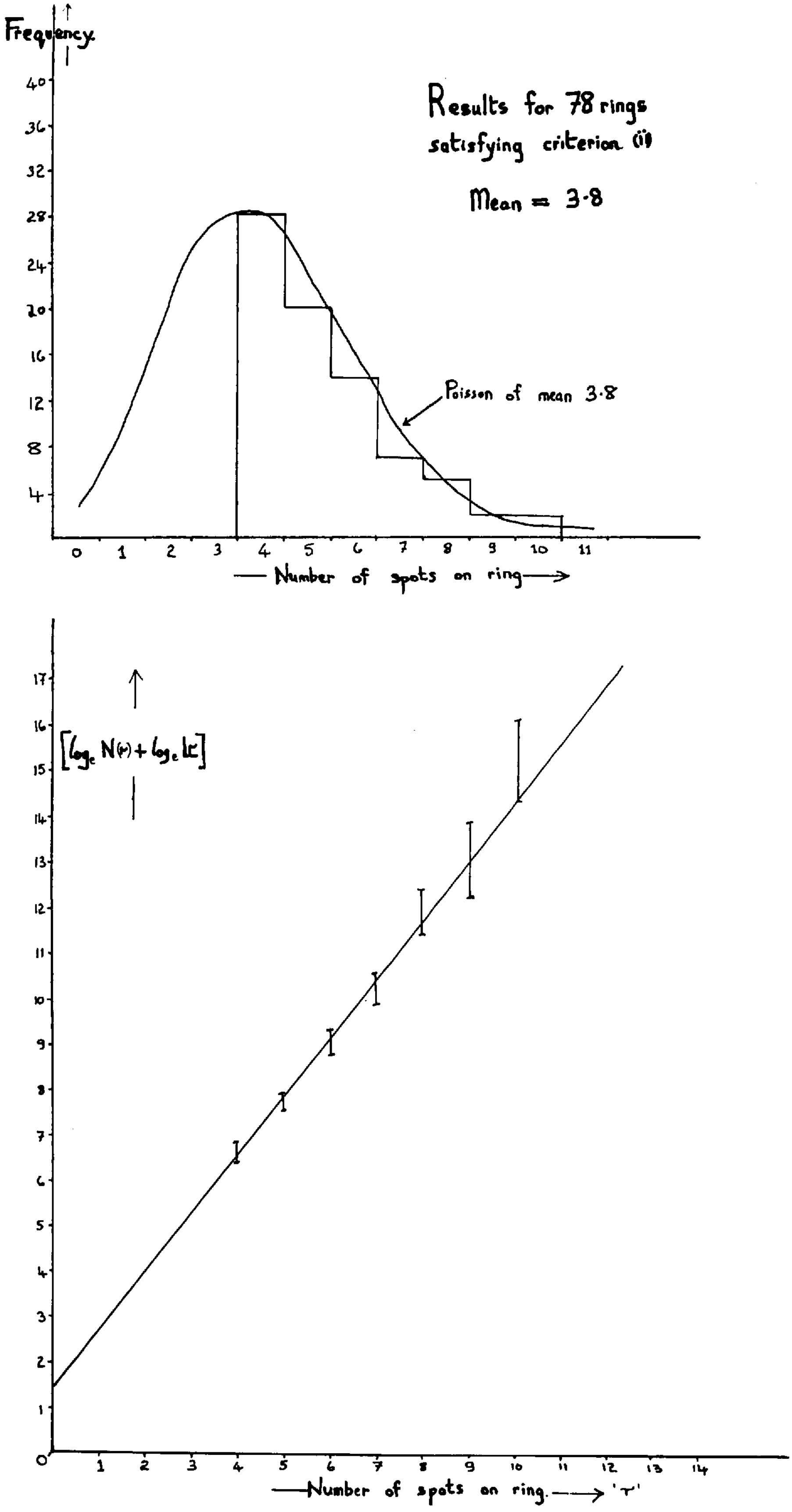
Frequency
40
36
32
28
24
20
16
12
8
4
Results for 78 rings satisfying criterion (i)
Mean = 3·8
Poisson of mean 3·8
0 1 2 3 4 5 6 7 8 9 10 11
Number of spots on ring
17
16
15
14
13
12
11
10
9
8
7
6
5
4
3
2
1
0
$[\log_e N(r) + \log_e \lfloor r]$
1 2 3 4 5 6 7 8 9 10 11 12 13 14
Number of spots on ring 'r'

Fig. 23 (a) & (b)

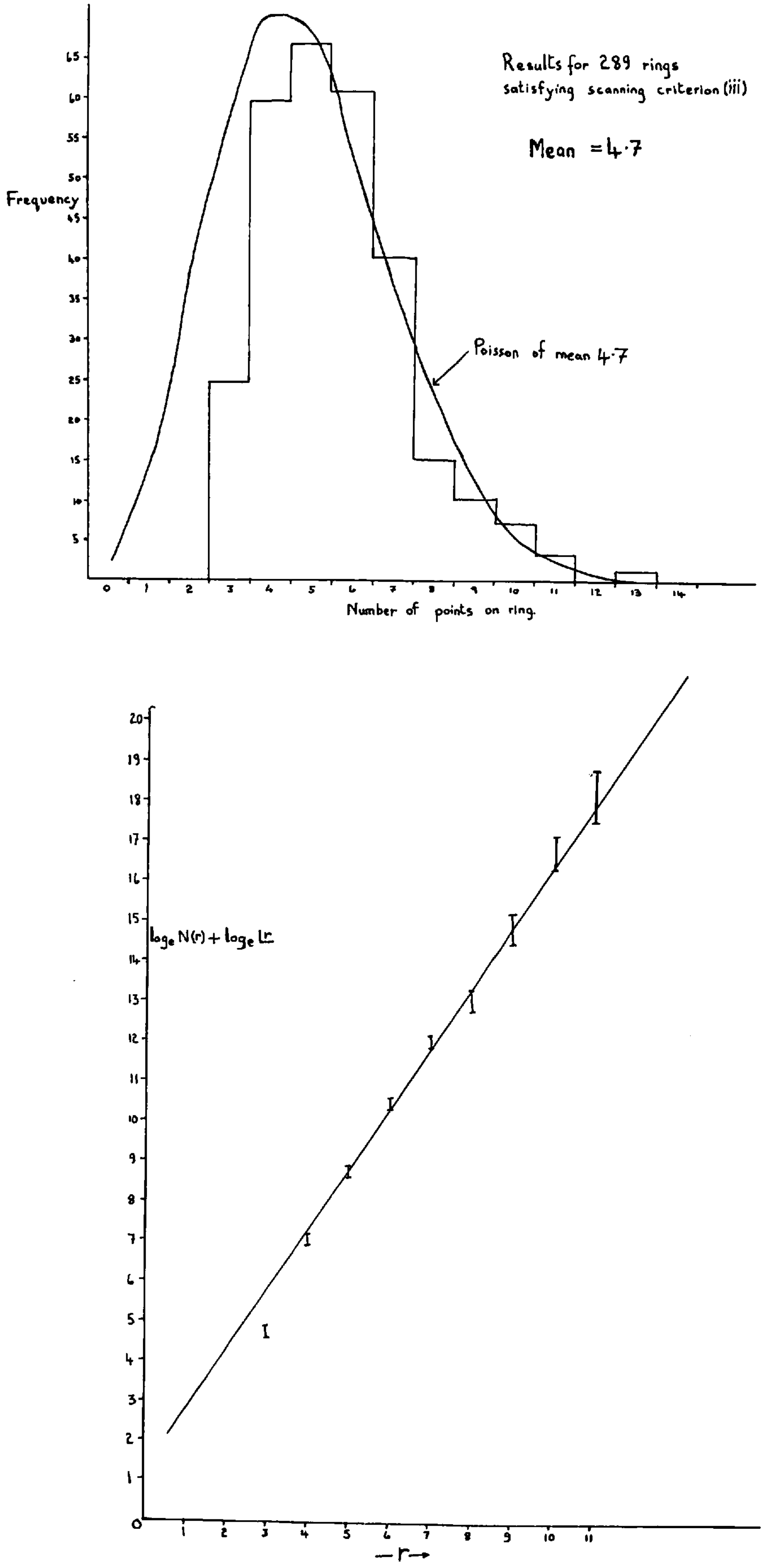
Results for 289 rings
satisfying scanning criterion (iii)
Mean = 4·7
Frequency
Poisson of mean 4·7
Number of points on ring.
0
1
2
3
4
5
6
7
8
9
10
11
12
13
14
5
10
15
20
25
30
35
40
45
50
55
60
65
$\log_e N(r) + \log_e \lfloor r$
—r→
O
1
2
3
4
5
6
7
8
9
10
11
12
13
14
15
16
17
18
19
20

Fig. 24 (a) & (b).

or less, and by the non-linearity of the log plot. Another criterion would have been to include all rings that could be fitted on the photocathode, even if some could also be fitted so as to fall partially off. It is likely, however, that this criterion would tend to enhance the number of rings with a low spot number by including as on the photocathode some rings which were falling largely outside the sensitive area.

It is reasonable to conclude that the ~~time~~ true mean number of recorded spots for 16 mm. rings lies between these values (i.e., between 3.8 and 4.7), and this sort of accuracy was felt to be justified when the other irreducible systematic errors in the estimate were borne in mind. The computed figure for a 16 mm. diameter ring was 12, but this number was also subject to a number of uncertainties. The main assumption here was that the quantum efficiency versus wavelength curve for the tri-alkali photocathode was based on a linear reduction by 2/3 (so as to correspond to 100 microamps per lumen) of a standard E.M.I curve for 150 microamps per lumen tri-alkali photocathodes. Other small errors arise from the difficulty of knowing the exact ring diameter (the number of points on a ring was proportional to the ring diameter over the range of angles covered) and the exact cut-offs of the glass elements in the system. Bearing these uncertainties in mind it was concluded that our image intensifier system recorded about 1/3 of the photoelectrons from the photocathode, though the figure could be as high as 50% or as low as 20%.

CHAPTER 7

Beam Profiling Experiments

7.1 The Requirements for Beam Profiling and Beam Study

The cross-sectional area and flux of a particle beam from a high energy accelerator vary widely depending on the nature of the beam and the use for which it is intended. The diversity of beams is best illustrated by taking two examples of beams which are at present being designed for use at the Nimrod accelerator of the Rutherford Laboratory. In a proposed external proton beam for use with an external target, it is hoped that about half the circulating protons will be successfully transported and focussed onto an area on the target about ½" diameter, with an angular spread of a few degrees.[49] The flux which it is hoped will be ultimately obtained with this accelerator is $\sim 10^{12}$ protons per pulse, so that $\sim$ few times 10^{11} protons can be expected in the external beam. During the setting up process it will, of course, be much lower, but will still remain a very high flux beam up to the external target. At the other extreme in particle flux is the output obtained from separated K^- meson beams. A proposed K^- beam at Nimrod [50] would have $\sim$ tens of particles per 10^{11} circulating protons, with a linear separation $\sim$ millimetres from the contaminating π^--mesons. The spill-out time of particle beams is dependent on the experimental requirements, and can be varied from 50μsec. to 100msec.

For all these beams the electron-optical problems are tackled by computational methods using specially written computer programmes capable of handling the parameters of standard quadrupole magnets, bending magnets and separators.[51] Because of the complexity of the electron-optics and the non-ideal characteristics of the elements used for the beam optics, there is a need for a visual monitor to look at the beam profile during the setting up stages. The final adjustments for optimizing the beam may then be carried out with reference to the visible cross-sectional profile of the beam. A monitor capable of accurately locating single particles would be particularly useful for looking at the clusters of separated particles emerging from an electrostatic separator.

The desirable features of a versatile beam monitor are summarized below:

(i) Ultimate sensitivity; that is, the ability to record single minimum ionizing particles. This enables accurate quantitative estimates to be made for weak beams, and combined with the other requirements listed below, enables particle identification in a separated beam.

(ii) Spatial resolution ~1mm. or better.

(iii) Flexible triggering facilities. An ideal beam monitor would trigger off any or all the particles in a beam pulse, including the ability to trigger for all particles of a certain class. (e.g. K^- mesons). A device with this facility, and having a short memory (~few μ sec.) has complete versatility.

(iv) Reference or fiducial marks to enable the coordinates of the beam profile to be determined.

(v) Minimum interference with the beam particles. It is desirable that the particles should traverse the minimum amount of material, so that the profiling device does not degrade the momentum or directional qualities of the beam, or introduce other contaminating particles at this stage. The monitor can then be incorporated as a permanent device, and in some experiments would provide useful additional information.

(vi) Physical size. The location of the electron-optical elements and the physical separation between them, together with the presence of concrete shielding walls, is often such that the amount of space available for the beam profiler is very limited.

It is important, therefore, to bear this practical need in mind when considering the size and shape of a monitor.

Up to the present, all methods of beam profiling fall short of these features. Direct photography of the scintillation light produced in a thin sheet of scintillator placed perpendicular to the beam direction is limited to high particle fluxes because the necessary gain requirements are not met. Using a 0.9" thick NaI(Tℓ) crystal as the scintillator, Sard [52] found that a flux of greater than 2 times 10^5 minimum ionizing particles per cm^2

was the minimum intensity that would produce just detectable development on Polaroid type 47 film. For most secondary particle beams this would mean long continuous exposures.

Another method that has been used is to scan the beam with a small scintillation counter whose scintillator is of the appropriate shape for the beam, and plot the counting rate as a function of the position of the counter. This method is tedious to use, and more elaborate scintillation counter hodoscopes have been made,[58] but the spatial resolution obtainable with such arrays is limited if the number of counter channels is to be kept reasonably small.[53] Recently single gap spark chambers have been developed which record single particles with a spatial resolution of 1mm;[54, 55] the sensitive time is short (~0.6 μsec.), and the dead time (defined as the time after sparking during which a second high voltage pulse will reignite the spark) is ~4msec., so that usually only one particle can be photographed per beam pulse.

A slightly modified form of the scintillator-intensifier system described in Chapter 5 makes a very refined and versatile beam profile monitor, meeting all the requirements that have been mentioned.

7.2 The Scintillator-Intensifier System as a Beam Profile Monitor.

The idea of using a scintillator-intensifier system for beam monitoring was first suggested by Jones and Perl,[56] who used a 4" square bundle of 1mm. plastic scintillator fibres butted up against a Westinghouse WL 7257 image tube. The intensification obtained was insufficient to enable single photo-electrons to be recorded with high efficiency and particle densities of $10^3/\mathrm{cm}^2$ were necessary to give a visible image of the beam. More recently, Waters et. al.[57] have constructed a profile monitor using a plastic scintillator fibre bundle butted onto an R.C.A. single-stage intensifier, type C70035. This latter tube is coupled to an R.C.A single-stage intensifier orthicon type C74036 and the system has sufficient gain to record individual beam particles.

It is instructive to consider the possible combinations of image tubes and scintillating material that could be used for beam profile work. Fig. 25 is a schematic diagram of four such combinations. In the most straight forward modification of the scintillation chamber experiments, a flat sheet of scintillator is placed perpendicular to the beam direction, and viewed with a conventional lens system (Fig. 25(a)). An "end-on" image of the particle track produced in the scintillator is focussed on the photocathode so that the spatial resolution obtained depends on the thickness of the scintillator, the aperture of the coupling lens and the position of the track. By inserting a reflecting surface between the scintillator and lens, the particle beam need only traverse the scintillator itself. Referring to Fig. 26 it can be seen that provided the scintillator thickness is very much less than the object distance of the lens, and the collection

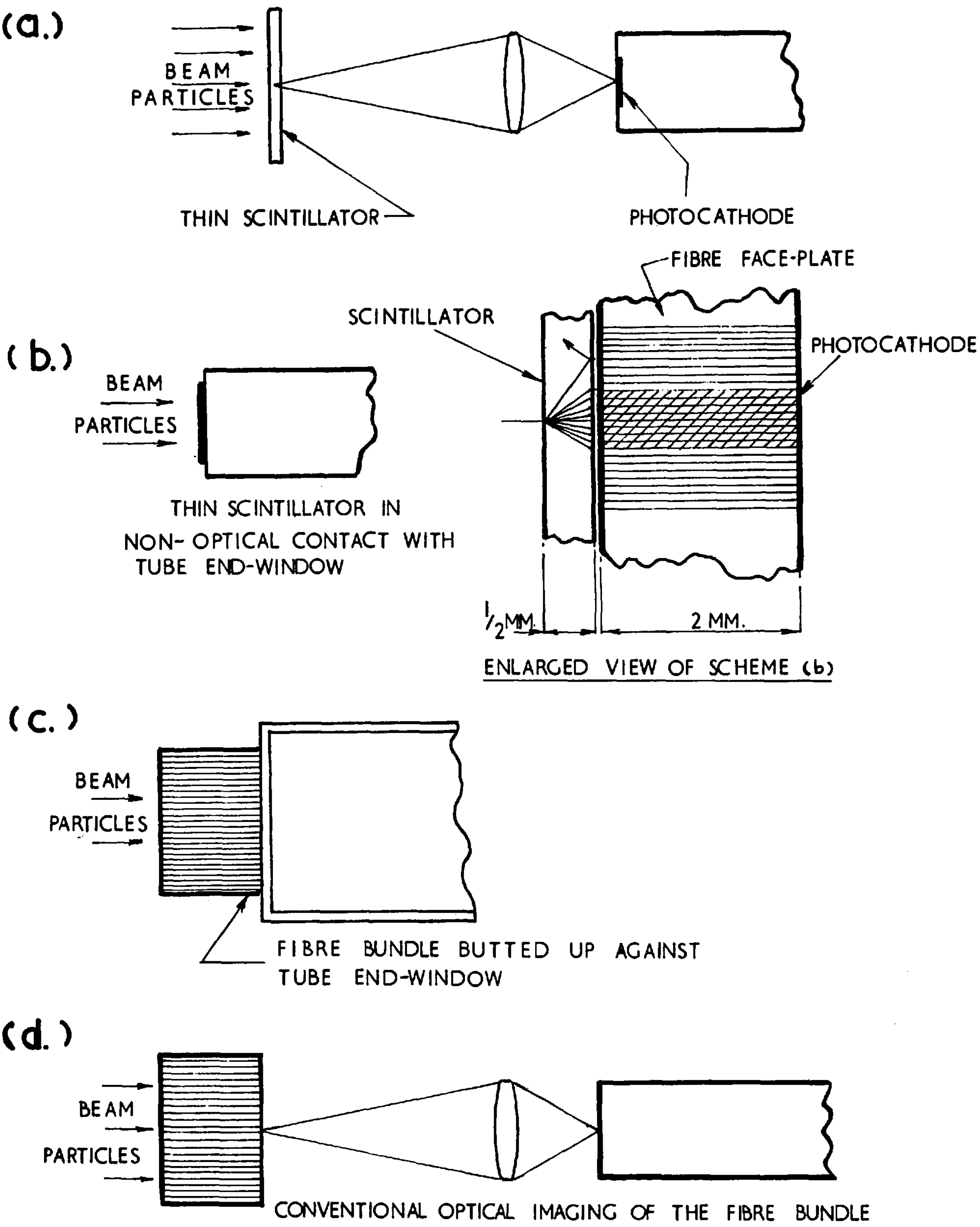

FIG. 25. FOUR POSSIBLE BEAM PROFILE ARRAGEMENTS USING IMAGE INTENSIFIERS

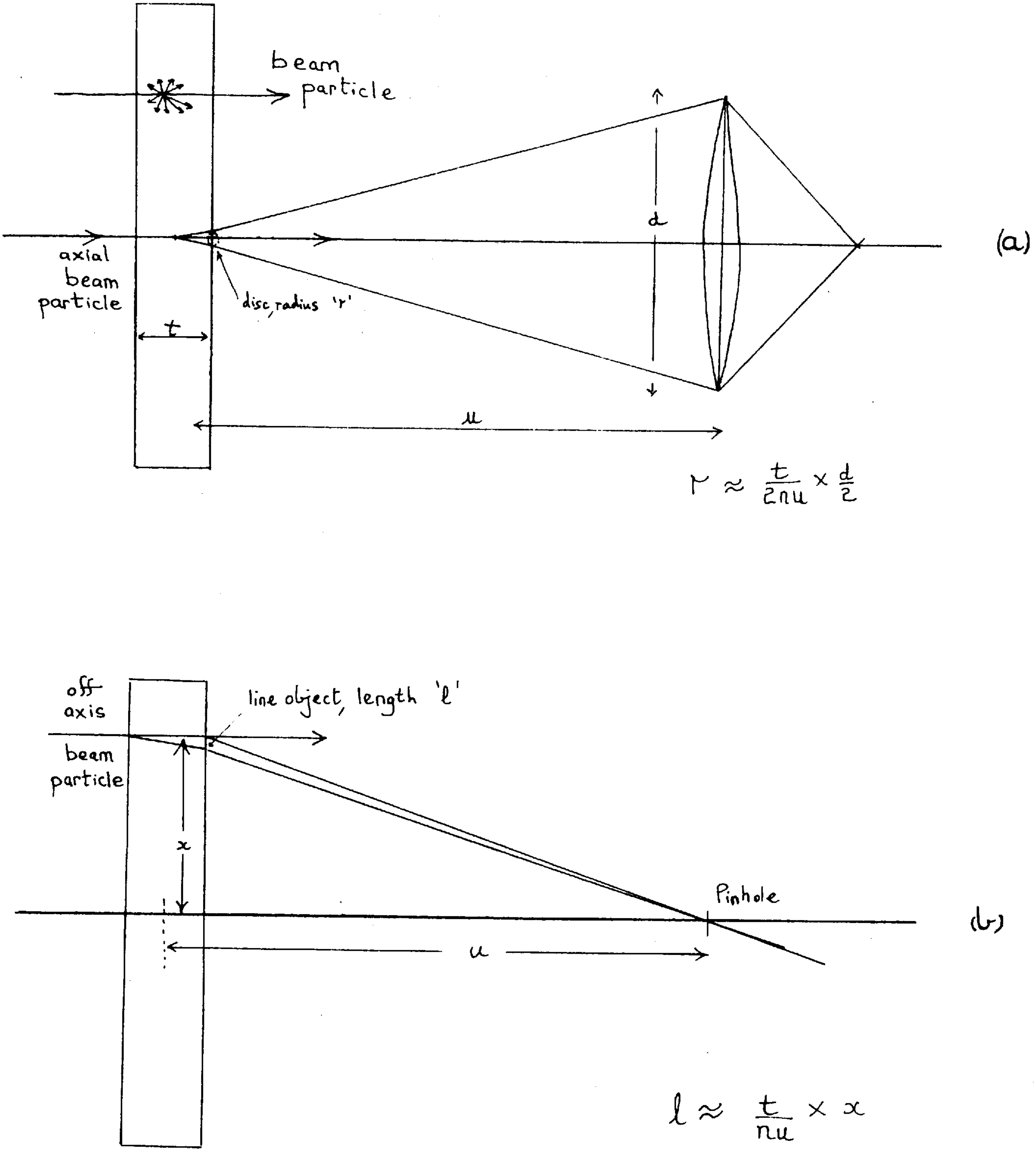
beam particle
axial beam particle
disc radius 'r'
t
d
u
$r \approx \frac{t}{2nu} \times \frac{d}{2}$
(a)
off axis beam particle
line object, length 'l'
x
Pinhole
u
$l \approx \frac{t}{nu} \times x$
(b)

Fig. 26. (a) & (b).

angle is small, the collection efficiency for light varies very little along the 'track' length and can be taken as constant and equal to the collection for the median plane of the scintillator sheet for the purpose of estimating the signal to be expected at the photocathode. The formula of eq. (5.1) can thus be used to estimate the number of photo-electrons obtained from a minimum ionizing particle.

An impression of the shape of the particle image under different conditions can be obtained by considering, in turn, the effect of the lens aperture and the particle position on the image shape. With an axial particle, and assuming the conditions mentioned above, the light patch in the object space is a circular area of radius 'r' given by:

$$r \approx \frac{t}{2nu} \times d/2 \text{ ....eq.(7.1) (see Fig. 26(a))}$$

For an off-axis particle imaged by a pin-hole onto the photocathode the light patch is a line object of length;

$$\ell \approx \frac{t}{nu} \times x \text{ ....eq.(7.2) see Fig.26(b)}$$

In general, a combination of both these effects is present giving a roughly sausage-shaped object patch whose length is approximately equal to 'ℓ', and of approximate width '2r'.

An alternative approach is to butt a thin scintillator directly against the glass end wall of the image tube (Fig.25(b). All the light contained in a cone of half-angle equal to the critical angle would hit the photocathode. Thus for plastic scintillator, giving 20,000 photons per cm. for a minimum ionizing particle, a thickness of ½mm. is sufficient to give one photo-electron, assuming 10% quantum efficiency and 1/3 intensifier recording efficiency for photo-electrons. With an ordinary glass end-window tube the spatial resolution is poor ($\sim \pm$ 3mm), but could be improved by having a fibre end-window. The field of view is confined to the sensitive area of thephotocathode, and the particle beam must go through the intensifier system. For particles having $\beta \geqslant 0.67$, the Čerenkor light produced in the glass wall of the tube produces sufficient photons to record the particle position.

In Fig. 25(c), the method used by Reynolds, and by Jones and Perl is shown. Quoted scintillation efficiency for plastic fibres is ~16,000 photons/cm. for minimum ionizing radiation, of which ~20% is piped to the end. A 1cm. long bundle would yield ~50 photo-electrons using the same assumptions as in the above estimates and putting in a factor of 2 for light attenuation in the fibres. Again, direct butting to the end window gives poor spatial resolution unless a fibre end-window is used. This system suffers from the other disadvantages of scheme (b).

Finally, a fibre bundle can be optically coupled onto the photocathode as in Fig. 25(d). With a F/1 4 : 1 demagnifying lens, about 1 or 2 photo-electrons could be expected for a 1cm. long bundle.

The high efficiency of recording photo-electrons obtained with the intensifier system described in this thesis means that the more elaborate arrangements of fibre scintillators and fibre end-windows do not give any advantages and are less flexible in many respects than scheme (a), so that only the latter system was investigated at Saclay. There is normally no high resolution requirement from the amplifying system for most beam profile work.

7.3 Experiments and Results.

Both the CsI(tℓ) crystal (¾" thick) and the plastic scintillator (1" thick) were used for the beam profile experiments; the Dallmeyer f/1.42 5" focal length condenser doublet was used at 2.7 ±.1 demagnification, and the 45° mirror system of the Čerenkov apparatus was used to keep the intensifier system at right angles to the beam direction.

A P.24 phosphor was used on the first tube throughout the runs, so that the memory was $\sim\mu$secs. Pictures were taken both with the paralysis circuit 'on', so that only one particle per beam pulse was photographed, and with the paralysis 'off', so that every particle in the beam pulse which passed through the counters was recorded on one film frame. Fig. 27 is a frequency histogram of the number of spots recorded in the case of single particle exposures in plastic. A Poisson distribution is also fitted to the data; the probability of one or more recorded spots per particle is 68%.

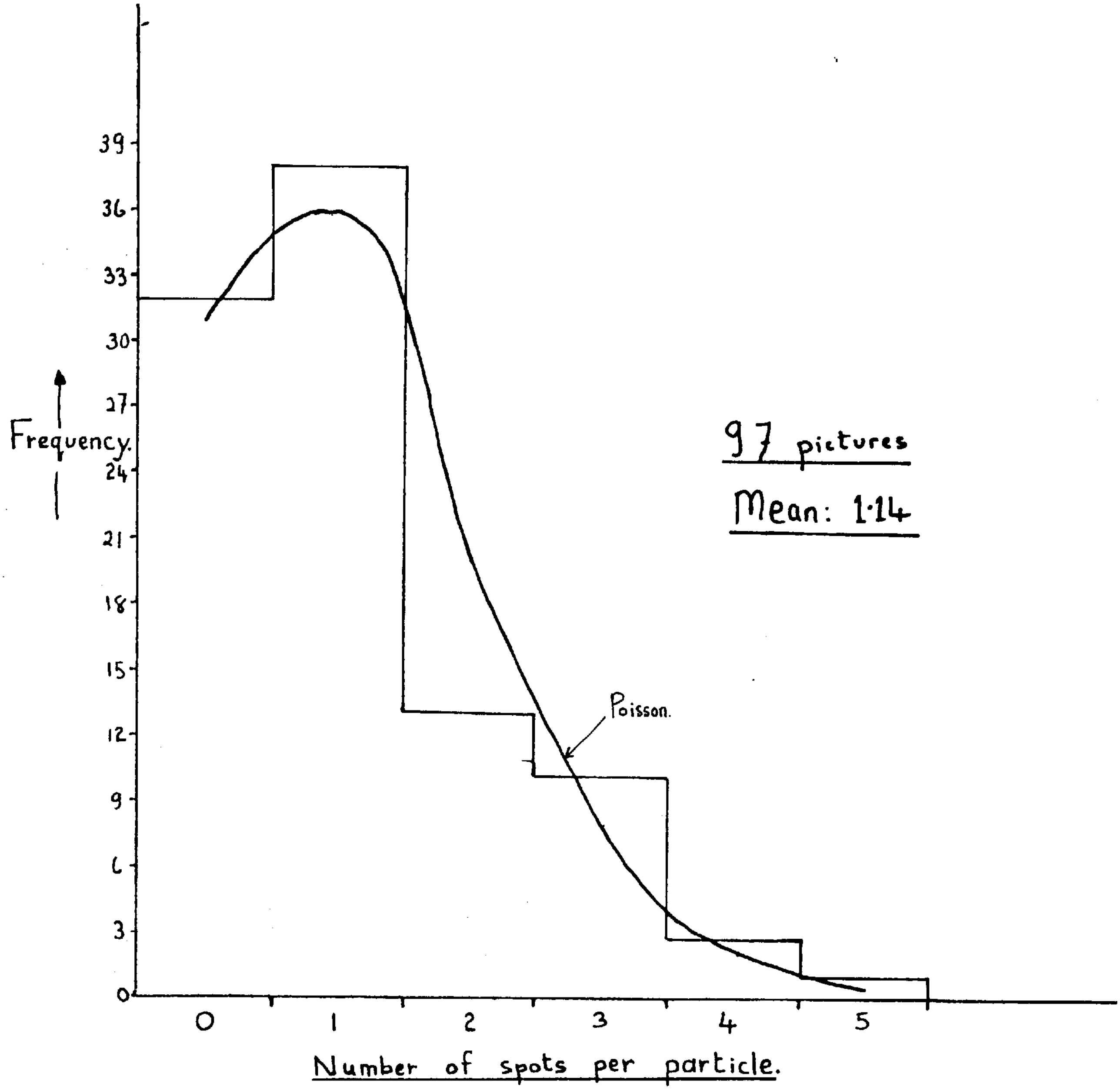

Fig. 27. Frequency histogram for 1" thick plastic scintillator used as a beam profiler.

Fig. 28 is a photograph of (a) ~~several hundred~~ ~ 50, and (b) many hundreds of particles obtained by recording the spots from particles for several beam pulses on one frame of the film. The outline of the 2cm. by 5cm. selection counters used to trigger the image tube system can be seen in (b).

An estimate of the number of background or 'noise' spots was obtained by counting the number of spots occuring outside the counter area. 9 spots were recorded in 98 frames, giving a figure of $\sim 5{,}000$ /cm.^{2}sec. Since this is much higher than the expected intensifier noise for a 5 μ sec. gating period, these spots must arise from reflected scintillation light, and to a lesser extent from Čerenkor radiation.

The average number of scintillation spots per particle that could be expected theoretically is given by

$$N_{p\,e} = \frac{\eta\, t \int P(\lambda)\; T(\lambda)\; S(\lambda)\, d\lambda}{16A^2m^2n^2} \ldots\ldots\ldots \text{eq.}(7.3)$$

where; 'η' is the recording efficiency for photo-electrons,

't' is the crystal thickness in cm.,

and $P(\lambda)$, $T(\lambda)$, $S(\lambda)$, A, m, and n have the same significance as in eq. (5.1).

$P(\lambda)$ and $S(\lambda)$ were not known exactly in this experiment, but since 'η' was not accurately known it was decided that the values corresponding to the peak wavelength of plastic scintillator could be used as was done for the estimates of 'η' in Chapter 5.

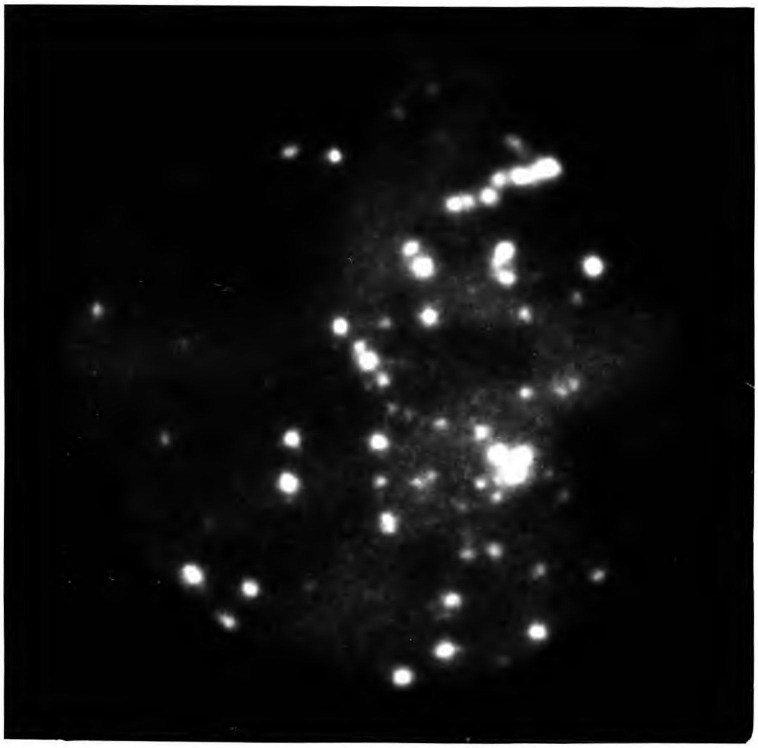

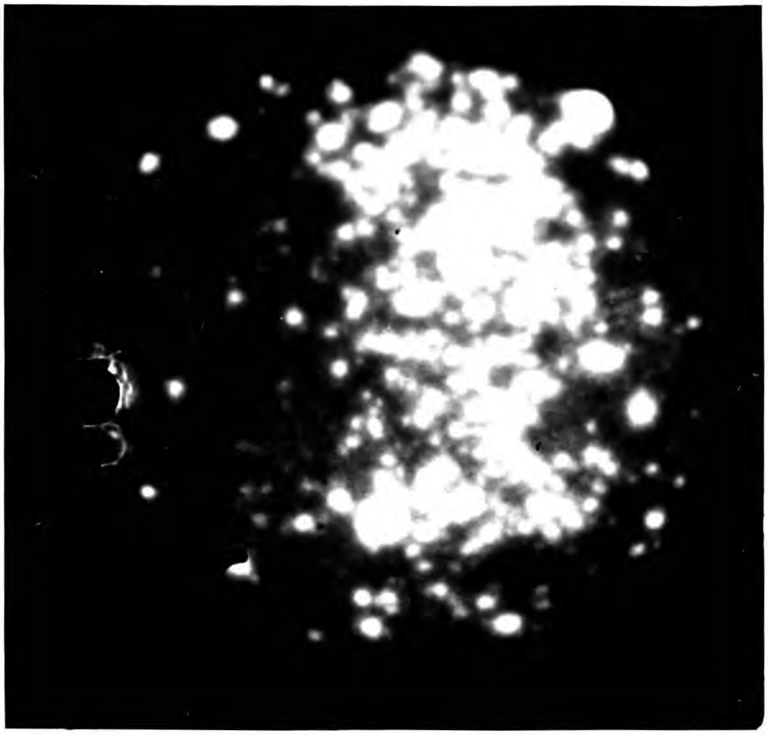

Fig28(a). Beam profile of ~50 beam particles in 1 inch thick plastic scintillator

Fig28(b). Beam profile of many hundreds of particles. The rectangular outline of the selection counter can be seen.

Thus eq. (7.3) may be rewritten;

$$N_{pe} = \frac{\eta\, t\, P\, T\, S}{16\, A^2 m^2 n^2} \quad \text{................eq. (7.4)}$$

The calculated value for N_{pe} using the values 20,000 photons/cm for P, 85% for T, 10% for S, and 1/3 for η was 1.4 photo-electrons, giving the probability of 75% of having one or more recorded spots per particle. This in in reasonable agreement with the observed efficiency of 68% when the possible variations in η , P and S are taken into consideration.

Fig. 29 shows a histogram of recorded spots per particle against frequency when the CsI(tℓ) crystal was used as the scintillator; a Poisson curve is again superimposed. In this case, the computed mean is 3.6, giving a probability of 98% for getting one or more recorded spots per minimum ionizing particle,but the beam has to traverse 8.60 gm. of CsI compared with 2.63 gm. of plastic in the previous experiment. Using eq. (7.4), and assuming 5% for the absolute efficiency of the CsI(tℓ) crystal [48], the theoretical mean expected number of spots is 3.8, and the corresponding recording efficiency is ~98%, as would be expected.

Fig. 30 shows clusters of spots corresponding to single particles traversing the CsI(tℓ) crystal; the object plane of the lens was displaced slightly from the median plane of the crystal so that the spots making up the clusters would be separated out to facilitate counting the numbers in each cluster.

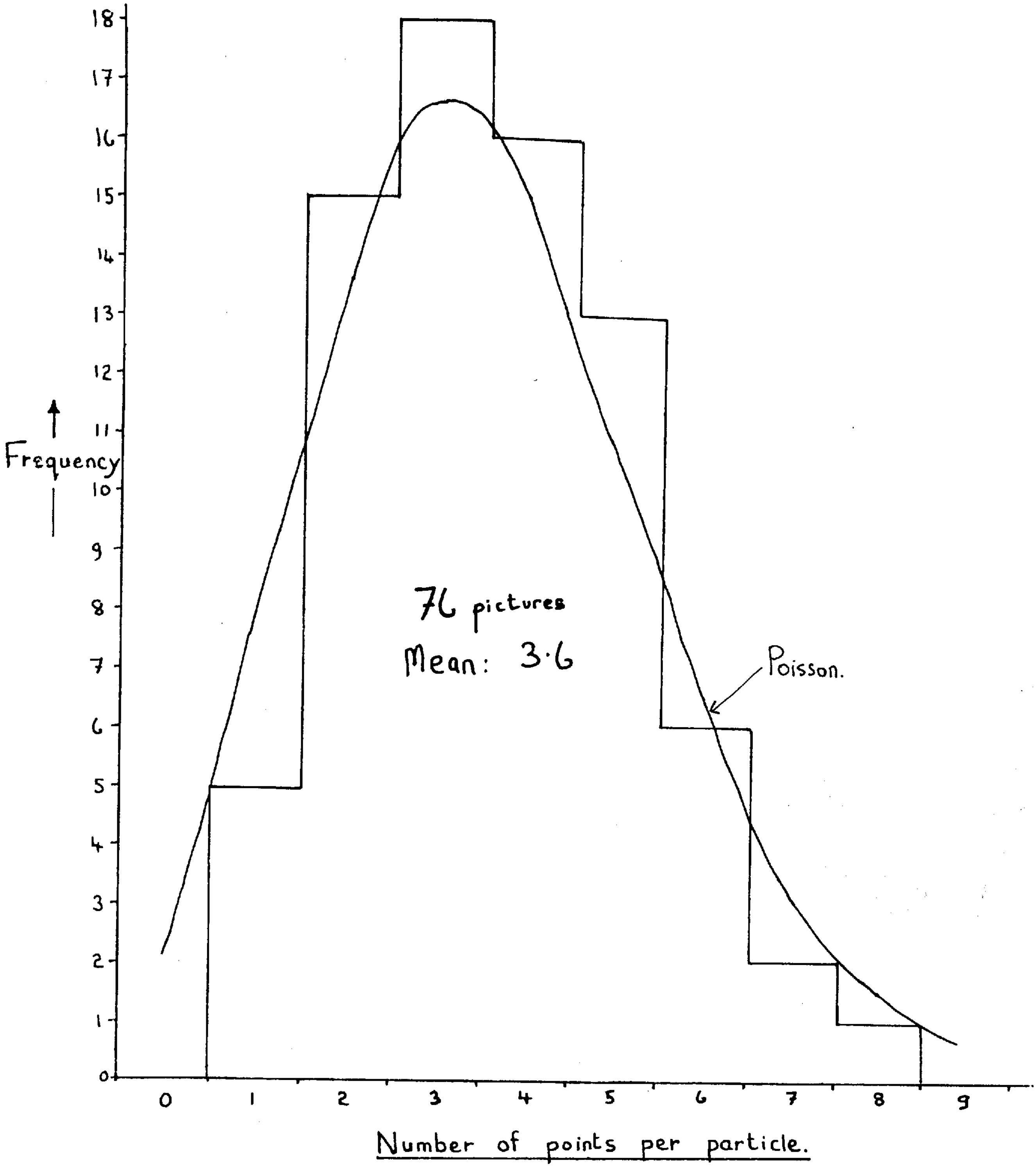

Fig. 29. Frequency histogram for CsI(Tl) crystal $\frac{3}{4}$" thick used as a beam profiler.

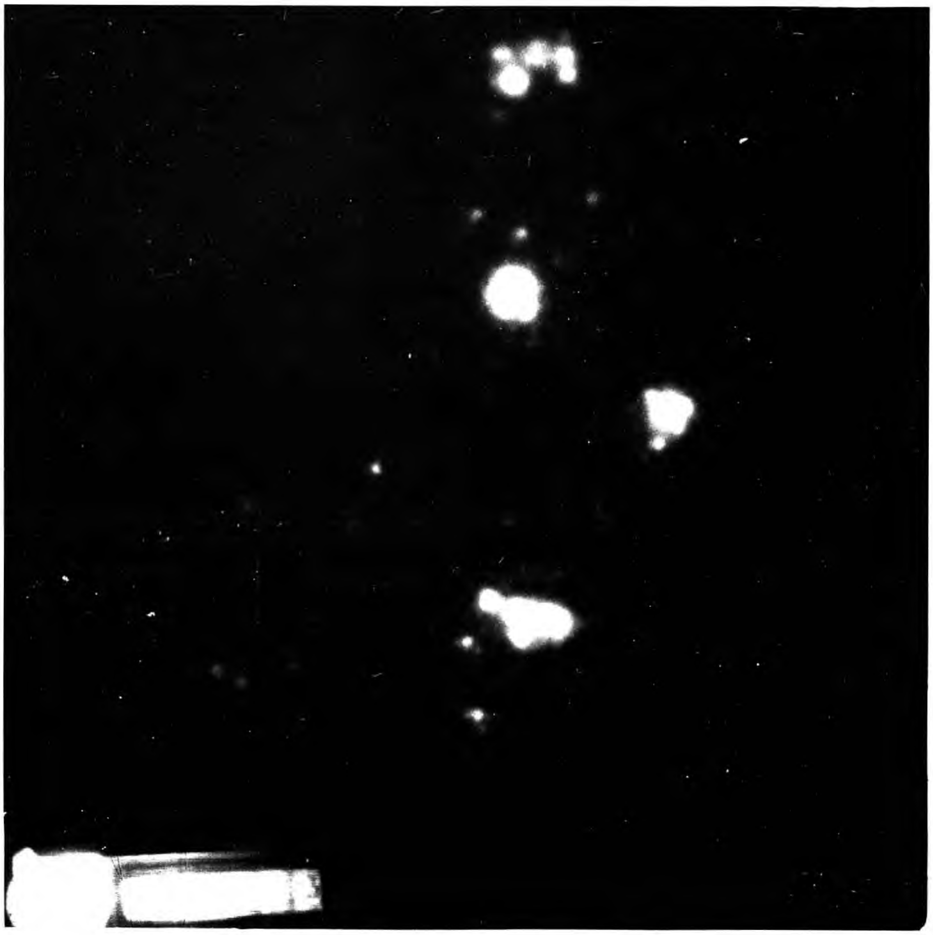

Fig. 30. Beam profile of 4 minimum ionizing particles in a 3/4" thick crystal of CsI(Tl). It can be seen that each particle is represented by a cluster of scintillation spots.

7.4 Development of a Beam Profiler.

The capabilities of the present image intensifier system as a beam profiler are illustrated in Table F, where the properties of two types of systems have been worked out, based on the results given in section 7.3. The first system has a high efficiency for recording single particles and good spatial resolution but a small field of view. It would thus be suitable for looking onto low intensity separated beams. The second system has a field of view of 20 cm., operating at 8 : 1 demagnification, and would be suitable for looking at high intensity beams. Beam profile equipment based on the Saclay type transmission secondary emission image tube set-up and incorporating a T.V. viewing system is at present being built at Imperial College.

Table 'F'

	Diameter of Field.	Scintillator used.	Magnification.	Lens parameters	Precision of Location		Recording Efficiency for single particles
					on axis	at edge	
System (a)	2·5cm.	1mm. of CsI(Tl)	1:1	$f/1$ 10cm focal length	~0·25mm.	~0·25mm	75%
System (b)	20cm.	25mm. of NE102 plastic scintillator.	8:1	$f/1$ 5cm. focal length	~0·2mm	~0·6mm	45%

CHAPTER 8

Present and Future Nuclear Physics Applications of Scintillation Chambers and the Čerenkov Camera.

8.1 Introduction.

The purpose of the present chapter is to examine the uses in current and future nuclear physics research of the techniques that have been described in this thesis. Experimental techniques in high energy physics are progressing at a very rapid rate, and several new devices (notably the spark chamber) have come into common use in the field during the past two years. The particular advantages and limitations of the scintillation chamber and Čerenkov camera techniques are considered in the light of recent and possible future developments.

8.2 Homogeneous Chambers and Fibre Chambers.

The present performance of homogeneous chambers and fibre chambers, as illustrated by the work of this thesis and by experiments carried out by other authors, is now fairly well established. To enable certain general comparisons to be made, the essential parameters will be summarized, but since the whole technique is dependent on developments in image tube technology these arguments could be radically changed in the future.

It is possible to envisage NaI($t\ell$) and CsI($t\ell$) chambers having spatial resolution $\sim$ 1mm., and with an usable depth of field up to 6" for most track recording purposes, so that with

90° stereoscopic viewing, two out of three dimensions are limited to about 6" by the depth of focus. By having the stereoscopic views at a more acute angle, and looking through the same face of the chamber, the depth of field limits one dimension only. The other two dimensions are then restricted by the photocathode size to about 20 to 30 cms. at present. For less efficient scintillators, such as plastic or glass, a comparable performance in terms of a similar number of recorded spots per cm. in chamber space would mean a smaller chamber in all three dimensions.

The choice of chamber material depends on the nature of the experiment; NaI(tℓ) and CsI(tℓ) have a high density and high atomic number whereas plastic scintillator has a higher hydrogen content and can tolerate higher fluxes of neutrons and γ-rays than alkali-halide crystals of the same size. Compared with fibre chambers, homogeneous chambers have the advantage of ease of construction and comparatively straightforward optical coupling. The quality of the plastic fibres that have been used up until now has limited the useful depth of a fibre chamber to a size which is very comparable with homogeneous chambers (i.e. $\sim$ 6"). A fibre chamber of this depth, however, suffers from the rather serious disadvantage for some experiments that the amount of light received from a particle is not only a function of its energy loss, but also depends on the distance from the fibre ends that the scintillation light occurs. This makes the interpretation of ionization information more difficult for fibre chambers. The chamber backgrounds, either due to scattered scintillation light from a homogeneous chamber, or caused by "cross-talk" between the fibre light-pipe is very similar. Finally, the choice between fibres or a homogeneous chamber may depend on the special selection methods and shapes required in an experiment.

The intrinsic resolving time of a scintillation chamber is ultimately limited to the decay time of the scintillation light, which is as low as 5nsec. for plastic scintillator. (The actual transit-time of a particle within the chamber volume would also be a limiting factor of the same order for chambers several tens of centimetres across). At the moment conventional selection methods and switching demand that a memory $\sim$ few times 10^{-7} sec. be incorporated in the system before the switched element, but rapid progress is being made in the field of fast electronics for counter circuits, and Fischer and Zorn[59] have recently described a spark chamber triggering system (where essentially the same problems arise) having a total delay $\sim$ 33nsec. It is probable, therefore, that the resolving time of scintillation chambers could be reduced to $\sim 10^{-7}$ sec.

The flexible time resolution and triggering facilities of the scintillation chamber can be exploited in a novel way by deflecting the image on the phosphor of the first tube and using different parts of the phosphor surface at different times. A nice example of using scintillation chambers in this way is the muon capture experiment of Reynolds[21] mentioned in Chapter 2. In order to time the B^{12} beta decay back to C^{12}, the fibre chamber was divided into several sections and the counter selection system was such that if no decay electron was indicated within 10 μsec of the muon coming to rest, the kinescope was gated on, and a clock began generating pulses at 1msec. intervals. Two milliseconds after the muon had stopped, the image of the chamber was deflected on the output phosphor of the first tube in the system so that the B^{12} decay electron could be recorded in a separate part of the picture. An image of the time clock was automatically flashed onto the film when the counters detected the decay electron.

The method of deflecting the phosphor image could also be used to enable the time between certain events in the chamber (such as particle decays) to be measured by measuring the displacement between tracks and knowing the sweep rate of the deflecting coils.

8.3 Scintillation Chambers versus Spark Chambers.

The capabilities of spark chambers have developed so rapidly during the past eighteen months that a large number of the features possessed originally only by scintillation chambers can now be exploited using spark chambers. Individual sparks can be measured to a spatial precision of $\frac{1}{2}$mm., and the gaps between plates can be as little as 2mm. This gives a spatial resolution comparable to that of scintillation chambers. The plates themselves vary in thickness and material down to 0.002cm. sheets of aluminium so that much lower average densities can be attained if necessary. Plane parallel plate chambers and concentric cylindrical plate chambers have been constructed.

Tracks can be photographed up to angles of 45° to the plate direction before multiple sparking occurs and angles can be measured to fractions of a degree with comparative ease. The resolving time of spark chambers is comparable with the present scintillation chamber figure of $\sim 1\mu$sec. (but will probably be improved in the future as was mentioned in section 8.2), and their recovery time is ~ 10 to 20msec. Of important practical value is the simplicity and ease of construction and operation of the spark chamber as compared with the scintillation chamber. Moreover, the large sizes (up to several metres cube and weighing several tons) of spark chambers is essential for experiments such as the recent 'ν' experiments of Danby et.al.[60] at Brookhaven.

There are two advantages that the scintillation chamber retains over spark chambers. First, the scintillation light produced is a function of the energy loss of the particle traversing the chamber, and second, it provides a chamber volume having isotropic sensitivity. The usefulness of these properties will depend very much on the experiment. At high energies, both of these advantages are less important; the first because the particles involved are nearly always minimum ionizing, and the second because the reaction products tend to be peaked forward.

Sodium and Caesium Iodide chambers provide excellent range measurements for muons, pions and protons at moderate energies. For example, referring to the curves of appendix D, protons of 20MeV kinetic energy have a range of 0.2cm. in NaI(tℓ) and a 5MeV energy spread means ± 1mm. in the range. 200MeV protons travel 11.5cm in NaI(tℓ) and have a range of ± 5mm for a 5MeV energy spread. Thus it is possible to measure to about 5MeV over this range using a NaI(tℓ) chamber of $\sim$ 15cm. diameter. If a lead plate spark chamber were used instead, a 20MeV proton has a range of 1gm. of lead whilst a 200MeV proton has a range of 54gm. of lead, so that to enable the energy of theprotons to be measured to 5 MeV using a spark chamber 130 plates of thickness 0.35mm. would be required making the chamber $\sim$ 1.3 metres long.

Both devices are especially useful for looking at rare events when the presence of high background due to conventional secondaries would swamp other track devices having a much less sensitive resolving time, and without the facility of counter controlled selection, whilst the poor opatial resolution of conventional counter arrays makes it difficult to identify the required event against the spurious background counts.

It is sometimes an added advantage of the scintillation chamber that the scintillation light, as well as being imaged to give the trajectory of the event being examined, can be measured separately by viewing the chamber with a photo-multiplier array. This gives a direct measure of the energy loss in the chamber and can provide a vital selection 'handle' for certain rare events.

An excellent example of this mode of trigger selection is an experiment which the Imperial College group intends to carry out using a modified form of the image intensifier system described in this thesis. The experiment is a search for a decay mode of muons into three electrons;

$$\mu^{\pm} \longrightarrow e^{\pm} + e^{\pm} + e^{\mp}$$

Experiments carried out using a freon bubble chamber by Crittenden et. al.,[61] and using spark chambers by Parker et. al.[62] and Alikhanov et. al.[63] have established an upper limit to the branching ratio of $\sim 5 \times 10^{-7}$ for this decay mode. In the common decay mode of the muon into one electron and two neutrinos, the electron has an energy spectrum going up to 52MeV, whereas an amount of energy nearly equal to the rest mass of the muon (~ 105MeV) is shared between the 3 electrons in the $\mu \rightarrow 3e$ decay mode. Thus by viewing the chamber with a conventional scintillation counter system and arranging that the scintillation chamber only takes photographs when more than 52MeV of energy is lost in the chamber, the $\mu \rightarrow 3e$ decay mode can be picked out. Various other rare decay processes such as

(a) $\mu \longrightarrow e + \gamma$ (lower limit 6×10^{-8})

(b) $\mu \longrightarrow e + e + e + \nu + \nu$ (lower limit 2.2×10^{-5})

(c) $\mu \longrightarrow e + \gamma + \nu + \nu$ (lower limit 10^{-2} for $E_{\gamma_{min}} \geqslant 10\text{MeV}$)

which have been studied by the above authors and by Bartlett et. al.[64] and Frankel et. al.[65] using spark chambers can also be looked for in the proposed scintillation chamber experiment.

The use of scintillation chambers for space research is being investigated by Doolittle and Graves[66]. These authors comment that the most favourable track imaging devices for space probes or satellites are the spark chamber and scintillation chamber. (Bubble chambers and cloud chambers are at present ruled out by size, weight and complexity, and nuclear emulsion stacks have the disadvantage of having to be recovered and of having no time sensitivity or pre-selection facility). The scintillation chamber has the advantage of being potentially able to distinguish particles of different charge and mass, as well as being isotropic and homogeneous advantages which are important for experiments in space research.

8.4 Extensions of the Čerenkov camera technique for high energies.

The present methods of distinguishing between momentum analyzed particles at high energies are:-

(i) time of flight.

(ii) electrostatic separators.

(iii) radio-frequency separators.

(iv) differential gas Čerenkov counters.

(i) The time of flight technique is the most obvious way of measuring particle velocities. For two particles of velocities

$\beta_1 c$ and $\beta_2 c$ which take times 't_1' and 't_2' respectively to traverse a length 'ℓ', then

$$t_1 - t_2 = \ell\left(\frac{1}{\beta_1 c} - \frac{1}{\beta_2 c}\right) \ldots\ldots\ldots\ldots \text{eq.}(8.1)$$

$$= \ell\frac{(\beta_2 - \beta_1)}{c}$$

The time measurement is at present restricted to $\sim 10^{-9}$sec. so that

$$\ell = \frac{30\text{cm}}{(\beta_2 - \beta_1)} \ldots\ldots\ldots\ldots\ldots \text{eq.}(8.2)$$

At 10GeV/c, a flight path of 70 metres is necessary to distinguish between k-mesons and protons; the flight path goes as the square of the energy or momentum at these high energies. It is clear that these long flight paths become intolerable because of the particle lifetimes and divergences in their directions.

(ii) The difference in angular deflection $\Delta\alpha_{12}$ produced for particles '1' and '2' travelling between two electrodes 'ℓ' metres long having an electric field 'E' is

$$\Delta\alpha_{12} = \frac{E\ell}{p}\,\Delta_{12}\left(\frac{1}{\beta}\right) \ldots\ldots\ldots\ldots\ldots \text{eq.}(8.3)$$

where $\Delta\alpha_{12}$ is in ~~milli~~radians

E is in volts/metre

ℓ is in metres

p is in eV/c

At highly relativistic velocities, this expression can be rewritten as:-

$$\Delta\alpha_{12} = \frac{E\ell}{2p^3}\,\Delta_{12}\,(M^2) \ldots\ldots\ldots\ldots\ldots\ldots \text{eq.}(8.4)$$

where 'M' is the rest mass in eV/c^2

Thus the deflection goes inversely as the momentum cubed. Practical limits exist on 'ℓ' and 'E' because of the decay time of k-mesons and the maximum electrostatic field that can be obtained. With $\ell = 10$m. and $E = 6 \times 10^6$ volts/m. $\Delta\alpha_{12} \approx 2.4\ \mu$radians for k-mesons and protons at 20GeV/c. Sandweiss [67] has considered in detail the design of separators for very high energies, and concludes that beyond ~30GeV/c electrostatic separation would be very difficult indeed; moreover the separators necessary to work up to 30GeV/c are thousands of feet long.

(iii) The problem of using radio frequency separation at very high energies has been discussed by Robertson[68] who describes a separator requiring drift spaces ~280m. at 50GeV and 28km at 500GeV for separating π-mesons and anti-protons; the drift length goes as the square of the energy. He concludes that radio frequency separators are unlikely to be practical above 50 to 100GeV/c.

All the above techniques are being strained to their limits at energies up to ~30GeV and are not likely to be useful at higher energies.

(iv) The problems involved in using a differential gas Čerenkov counter are very similar to the Čerenkov camera and a discussion of the latter is given first.

With the present image intensifier setup, the resolution enables a spot to be located on the photocathode to within 1/10mm. It is reasonable to assume that this figure could be improved upon by a factor of between 2 and 4 using tubes of the present type (i.e. tubes having better resolution over a larger photocathode area), but a greater improvement than this is not easily forseeable with the transmission secondary emission tubes. It will be taken as a reasonable working assumption that, so far as the image tubes are concerned, the radius of an 'ideal' 2cm. diameter ring can be measured to $\sim \frac{1}{2}\%$ for each 'spot' on the ring. It is assumed here that any distortions in the tubes which are of this order or larger have been calibrated out. For some experiments, triggering from a random event is not necessary, in which case a single image tube could be used, giving a better overall resolution than for two tubes in cascade, but the recording efficiency and hence the number of spots defining the circle would be lower. Thus whether a single tube or a two tube system is better depends on the relative values of resolution and recording efficiency for the two systems.

It is interesting to ask what precision in velocity measurement can be attained at high energies when the radius of the Čerenkov ring is measured to the above accuracy. It is shown in Appendix E that the change in 'β' of $d\beta$ corresponding to a change of dr in 'r' is given by:-

$$\frac{d\beta}{\beta} = \frac{dr}{r}\sin^2\theta$$

$$\approx \frac{dr}{r}\,\theta^2, \text{ for small } \theta \text{ ....eq.(8.5)}$$

Also, the momentum change for highly relativistic particles is given by eq.(E.7) of Appendix E:

$$\frac{dp}{p} \approx \gamma^2\theta^2 \; \frac{dr}{r} \text{ ....eq.(8.6)}$$

In eqs. (8.5) and (8.6), a lower limit of 0.005 can be placed on dr/r, so that the only variable left is 'θ'. It is apparent that the velocity resolution becomes more accurate as 'θ' is decreased, but there is a lower limit to the smallness of 'θ' because the intensity of the Čerenkov light is proportional to $\sin^2\theta$ (or θ^2 approximately, for small angles).

The following table shows the values of 'β' for K-mesons and protons at different momenta:

Momentum	$1 - \beta_k$	$1 - \beta_p$
1 GeV/c	1.0×10^{-1}	2.7×10^{-1}
10 GeV/c	1.2×10^{-3}	4.4×10^{-3}
20 GeV/c	3.0×10^{-4}	1.1×10^{-3}
50 GeV/c	4.9×10^{-5}	1.8×10^{-4}
100 GeV/c	1.2×10^{-5}	4.4×10^{-5}
300 GeV/c	1.3×10^{-6}	4.9×10^{-6}
1000 GeV/c	1.2×10^{-7}	4.4×10^{-7}

Thus to distinguish between K's and p's at 50 GeV/c, differences $\sim 5 \times 10^{-5}$ in β must be detectable, and using this value in eq. (8.5), together with 0.005 for dr/r gives $\theta = 100$ milliradions.

The other requirements for the system can now be worked out. For $\theta \sim 100$mr., a lens or mirror of focal length 10cm. is required to give rings 1cm. in radius. To ensure that, on average, 90% of the rings have 3 or more spots, an average of 5 spots per picture must be obtained, and with the present recording efficiency of 1/3 and a photocathode efficiency of 10%, then 150 photons must be incident on the photocathode. Assuming that relatively little transmission or absorption losses take place, this means that $\sim$ 150 photons are needed in a wavelength band which is narrow enough to keep the dispersion error below the image tube precision of ½ % in 'r'. In Chapter 6, an expression for the effect of dispersion on θ was derived:-

$$\left\{\frac{d\theta}{\tan\theta}\right\}_{\beta} \approx \pm\ 0.015\,\Gamma \quad \ldots\ldots\ldots\ldots\ldots \text{eq.}(6.9)$$

For the present case, $\Gamma \sim 0.004$, and θ is 0.1, so that $d\theta/\theta$ or dr/r is $\sim 6 \times 10^{-5}$ which is much smaller than the image tube error.

Referring to eq. (6.2) of Chapter 6, about 40cm. of radiator would be required to yield 150 photons between 4000Å and 6000Å wavelength at a 5° emission angle. This now defines the aperture required to be $\sim$ f/2.5. This length of radiator containing any of the usual gases to give a refractive index ~ 1.004 would not introduce any significant scattering or energy loss error. Working with a 4 cm. diameter photocathode, the acceptance angle of the system would be ± 5° if the rings were required to fall completely on the photocathode.

A conventional differential gas Čerenkov counter having a comparable velocity resolution would be very severely restricted in angular acceptance because the annular diaphragm would have to be made such that dr/r ~ ½ %. At a Čerenkov angle of 5° the acceptance is only 0.5 milliradians.

It is clear that by going down in Čerenkov angle (say to 1°) and increasing the radiator length to maintain the number of spots on the ring the Čerenkov camera can be extended to have velocity resolutions capable of distinguishing between K-mesons and protons at ~ 300 GeV/c, and still have an angular acceptance of ± 1°.

A further recent application of image intensifiers for observing Čerenkov light is worth noting. Hill and Porter[69] have used image tubes to photograph directly the Čerenkov radiation emitted by extensive air showers in the atmosphere. Since the Čerenkov light from a particle in air is emitted close to the particle direction, the angular distribution of light from the shower should be centred about the shower direction. The angular distribution is broadened because of coulomb scattering of the shower electrons. These authors were able to record the Čerenkov light as a bright spot on photographic film, and deduce that angular resolutions $\sim 1^{\circ}$ or better should be obtainable. The technique appears to have possibilities for the study of shower development, and the detection of very large showers at large distances from the axis.

APPENDIX A.

Some Formulae for the Geometrical Light Collection and Depth of Focus in Homogeneous Chambers.

A representation of the problem is shown in Fig. 31(a), in which a thin lens of focal length 'f' and diameter 'd' is used at a demagnification of 'm' to image tracks in a crystal of thickness '2x' and refractive index 'n'.

Using the lens formula, $\frac{1}{u} + \frac{1}{v} = \frac{1}{f}$

or since $u = mv$,

$$\frac{1}{mv} + \frac{1}{v} = \frac{1}{f}$$

giving $u = f(1 + m)$............eq.(A.1)

Now $\theta = \tan^{-1}(d/2u) = \tan^{-1}(d/2f(1 + m))$..........eq.(A.2)

Also, $\frac{\sin\theta}{\sin\theta'} = n$

whence $\sin\theta' = \frac{\sin\theta}{n} = \frac{d}{n\sqrt{\left[d^2+4f^2(1+m)^2\right]}}$

and $\cos\theta' = \frac{\sqrt{\left[d^2(n^2-1) + 4n^2f^2(1+m)^2\right]}}{n\sqrt{d^2 + 4f^2(1 + m)^2}}$.............eq.(A.3)

The fraction of the total solid angle which is collected by the lens is: $F_1 = \frac{(1 - \cos\theta')}{2}$

and substituting for $\cos\theta'$ from eq.(A.3) and putting $f/d = A_o$, we have:-

$$F1 = \frac{1}{2}\left\{1 - \sqrt{\frac{n^2 + 4n^2A_o^2(1+m)^2 - 1}{n^2 + 4n^2A_o^2(1+m)^2}}\right\}, \text{...........eq.(A.4)}$$

Now $\frac{1}{A_o} = \left(\frac{m + 1}{m}\right)\frac{d}{v} = \left(\frac{m + 1}{m}\right)\frac{1}{A}$ by definition,

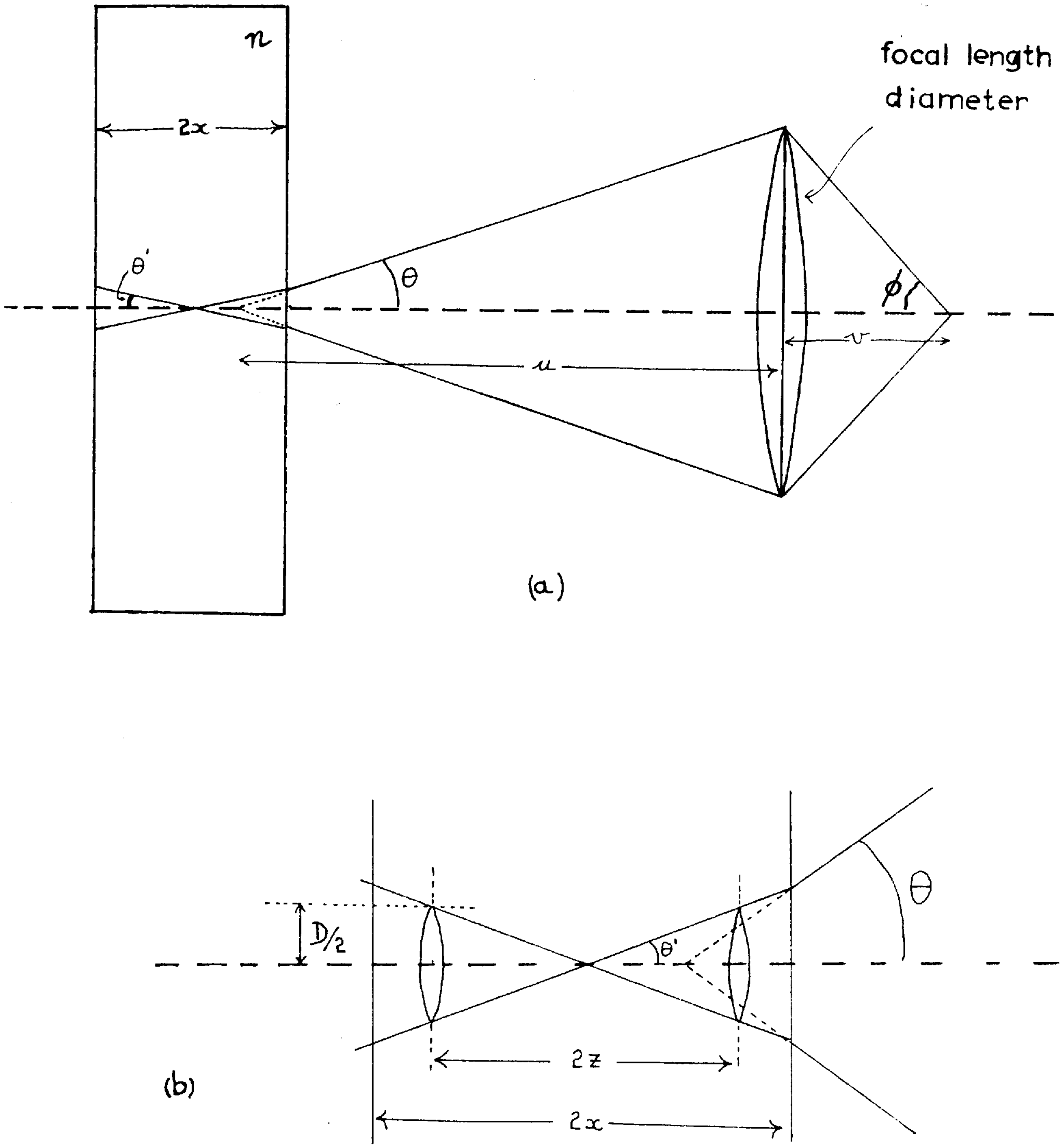

Fig. 31.(a) & (b).

where $A = v/d$

so that $(m+1)A_o = mA$, and substituting in eq.(A.4),

$$F_1 = \tfrac{1}{2}\left\{ 1 - \sqrt{\frac{n^2+4n^2A^2m^2-1}{n^2+4n^2A^2m^2}} \right\} \text{.............eq.(A.5)}$$

This is the exact formula for the fraction collected. For most purposes in scintillation chamber work, approximate forms of eq.(A.5) can be used.

Re-arranging eq.(A.5), we have:-

$$F_1 = \tfrac{1}{2}\left\{ 1 - \left[1 - \frac{1}{n^2+4n^2A^2m^2}\right]^{\frac{1}{2}} \right\}$$

$$= \tfrac{1}{2}\left\{ 1 - (1 - x)^{\frac{1}{2}} \right\} \text{..............eq.(A.6)}$$

$$\text{where } x = \frac{1}{n^2+4n^2A^2m^2} \text{...........eq.(A.7)}$$

Expanding eq.(A.6);

$$F_1 = \tfrac{1}{2}\left\{ 1 - 1 + \tfrac{1}{2}x + \frac{x^2}{8} + \ldots\ldots \right\}$$

$$\approx \frac{x}{4} + \frac{x^2}{16} \text{.............eq.(A.8)}$$

and putting in the value for x from eq.(A.7);

$$F_2 = \frac{1}{4(n^2+4n^2A^2m^2)} + \frac{1}{16(n^2+4n^2A^2m^2)^2} \text{........eq.(A.9)}$$

As a further approximation, we can neglect the second term, giving,

$$F_3 = \frac{1}{4(n^2+4n^2A^2m^2)} \text{.................eq.(A.10)}$$

and finally, if $4A^2m^2 \gg 1$, we have

$$F_4 = \frac{1}{16n^2A^2m^2} \text{...........eq.(A.11)}$$

The following table shows the percentage error of the approximate expressions F_2, F_3, and F_4 compared to the exact formula F_1, when $n = 1.5$, and $A = 1$, and for values of m ranging from ½ to 4.

m	(-) Percentage error of F_2	(-) Percentage error of F_3	(+) Percentage error of F_4
½	0.5%	5.8%	88%
1	0.1%	1.5%	22%
2	0.1%	0.6%	6.1%
3	0.1%	0.3%	3%
4	0.1%	0.1%	1.8%

N.B. $A = 1$ and $n = 1.5$ for the calculations in the table.

Depth of focus

Referring to Fig.31(b), a close up of the chamber cross-section is shown in which a disc of confusion of diameter 'D' corresponds to an usable depth of ± z about the median plane of the chamber.

$$\tan\theta' = \frac{D}{2z} = \frac{d}{\sqrt{n^2d^2+4n^2f^2(1+m^2)^2-d^2}}$$

$$\text{or} \quad \frac{D}{2z} = \frac{1}{\sqrt{(n^2-1)+4n^2A^2m^2}}$$

$$\text{giving } 2z = D\sqrt{(n^2-1)+4n^2A^2m^2} \;\ldots\ldots\ldots\ldots\text{eq.(A.12)}$$

This is the exact formula for z. Taking the approximation that $4n^2A^2m^2 \gg (n^2-1)$, eq.(A.12) becomes;

$$2z = 2nDAm \;\ldots\ldots\ldots\ldots\ldots\text{eq.(A.13)}$$

The table that follows gives the percentage error of the approximate expression, eq.(A.13), for various demagnifications, when A = 1 and n = 1.5.

m	Percentage error of eq.(A.13)
½	28%
1	7%
2	1.75%
3	0.8%
4	0.4%

Summary of Image Tubes Available

Make & Type of tube.	Focus.	Cathode diameter.	Type of cathode.	Phosphor diameter.	Type of phosphor.	Resolution.	Overall voltage	Overall gain.	Typical noise.	Price.
English Electric. (transmission secondary emission 5-stage	electro-static magnetic	2·5cm.	S.20. [~13% Q.E at 4200Å]	2·5cm.	P.11. P.24.	~30 lp/mm	~40Kv	~10^5–10^6.	~100 per cm^2 per sec.	~£1000
20th. Century Electronics. (transmission secondary emission 5 stage)	electro-static magnetic	2cm.	S.9. {~8% Q.E. at 4200Å]	2cm.	P.11. P.24.	~30 lp/mm	~37Kv.	~few times 10^5	100 → 1000 per cm^2 per sec	~£1000
Mullard 2-stage sandwich type.	electro-static	150mm.	S.9.?	2cm	?	20 lp/mm at phosphor			?	?
French Thomson Houston. TH 9450/1/2/3	electro static.	10cm.	S.1. S.4 S.10 S.20	1·4 cm.	P.1. P.20.	4 lp/mm. at centre 2 lp/mm at edge figures refer to cathode	~24Kv.	~50 (also factor ~50 in brightness)	?	?
WX 4171 Westinghouse.	electro static	12·5cm.	S.20 15% Q.E. at 4400Å	2·5cm.	P.15	15 lp/mm at phosphor	25-35Kv	20–40	?	$5000
4-stage transmission secondary emission	electro-static magnetic	2·5cm.	S.11 5-7% Q.E.	2·5cm.	P.11	10-12 lp/mm	25-36Kv	≥5000	?	?
R.C.A. C73491 3-stage sandwich tube.	electro-static	2·5cm.	S.20 ~15% Q.E.	2·5cm.	P.11 P.20	~12 lp/mm	30-45Kv.	5,000 → 50,000	?	$10,000

APPENDIX 'B'

Lens.	Focal length (mm.)	Rated aperture	Resolution [line pairs/m.m.]	Field covered.	Transmission with wavelength	60% vignetting radius (mm.)	Other comments.
Canon.	50	f/1·2	Drops from 90 l.p/mm. to 20 l.p./mm. at 8° semi-angle.		70% at 4300Å	~10mm.	
Dallmeyer.	82·5	f/1·9			75% at 4350Å		See also Table 'D'
Dallmeyer.	152	f/3·5			80% at 4350Å.		See also Table 'D'
Wray.	50	f/1			57% at 4050Å 65% at 4350Å	11 mm.	corrected for operation at 4:1
Angènieux.	50	f/1·5			70% at 4400Å	10mm.	
Oude Delft	50	f/0·75	90 l.p./mm on axis	19mm. image	70% at 4100Å	10mm.	
Oude Delft	65	f/0·75	90 l.p./mm. on axis	22mm image			
Oude Delft	105	f/0·75	65 l.p./mm. on axis	38mm. image			
Oude Delft	150	f/0·75	60 l.p./mm. on axis.	58mm. image	42% at 4150Å		
Dallmeyer	127	f/1·42			70% at 3400Å		condenser doublet.
T. T. H.	50	f/0·8				5·5	
Zeiss.	75	f/1·5				8·5	
NiKKor.	85	f/1·5				10	
Carl Meyer.	60	f/1·6			47% for P11 phosphor 72% for P20 phosphor	7·2	P11 emission peaks at 4500A° P20 emission peaks at 5500Å.
Bausch & Lomb.	127	f/1·9			45% for P11 phosphor 67% for P20 phosphor	25	
Kodak (Aero aktar)	178	f/2·5			28% for P11 phosphor 38% for P20 phosphor	25	

See Ref. 29 also.

APPENDIX E

Expressions for the Velocity and Momentum resolution of the Cerenkov Camera.

(a) Velocity resolution.

For a ring of radius 'r' imaged with a lens of focal length 'f', we have

$$\tan\theta = r/f$$

Substituting for 'θ' in the usual Cerenkov expression, $\cos\theta = 1/\beta n$, we get

$$\frac{f}{\sqrt{f^2+r^2}} = \frac{1}{\beta n} \qquad \text{..............eq.(E.1)}$$

Differentiating eq.(E.1),

$$\frac{frdr}{(f^2+r^2)^{3/2}} = \frac{d\beta}{\beta^2 n} = \frac{d\beta}{\beta}\left(\frac{1}{\beta n}\right) \qquad \text{..........eq.(E.2)}$$

Substituting for $\frac{1}{\beta n}$ from eq.(E.1),

$$\frac{frdr}{(f^2+r^2)^{3/2}} = \frac{d\beta}{\beta}\,\frac{f}{(f^2+r^2)^{1/2}}$$

$$\frac{d\beta}{\beta} = \frac{rdr}{(f^2+r^2)}$$

$$= \frac{dr/r}{(1+f^2/r^2)} = \frac{dr/r}{(1+\cot^2\theta)}$$

$$\frac{d\beta}{\beta} = dr/r\ \mathrm{Sin}^2\,\theta \qquad \text{........eq.(E.3)}$$

$$\approx \theta^2\,d\theta \qquad \text{.............eq.(E.4)}$$

(b) Momentum resolution

$$p = m_o \gamma \beta c$$

$$= m_o(1 - \beta^2)^{-\frac{1}{2}} \beta c \quad \ldots\ldots\ldots\ldots\ldots\ldots\ldots \text{eq.(E.5)}$$

Differentiating eq.(E.5),

$$\frac{dp}{d\beta} = m_o c \left\{ (1-\beta^2)^{-\frac{1}{2}} + (1-\beta^2)^{-3/2} \beta^2 \right\}$$

$$\frac{dp}{p} = m_o c \, d\beta \left\{ \frac{1}{(1-\beta^2)^{\frac{1}{2}}} + \frac{\beta^2}{(1-\beta^2)^{3/2}} \right\} \times \frac{(1-\beta^2)^{\frac{1}{2}}}{m_o \beta c}$$

$$= d\beta \left\{ \frac{1}{\beta} + \frac{\beta}{(1-\beta^2)} \right\}$$

$$\approx \frac{d\beta}{\beta} \left\{ 1 + \frac{1}{(1-\beta^2)} \right\}$$

$$\approx d\beta \, (1 + \gamma^2)$$

and if $\gamma \gg 1$, (i.e. highly relativistic particles),

$$\frac{dp}{p} \approx \gamma^2 \frac{d\beta}{\beta} \quad \ldots\ldots\ldots\ldots\ldots\ldots \text{eq.(E.6)}$$

Combining eqs. (E.4) and (E.6);

$$\frac{dp}{p} \approx \theta^{\cancel{4}} \gamma^2 \, d\theta \quad \ldots\ldots\ldots\ldots\ldots \text{eq.(E.7)}$$

Acknowledgements

The author would like to express his gratitude to Professor P.M.S. Blackett for the opportunity of working in his laboratory.

The author is especially grateful to his supervisor, Mr. J.A. Newth for the constant encouragement and help he has received during the whole duration of the research work, and for maintaining an atmosphere which has made research work a real pleasure.

Thanks are also due to Dr. D.M. Binnie, Mr. A. Duane, Mr. M.R. Jane and Mr. D.C. Potter for many helpful discussions and assistance with the experimental work, especially during the Saclay experimental runs. Valuable technical assistance was given by Mr. R. Hobbs, who was responsible for the construction of most of the experimental apparatus used.

The author wishes to thank M. J. Crussard and the staff and technicians at the French Atomic Energy Centre at Saclay, Paris, for their hospitality and kindness during the time spent there by the author and his colleagues.

Finally, the author wishes to thank D.~~H~~S.I.R. for providing a maintenance grant between 1959 and 1962, and N.I.R.N.S. for providing the research grant which made the research work possible.

References

(1) Glaser, D.A.,
Phys. Rev., 87, 665, (1952).

(2) Baum, W.A ,
Transactions of the International Astronomical Union,
9, 684, (1957).

(3) Bang, B.A.,
Proc. 5th. Int. Cong. High Speed Photography, C.12,
p.141, (1962).

(4) Flanagan, T.P., Anderson, D.G., Noé, E.H., and Dracass, J.,
Adv. in Electronics and Electron Physics, 16, 547, (1962).

(5) Tusting, R.F., Kerns, Q.A., and Knudsen, H.K.,
I.R.E. Trans. on Nuclear Science, N5-9, 118, (1962).

(6) Lombard, F.J., and Martin, F.,
Rev. Sci. Inst., 32, 200, (1961).

(7) Davison, M.,
Private communication.

(8) Todkill, A.,
Private communication.

(9) Wilcock, W.L., Emberson, D.L., and Weekley, B.,
Nature, 185, 370, (1960).

(10) Emberson, D.L.,
Ph.D. Thesis at the University of London, (1961).

(11) Slark, N.A., and Woolgar, A.J.,
Adv. in Electronics and Electron Physics, 15, 141, (1962).

(12) Zavoisky, E.K., Butslov, M.M., Plakhov, A.G., Smolkin, G.E.,
Doklady. Akad. Nauk SSSR, 100, 241, (1955).

(13) Zavoisky et. al.,
Atomic Energy, 1, 34, (1956).

(14) Zavoisky et. al.,
J. Nuclear Energy, 4, 340, (1957).

(15) Demidov, B.A., and Fanchenko, S.D.,
Soviet Physics (J.E.T.P.), 12, 46, (1961).

(16) Reynolds, G.T., and Condon, P.,
Rev. Sci. Inst., 28, 1098, (1957).

(17) Reynolds, G.T.,
Nucleonics, June, 1958, p.60.

(18) Reynolds, G.T.,
Int. Comf. on High Energy Accelerators, CERN, 1959,p576.

(19) Reynolds, G.T., Giacconi, R., and Scarl, D.B.,
Rev. Sci. Inst., 30, 497, (1959).

(20) Reynolds, G.T., Scarl, D.B., Swanson, R.A., Waters, J.R., and Zdanis, R.A.,
Adv. in Electronics and Electron Physics, 15, 487,(1962).

(21) Reynolds, G.T., Scarl, D.B., Swanson, R.A., Waters, J.R., and Zdanis, R.A.,
To be published (in Phys. Rev.).

(22) Jones, L.W., and Perl, M.L.,
Rev. Sci. Inst., 29, 441, (1958).

(23) Perl, M.L., and Jones, L.W.,
Phys. Rev. Letters, 2, 116, (1959).

(24) Jones, L.W., and Perl, M.L.,
Int. Comf. on High Energy Accelerators, CERN, 1959,p561.

(25) Jones, L.W., Lai, K., Newsome, R., and Perl, M.L.,
I.R.E. Transactions on Nuclear Science, N5-7,145,(1960).

(26) Perl, M.L., and Jones, L.W.,
Proc. 5th. Int. Cong. on High Speed Photography,C.2,98, (1962).

(27) Lai, K., Jones, L.W., and Perl, M.L.,
Bulletin of Am. Phys. Soc., Series II, 5, 427, (1960).

(28) Lai, K., Jones, L.W., and Perl, M.L.,
Phys. Rev. Letters, 7, 125, (1961).

(29) Jones, L.W., and Perl, M.L.,
Adv. in Electronics and Electron Physics, 15, 513,(1962)

(30) Hill, D.A., Caldwell, D.O., and Schluter, R.A.,
Adv. in Electronics and Electron Physics, 15, 475,(1962)

(31) Lande, K., Mann, A.K., Schachter, M.M., Skyrme, D.M., and Uto, H.,
Rev. Sci. Inst., 30, 496, (1959).

(32) Goetze, G., and Kanter, H.,
Nuc. Inst. and Methods, 10, 224, (1961).

(33) Anderson, A.E., Goetze, G., and Kanter, H.,
Proc. 5th. Int. Cong. on High Speed Photography, C.1. 95, (1962).

(34) Geise, R., Gildemeister, O., and Paul, W.,
Int. Conf. on High Energy Accelerators, CERN,1959,p571

(35) Gildermeister, O., and Geise, R.,
Adv. in Electronics and Electron Physics., 15,113,(1962)

(36) Duflo, J.,
J. Phys. Radium, 21, 65A, (1960).

(37) Salvadori, P.,
Rendiconti Instituto Superiore Di Sanita, 25, 62, (1962)

(38) McGee, J.D.,
'Nuclear Instruments' Symp. at Harwell, 1961,paper N1/1

(39) McGee, J.D.,
Private communication.

(40) Rankin, B.,
Rev. Sci. Inst., 25, 675, (1954).

(41) Van-Rossum, L.,
Private communication.

(42) Davison, M.,
Private communication.

(43) Reiffel, L., and Kapany, N.S.,
Rev. Sci. Inst., 31, 1136, (1960).

(44) Galbraith, W., Manning, G., and Parham, A.G.,
"A Gas Cerenkov Counter for use at Nimrod", AERE-R3968 (1962).

(45) Roberts, A.,
Nuc. Inst and Methods, 9, 55, (1960).

(46) Parham, A.G.,
AERE-R4110, p3, (1962).

(47) Dedrick, K.G.,
Phys. Rev., 87, 891, (1952).

(48) Nicoll, N.E., (Nuclear Enterprises Ltd)
Private communication.

(49) Gardner, J.W., King, N.M., Whiteside, D.,
Rutherford High Energy Laboratory, NIRL/R/12, (1962)

(50) Whiteside, D., (Rutherford High Energy Laboratory)
Private communication.

(51) Gardner, J.W., and Whiteside, D.,
Rutherford High Energy Laboratory, NIRL/M/21, (1961).

(52) Sard, R.D.,
Berkeley Instrumentation Conference, p320,(1960).

(53) Heer, E.,
Berkeley Instrumentation Conference, p284, (1960).

(54) Gulligan, G., Harting, D., Lipman, N.H.,
CERN publication 61-25, (1961).

(55) Fischer, J., and Zorn, G.T.,
Berkeley Instrumentation Conference, p281, (1960).

(56) Jones, L.W., and Perl, M.L.,
Nuc. Inst. and Methods, 10, 348, (1961).

(57) Waters, J.R., Reynolds, G.T., Scarl, D.B., and Zdanis, R.A.,
Nuc. Inst. and Methods, 17, 44, (1962).

(58) Miller, D.H., (CERN, Geneva),
Private communication.

(59) Fischer, J., and Zorn, G.T.,
I.R.E. Transactions on Nuclear Science, N5-9,261,(1962)

(60) Danby, G., Gaillard, J.M., Goulianos, K., Lederman, L.M.,
Mistry, N., Schwartz, M., and Steinberger, J.,
Phys. Rev. Letters, 9, 36, (1962).

(61) Crittenden, R.R., and Walker, W.D.,
Phys. Rev., 121, 1823, (1961).

(62) Parker, S., and Penman, S.,
Nuovo Cimento, 23, 485, (1962).

(63) Alikhanov, A.I., Babaev, A.I., Balats, M. Ja., Kaftanov, V.S., Landsberg, L.G., Ljubimov, V.A., and Obukhov, Iu. V.,
Publication of the Inst. of Theoretical and Experimental Physics, Moscow, (1962).

(64) Bartlett, D., Devons, S., and Sachs, A.M.,
Phys. Rev. Letters, 8, 120, (1962).

(65) Frankel, S., Halpern, J., Holloway, L., Wales, W., and Yearian, M.,
Phys. Rev. Letters, 8, 123, (1962).

(66) Doolittle II, R.F., and Graves, C.D.,
Adv. in Electronics and Electron Physics, 16, 535, (1962)

(67) Sandweiss, J.,
'Experimental Program Requirements for a 300-1000 GeV Accelerator', Brookhaven, Upton, N.Y., section II C2(a) (1961).

(68) Robertson, D.S.,
'Experimental Program Requirements for a 300 - 1000 GeV Accelerator', Brookhaven, Upton, N.Y., II C2(b) (1961).

(69) Hill, D.A., and Porter, N.A.,
Adv. in Electronics and Electron Physics, 16, 531,(1962).

APPENDIX 'D'

Range against Energy & Momentum for NaI(Tl).

Walton

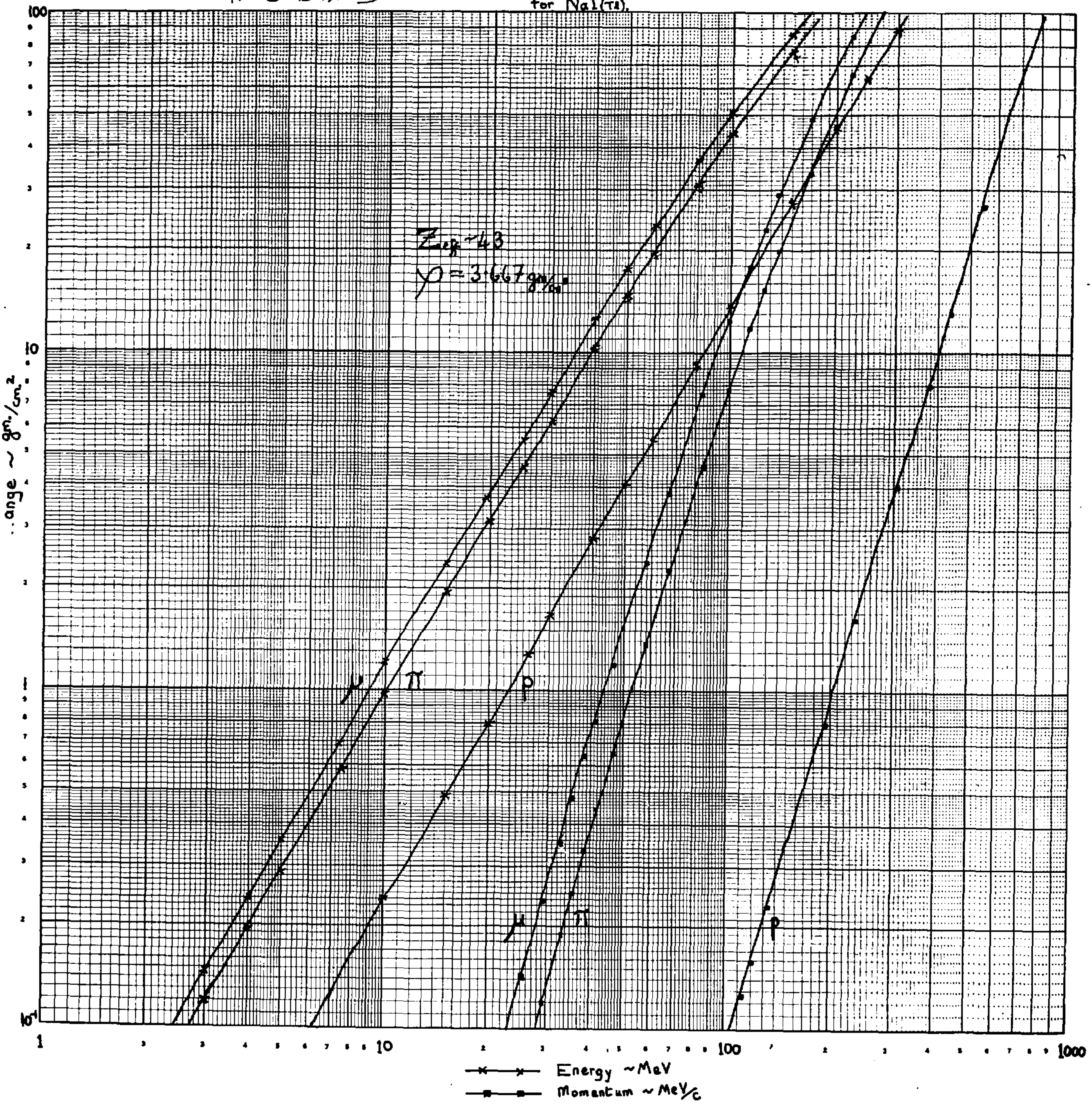

Range against Energy and Momentum.
for CsI (Tl) crystal.

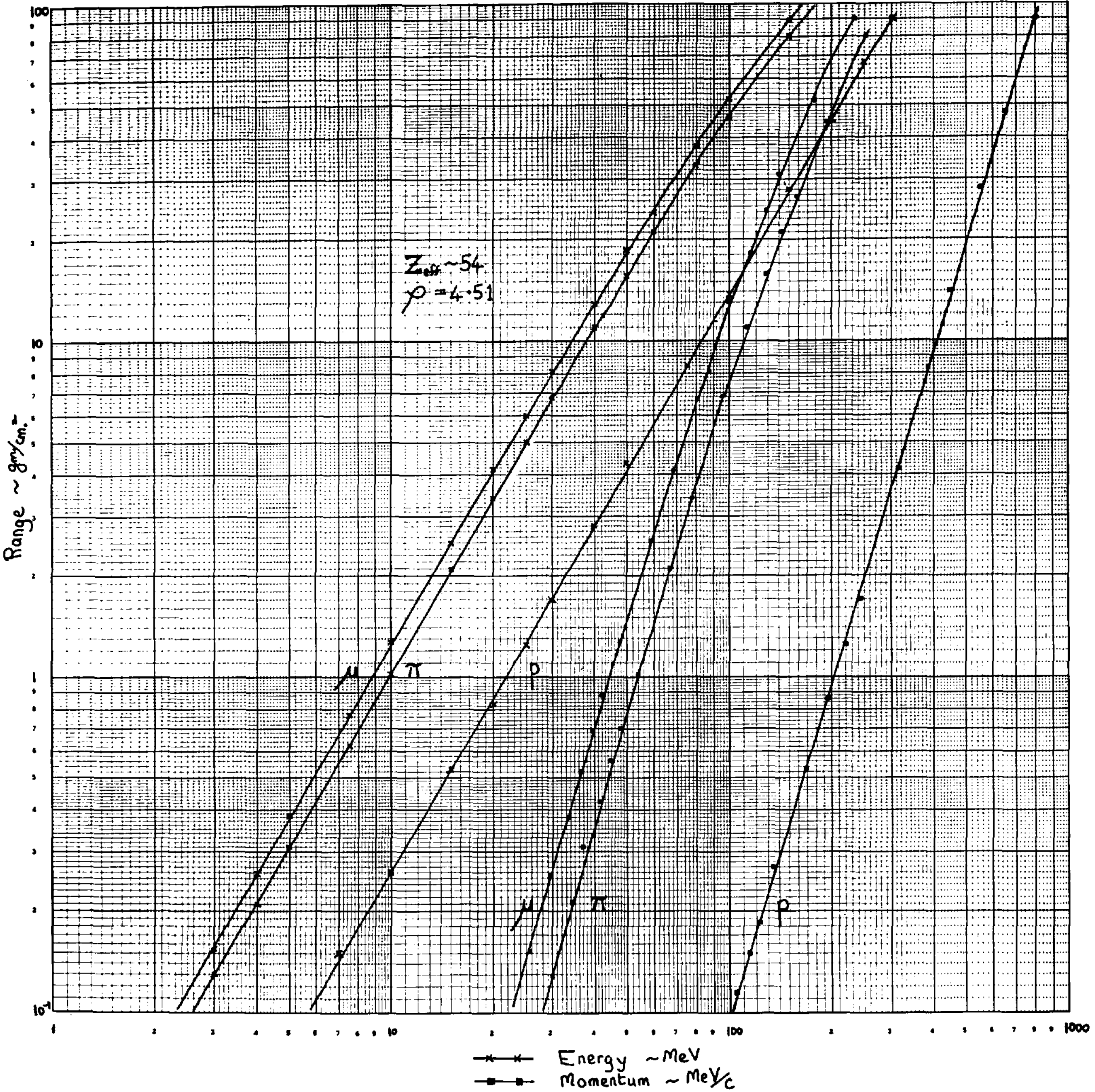

$\frac{dE}{dx}$ against Momentum for CsI(Tl) & NaI(Tl)

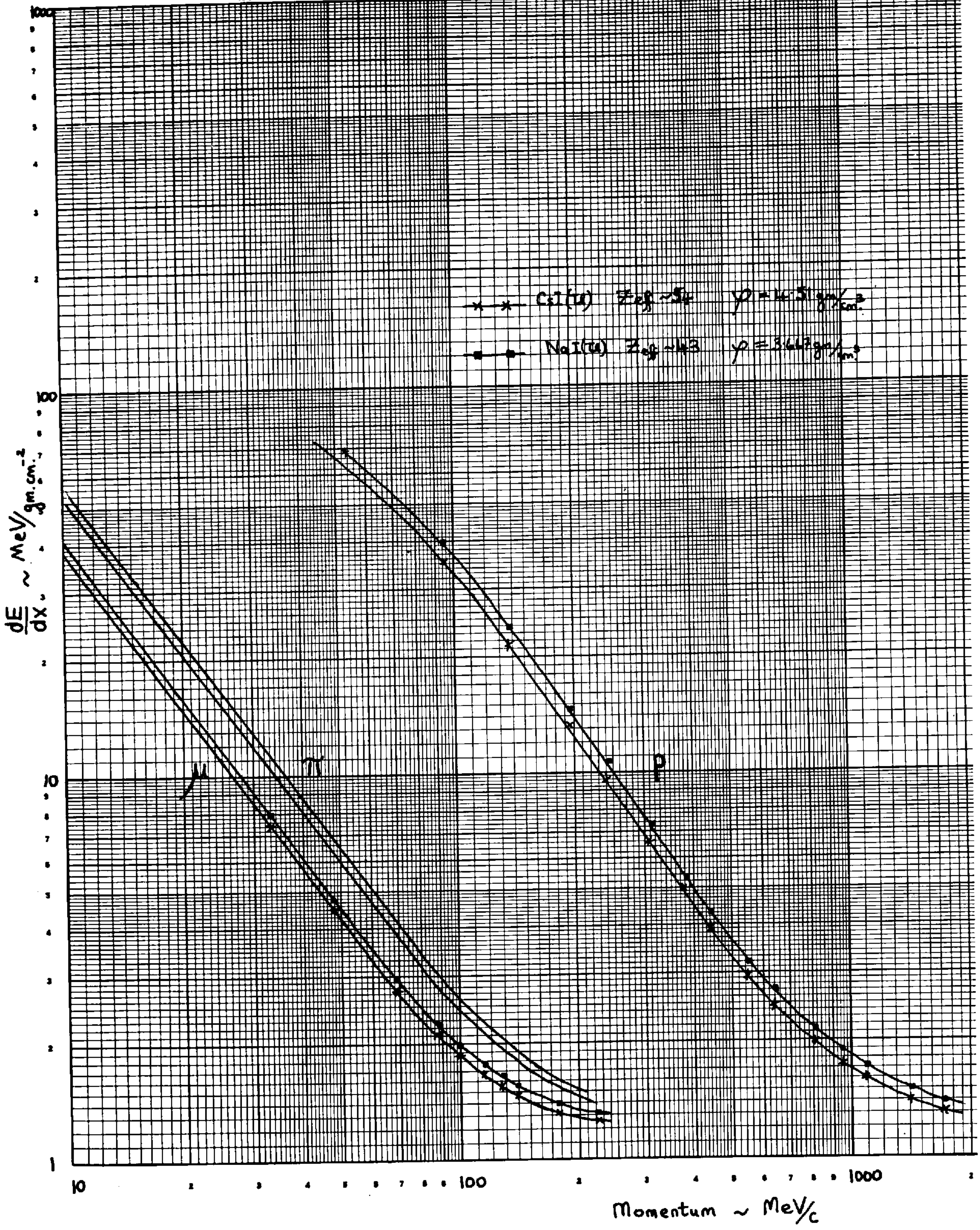

Range versus Energy and Momentum
for NE102 plastic scintillator.

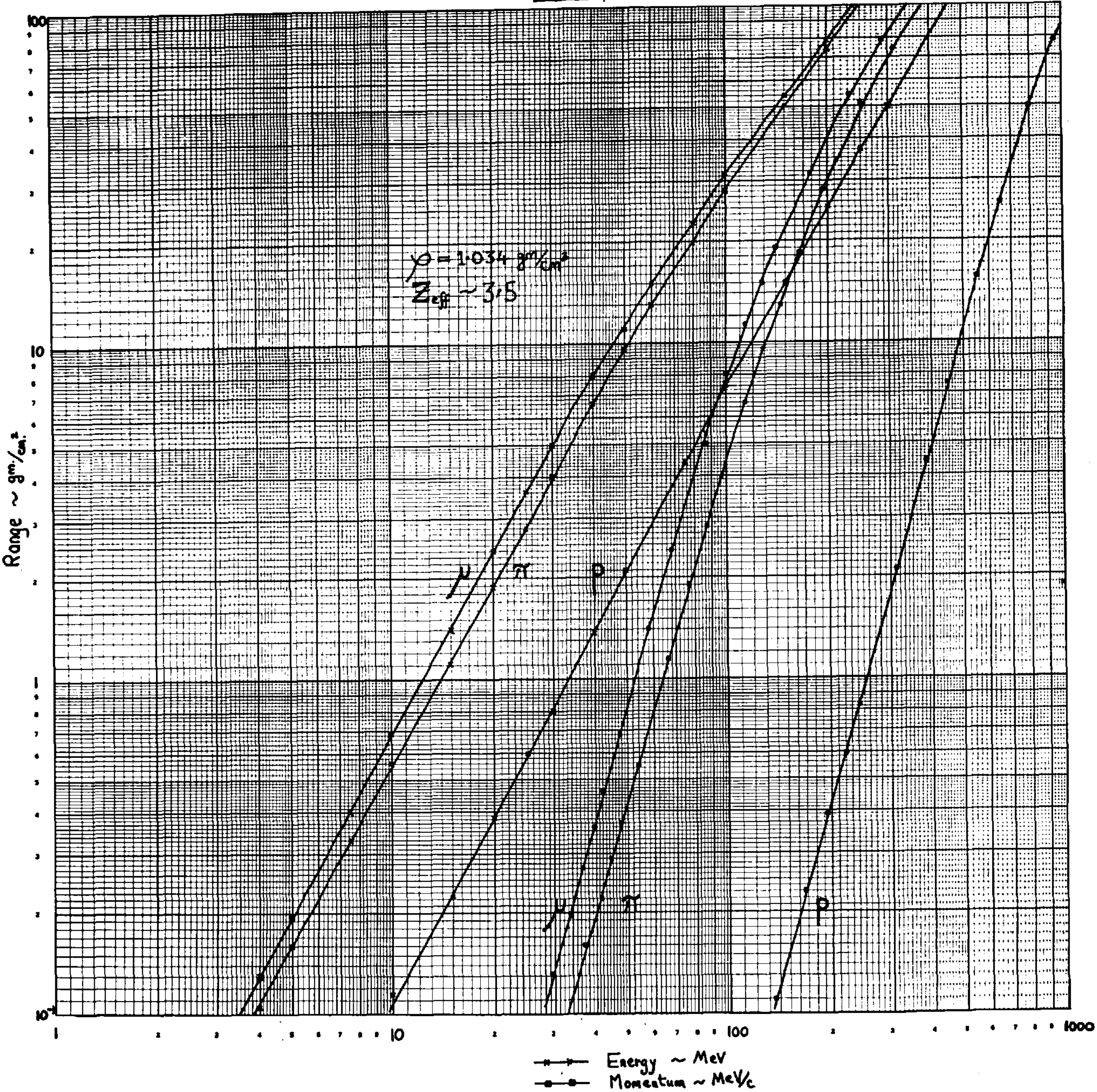

$\frac{dE}{dx}$ against momentum for NE102 plastic scintillator

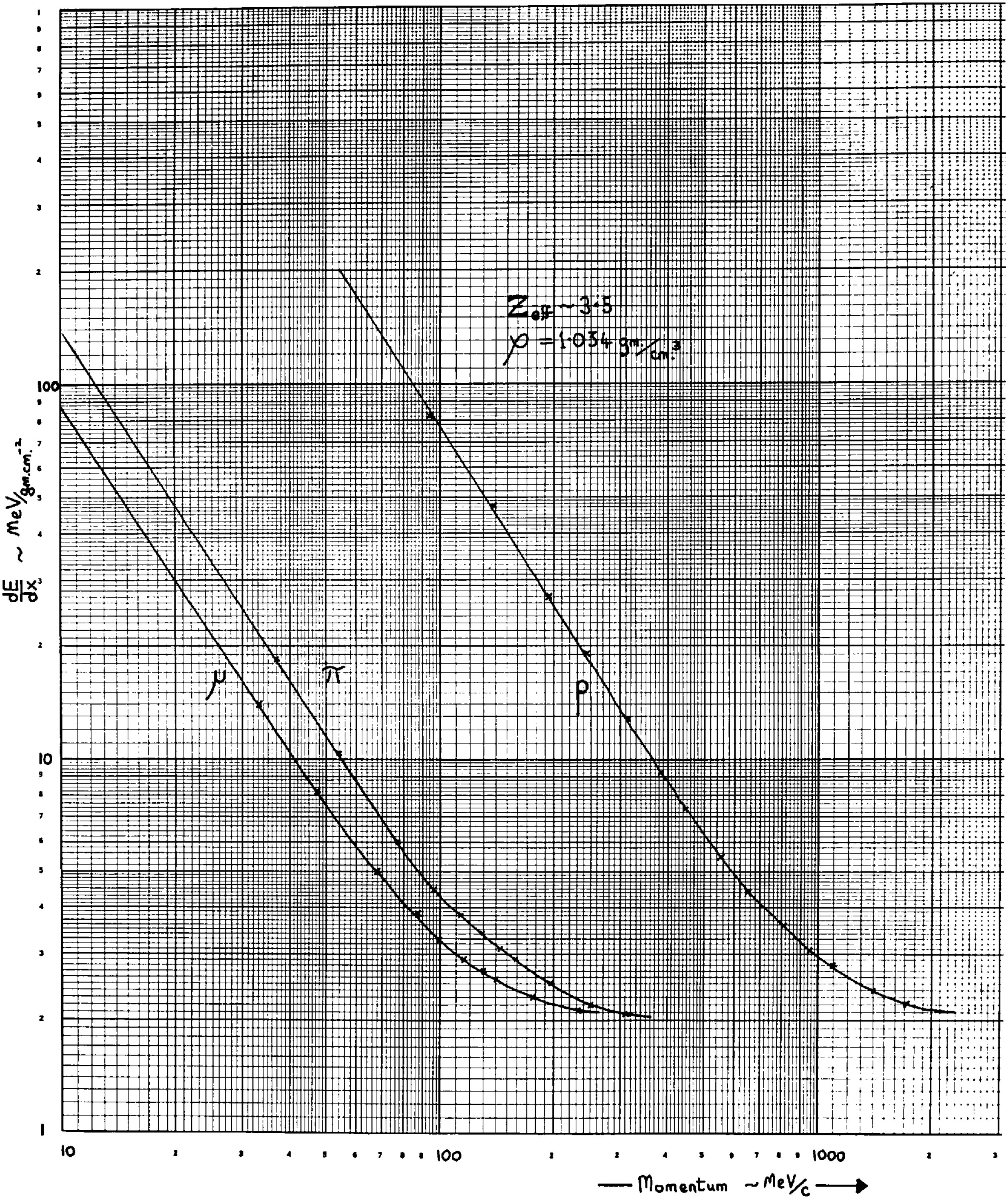

Range against Energy and Momentum
for GS/1 glass

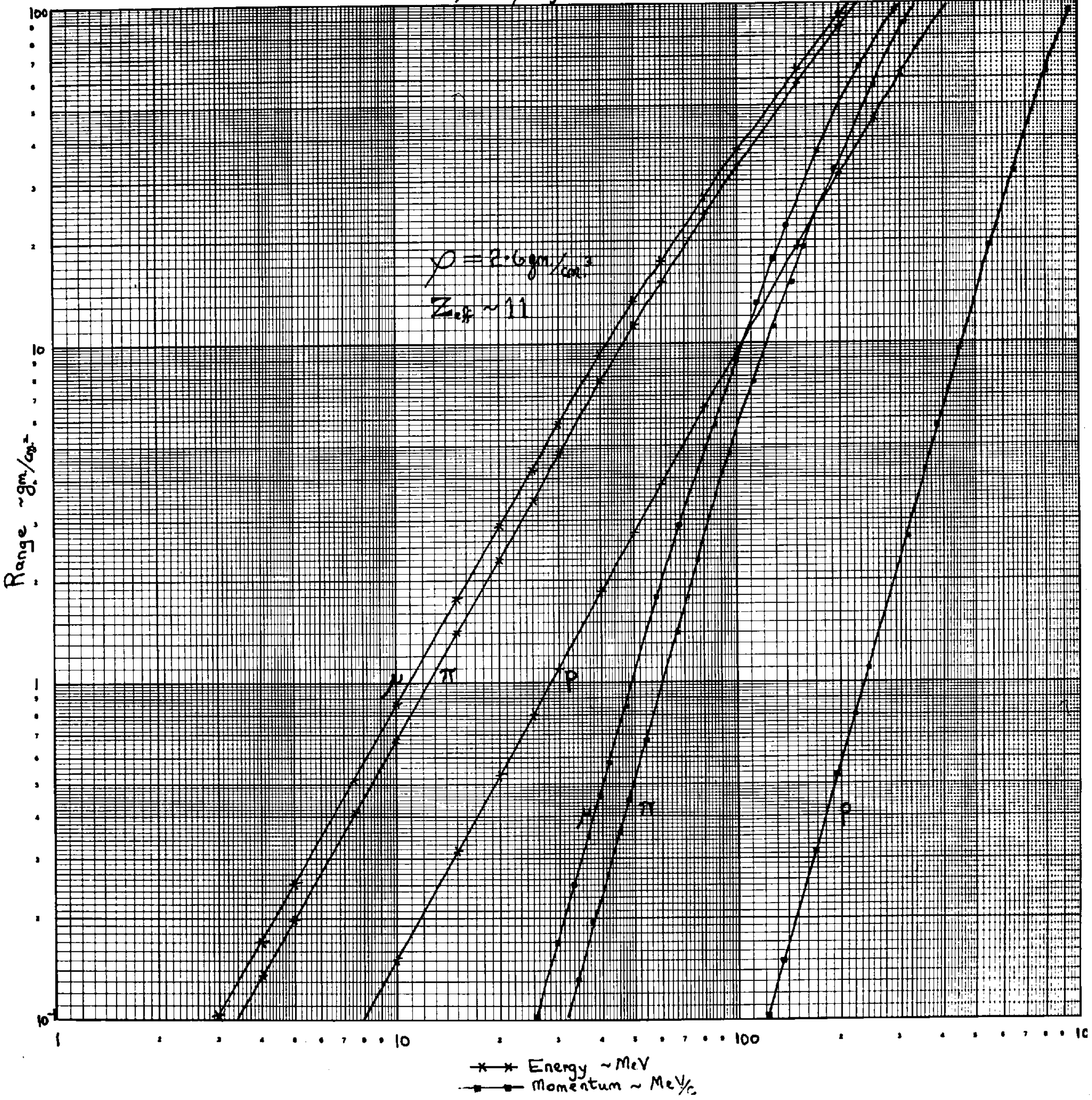

$\frac{dE}{dx}$ against Momentum for GS/1 glass.